

NUMERICAL MODELING OF MULTIPHASE PLUMES: A COMPARATIVE
STUDY BETWEEN TWO-FLUID AND MIXED-FLUID INTEGRAL MODELS

A Thesis

by

TIRTHARAJ BHAUMIK

Submitted to the Office of Graduate Studies of
Texas A&M University
in partial fulfillment of the requirements for the degree of

MASTER OF SCIENCE

August 2005

Major Subject: Ocean Engineering

NUMERICAL MODELING OF MULTIPHASE PLUMES: A COMPARATIVE
STUDY BETWEEN TWO-FLUID AND MIXED-FLUID INTEGRAL MODELS

A Thesis

by

TIRTHARAJ BHAUMIK

Submitted to the Office of Graduate Studies of
Texas A&M University
in partial fulfillment of the requirements for the degree of

MASTER OF SCIENCE

Approved by:

Chair of Committee,
Committee Members,

Head of Department,

Scott A. Socolofsky
Kuang-An Chang
Yassin A. Hassan
David Rosowsky

August 2005

Major Subject: Ocean Engineering

ABSTRACT

Numerical Modeling of Multiphase Plumes: A Comparative Study Between
Two-fluid and Mixed-fluid Integral Models. (August 2005)

Tirtharaj Bhaumik, B.Tech., IIT Kharagpur, India

Chair of Advisory Committee: Dr. Scott A. Socolofsky

Understanding the physics of multiphase plumes and their simulation through numerical modeling has been an important area of research in recent times in the area of environmental fluid mechanics. The two renowned numerical modeling types that are commonly used by researchers today to simulate multiphase plumes in nature are the mixed-fluid and the two-fluid integral models. In the present study, a detailed review was performed to study and analyze the two modeling approaches for the case of a double plume (upward moving inner plume with downward moving annular outer plume) with the objective of ascertaining which of these models represent the prototype physics in the integral plume model equations with a higher degree of completeness and accuracy. A graphical user interface was designed to facilitate running the models. By comparison to laboratory scale experimental data and through sensitivity analyses, a rigorous effort was made to determine the most appropriate choice of initial conditions needed at the start of the model computation and at the peeling locations and to obtain the most consistent values of the different model parameters that are necessary for calibration of the two models. Consequently, with these selected sets of initial conditions and model parameters, the models were run and their outputs compared against each other for three different case studies with ambient conditions typical of real environmental data. The dispersed phases considered were air bubbles in two cases and liquid CO₂ droplets for the third case, with water as the continuous phase in all cases. The entrainment coefficient was found to be the most

important parameter that affected the model results. In all the three case studies conducted, the mixed-fluid model was found to predict about 30% higher values for the peel heights and the DMPR (Depth of Maximum Plume Rise) than the two-fluid model.

To my parents and grandparents

ACKNOWLEDGMENTS

This work was funded by the United States National Science Foundation and was part of the project: “CAREER: The role of turbulence, coherent structures, and intermittency for controlling transport in multiphase plumes in the environment.” (Grant CTS-0348572). In addition to financial support, I gratefully acknowledge the invaluable guidance and motivation extended to me by my advisor, Dr. Scott A. Socolofsky concerning this work. I deeply appreciate the amount of time he willingly sacrificed for me in arduously offering his help, which ranged from explaining to me several doubts which I had regarding mathematical derivations, programming issues, experimental data interpretation and analyses to editing the thesis manuscript.

I also appreciate the kind words of inspiration which I often received from my committee members, Dr. Kuang-An Chang and Dr. Yassin A. Hassan during the course of this work. I would like to thank my research-mate, Dong-Guan Seol for providing me with the experimental data and to the exchange student, Christian Bergmann for participating with me in several useful discussions concerning the experimental data analysis and the numerical model implementation at the initial stages of this work.

Outside the research arena, I am indebted to all my friends for their kind words of inspiration, consolation and good humor, for offering their help and advice whenever I needed, and for giving me good company and enlivening my spirit from time to time.

I thank God for showering His blessings upon me and for keeping me in good health and spirits. Last but not the least, I thank my beloved parents, grandparents and relatives for giving me love, care and all kinds of support as always, and for their words of encouragement from afar.

TABLE OF CONTENTS

CHAPTER		Page
I	INTRODUCTION	1
	1. Multiphase Flow Basics	2
	1.1. Multiphase Plume Types	6
	2. Numerical Modeling of Multiphase Plumes	8
	2.1. The Mixed-fluid Model	9
	2.2. The Two-fluid Model	14
	3. Case Studies	15
	3.1. Case 1: Lake Destratification	15
	3.2. Case 2: Lake Aeration	16
	3.3. Case 3: CO ₂ Sequestration in the Ocean	17
	4. Thesis Organization	19
II	GOVERNING EQUATIONS	21
	1. The Self-Similarity Assumption	23
	1.1. Gaussian and Top-Hat Distribution	24
	1.2. Relationship between Gaussian and Top-Hat Variables	25
	2. Conservation Equations	26
	2.1. Single Plume Model Equations	26
	2.1.1. Conservation of Volume Flux	26
	2.1.2. Conservation of Momentum Flux	28
	2.1.3. Conservation of Buoyancy Flux	32
	2.1.4. Conservation of Temperature Flux	34
	2.1.5. Conservation of Concentration Flux	34
	2.1.6. Conservation of Salinity Flux	35
	2.1.7. Conservation of Mass Flux of Dispersed Phase	35
	2.2. Closure Equations	36
	2.2.1. Buoyancy Flux of Dispersed Phase	36
	2.2.2. Slip Velocity of Dispersed Phase	37
	2.3. Double Plume Model Equations	38
	2.3.1. Inner Plume Equations	39
	2.3.2. Outer Plume Equations	42
	3. Summary of Equations	44
	3.1. State Variables	44
	3.2. Primary Variables	46
	3.3. Two-fluid Model Equations	47

CHAPTER	Page
3.4. Mixed-fluid Model Equations	49
III MODEL PARAMETERS	51
1. Phase Properties	51
1.1. Density	51
1.2. Viscosity	54
1.3. Surface Tension	54
1.4. Mass Transfer Coefficient	55
1.5. Solubility	55
1.6. Solute Density Effect	57
1.7. Heat of Dissolution	58
1.8. Specific Heat	58
1.9. Compressibility	59
2. Ambient Properties	59
2.1. Temperature	59
2.2. Salinity	60
2.3. Dissolved Insitu Concentration	60
2.4. Entrainment Coefficient	61
2.5. Momentum Amplification Factor	62
3. Design Variables	62
3.1. Flow Rate	62
3.2. Diffuser Dimensions	63
3.3. Number Flux of Dispersed Phase	64
3.4. Spreading Ratio	64
IV MODEL ALGORITHM AND GRAPHICAL USER INTERFACE	66
1. Model Algorithm	66
2. Program Inputs	69
2.1. Constant Input Data	69
2.2. Data Varying with Depth	72
3. Graphical User Interface	74
V INITIAL CONDITIONS	79
1. Inner Plume Initial Conditions at the Diffuser Source	80
1.1. Concept of Power Series	80
1.2. Concept of Virtual Point Source	81
1.3. Concept of Densimetric Froude Number	82
2. Outer Plume Initial Conditions	85

CHAPTER	Page
3. Initial Conditions for Subsequent Inner Plumes	87
3.1. Concept of Bubble Core Radius	87
VI MODEL CALIBRATION	92
1. Experiment in Unstratified Ambient	92
2. Determination of the Right Choice of Initial Conditions to Match Model Results with Experimental Data	98
3. Verification of Model Results against Experiments in Strat- ified Ambient	108
4. Sensitivity Analysis	114
VII MODEL APPLICATIONS	116
1. Lake Destratification	117
2. Lake Aeration	122
3. Ocean Sequestration of CO ₂	126
VIII SUMMARY AND CONCLUSIONS	133
REFERENCES	136
APPENDIX	143
VITA	148

LIST OF TABLES

TABLE		Page
1	Best-fit model parameters	114
2	Base case parameters	117
3	Lake temperature data taken from Nepf(1995)	118
4	Ocean temperature data taken from Teng(1996)	129
5	Coefficients b_{ij} for the CO ₂ equation of state	146
6	Coefficients and exponents for the air equation of state	147

LIST OF FIGURES

FIGURE	Page
1	Schematic of an air-bubble plume in water 4
2	Types of multiphase plumes 7
3	Double plume model of McDougall(1978) 10
4	Double plume model of Asaeda & Imberger(1993) 12
5	Double plume model of Socolofsky, Crounse & Adams(2002) 13
6	Destratification of a lake by air-bubble plume 15
7	Aeration of a lake by air-bubble plume 16
8	CO ₂ sequestration in ocean 18
9	Top-hat and Gaussian distribution for the state variables 24
10	The entrainment hypothesis 26
11	Conservation of momentum inside control volume 28
12	Conservation of buoyancy inside control volume 32
13	Flowchart of model algorithm 68
14	Graphical user interface designed for the multiphase plume integral models 75
15	Illustration of the virtual point source concept 83
16	Experimental set-up to simulate air-bubble plumes in an unstratified ambient 93
17	Calculated values of α , γ and u_s 96
18	Extrapolated values of α, γ and u_s 96

FIGURE	Page
19	Dimensional plots of Q , J , u and b vs. z with experimental initial conditions 98
20	Non-dimensional plots of Q , J , u and b vs. z with experimental initial conditions 99
21	Plot of C and F_r vs. z with experimental initial conditions 99
22	Dimensional plots of Q , J , u and b vs. z using McDougall's initial conditions 101
23	Non-Dimensional plots of Q , J , u and b vs. z using McDougall's initial conditions 101
24	Plot of C and F_r vs. z for McDougall's initial conditions 102
25	Dimensional plots of Q , J , u and b vs. z using Cederwall & Ditmars' initial conditions 102
26	Non-Dimensional plots of Q , J , u and b vs. z using Cederwall & Ditmars' initial conditions 103
27	Plot of C and F_r vs. z for Cederwall & Ditmars' initial conditions . . 103
28	Dimensional plots of Q , J , u and b vs. z using Wuest's initial conditions with initial $F_r = 0.8$ 104
29	Non-Dimensional plots of Q , J , u and b vs. z using Wuest's initial conditions with initial $F_r = 0.8$ 104
30	Plot of C and F_r vs. z for Wuest's initial conditions with initial $F_r = 0.8$ 105
31	Dimensional plots of Q , J , u and b vs. z using Wuest's initial conditions with initial $F_r = 1.6$ 105
32	Non-Dimensional plots of Q , J , u and b vs. z using Wuest's initial conditions with initial $F_r = 1.6$ 106
33	Plot of C and F_r vs. z for Wuest's initial conditions with initial $F_r = 1.6$ 106

FIGURE	Page
34	Correlation of plume peel height to U_N . All data are from Socolofsky and Adams (2005). Typical error bars are shown for one data point. 108
35	Correlation of plume trap height to U_N . Right-pointing triangles are data from Lemckert and Imberger (1993), circles are from Asaeda and Imberger (1993) and squares are from Socolofsky and Adams (2005). Open symbols are air bubble experiments; closed symbols are glass bead experiments. Typical error bars are shown for one data point. 109
36	Two-fluid model results for different initial conditions 110
37	Mixed-fluid model results for different initial conditions 110
38	Comparison of the two-fluid and the mixed-fluid model 111
39	Sensitivity of model to α 112
40	Sensitivity of model to γ 113
41	Sensitivity of model to λ_1 113
42	Sensitivity of model to κ 115
43	Density stratification for the lake 119
44	Numerical simulation of air-bubble for the lake using the two-fluid modeling approach. $Q_0 = 15.0$ l/s in this figure which gives the first peel at the water surface. Bold lines denote the inner plume and dashed lines denote the outer plume. 119
45	Numerical simulation of air-bubble for the lake using the mixed-fluid modeling approach. $Q_0 = 5.0$ l/s in this figure which gives the first peel at the water surface. Bold lines denote the inner plume and dashed lines denote the outer plume. 120
46	Top view of the 7 m diameter diffuser <i>TANYTARSUS</i> (McGinnis, Lorke, Wüest, Stöckli & Little 2004) 123

FIGURE	Page
47	Numerical simulation of air-bubble for the lake using the mixed-fluid and two-fluid modeling approaches. Bold lines denote results for the two-fluid model and dotted lines for the mixed fluid model. 124
48	Phase properties vs. depth as tracked by the two-fluid and the mixed-fluid models. Bold lines denote results for the two-fluid model and dotted lines for the mixed fluid model. 125
49	DMPR of air-bubble plumes for different values of diffuser air flowrate and bubble diameter. 125
50	Schematic of various CO ₂ sequestration schemes in the deep ocean (http://archive.greenpeace.org/politics/co2/co2dump.pdf) 128
51	Variation of ocean water density with depth 130
52	Comparison of results for the two-fluid and mixed-fluid models. Bold lines denote results for the two-fluid model and dotted lines for the mixed fluid model. 131
53	Comparison of results for the two-fluid and mixed-fluid models for estimated DMPR for liquid CO ₂ droplet plumes 132

CHAPTER I

INTRODUCTION

Multiphase plumes are encountered in a variety of engineering problems. To name a few, liquid plumes driven by air-bubbles are used to prevent surface ice formation in harbors by bringing warmer water to the surface (McDougall 1978). Turbulence generated by air bubbles can be effectively utilized to destratify reservoirs by mixing denser water at the bottom with its lighter counterpart in the upper layers (Baines & Leitch 1992). Air-bubble plumes are also widely used to reaerate lakes (Wüest, Brooks & Imboden 1992, Schladow 1993) in order to provide oxygen to bottom water in summer. The same principle has also been successfully employed in designing bubble curtains for the purpose of containing spills due to accidental blowouts of oil and gas (Yapa & Zheng 1999) and for discouraging sharks. Use of bubble barriers for shockwave protection from underwater explosions is another area where the knowledge of multiphase plume dynamics prove worthwhile. Other than air-bubble plumes, the study of the near-field effects of a multiphase plume of liquid CO₂ droplets in ocean water finds potential in estimating the environmental risks involved due to deep-ocean sequestration of greenhouse gases like carbon dioxide, which is one of the proposed alternatives (Liro, Adams & Herzog 1992) to mitigate the problem of global warming on earth. Contaminant containment (Milgram 1983) and continuous particle clouds resulting from the release of dredged sediments (Koh & Chang 1973) and a host of multiphase bubble, droplet and powder flows in industry (Taitel, Barnea & Brill 1995, Johnson & White 1993) are other areas of multiphase plume applications.

In the past, several attempts have been made to devise robust numerical mod-

The journal model is *Journal of Hydraulic Engineering*.

els to simulate multiphase flow phenomena. Simultaneously, efforts have been made to validate the models by experimental measurements. The two popular numerical modeling approaches in the study of multiphase plumes are the mixed-fluid (McDougall 1978, Asaeda & Imberger 1993) and the two-fluid (Socolofsky, Crouse & Adams 2002) integral plume models. The difference between the two models is illustrated later in this chapter. The objective of this present work is to ascertain which of these models represent the prototype physics with a higher degree of completeness and accuracy. This is achieved by calibration of the model to laboratory scale experiments (Bergmann, Seol, Bhaumik & Socolofsky 2004, Socolofsky & Adams 2005) and then by comparison of the model results to three field scale case studies, namely the destratification of a reservoir by air-bubble plumes, the aeration of a lake by air bubble plumes, and the sequestration of CO_2 in the deep ocean by the release of liquid CO_2 droplets. With this motivation, the present work is aimed at performing a detailed numerical analysis for each of the three case studies and comparing the outputs from the two different numerical modeling approaches.

1. Multiphase Flow Basics

Multiphase flows, in most general terms, are flows involving the dynamics of two or more immiscible phases. Numerous examples of such flows exist in a variety of scientific and engineering disciplines. All of these flows typically involve the motion of a dispersed phase consisting of bubbles, droplets or particles through a surrounding medium called the continuous phase. Understanding and formulating the dynamics of multiphase flows is important because of the direct implications it has in developing conceptual models of new design techniques and in optimising the design methodology of systems that operate such flows.

Multiphase flows can be broadly classified under two flow regimes. This classification is based on the physical quantity responsible for driving the dispersed phase through the continuous phase. When the driving force is the momentum flux of the dispersed phase the flow is called a *jet*. The momentum flux of a jet is generated by imparting a high initial momentum to the released dispersed phase. On the other hand, when the driving force is the buoyancy flux of the dispersed phase which is generated due to the density difference of the phases with respect to the ambient stratification, the flow is described as a *plume*. Typically plumes have a zero initial velocity and eventually, all buoyant jets act like plumes.

Plumes in stratification have an upward moving core flow forming the inner plume, and an annular, downward moving outer flow forming the outer plume. Models that capture the inner and outer plume motions are called double-plume models. The schematic of a double plume in a stratified ambient is depicted in Figure 1 with air-bubbles constituting the released dispersed phase. The air-bubbles are injected by a diffuser source at a depth H below the free surface which forms the dispersed phase. The released bubbles drag the surrounding water with their inherent buoyancy flux thereby forming a conical plume of surrounding water which forms the continuous phase. This phenomenon is called *entrainment* in turbulent shear flow nomenclature. In the absence of stratification or crossflow, the bubbles will entrain fluid from the ambient while rising vertically upwards without causing any peeling or separation between the phases. However in the real environment, usually some level of stratification will be present in the ambient fluid so that a fraction of the entrained fluid will become negatively buoyant at a height h_P where peeling or separation will occur between the phases, and henceforth part of the peeled fluid will be re-entrained by the plume on its way downwards and the remaining part will spread laterally after being trapped at a level of neutral buoyancy at a height h_T . The dispersed phase

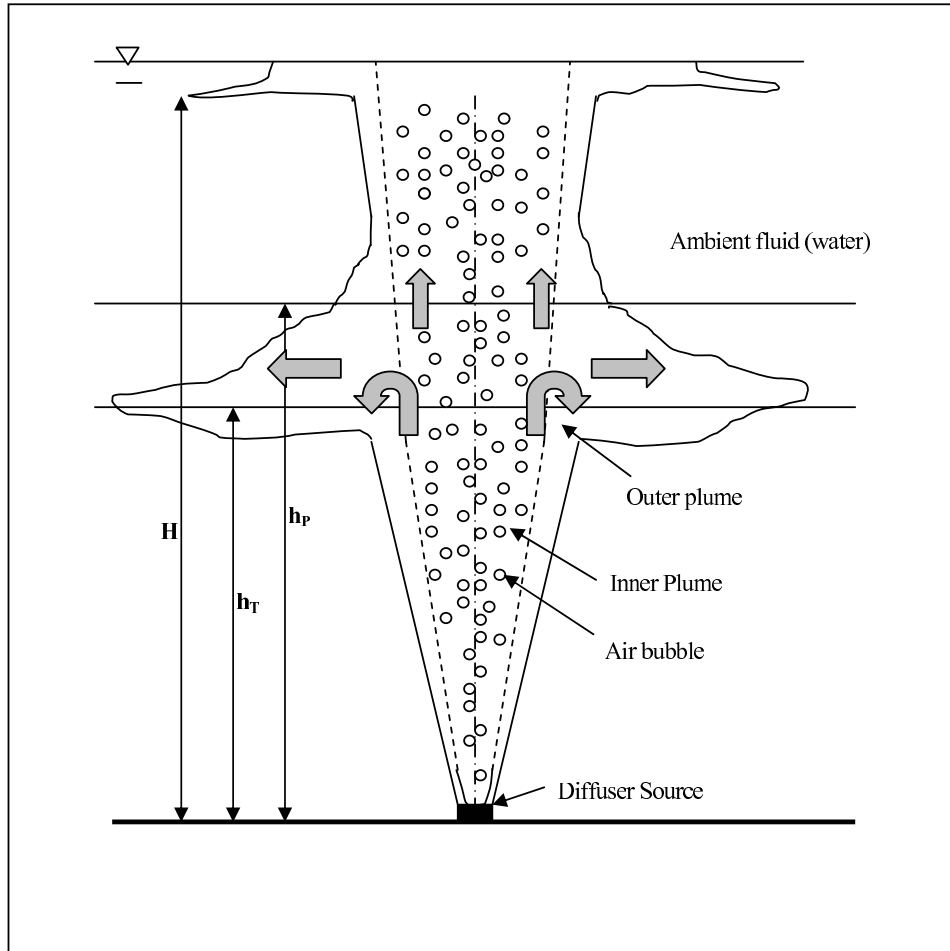


Fig. 1. Schematic of an air-bubble plume in water

will continue to rise above the height h_P . This phenomenon of separation between phases is absent in the case of single phase plumes, examples of which are sewage plumes in sea water or heated water plumes resulting from the use of once-through cooling in electrical power production. It is this phenomenon of separation which makes the dynamics of multiphase plumes more difficult to formulate as compared to single phase plumes.

The separation between phases are best viewed by the two important length scales mentioned before - the peel or separation height h_P and the trap or intrusion height h_T . These length scales are governed by the buoyancy flux of the dispersed phase and the entrained and detrained volume fluxes into and out of the plume respectively. The entrainment and detrainment depend on the values of the turbulent entrainment coefficients, which in turn vary according to the dispersed phase properties and the plume type. The more the entrainment, the more is the added negative buoyancy to the plume and this causes the plume to decelerate and peel faster. The higher the buoyancy flux of the dispersed phase, the greater is the drag force exerted by the dispersed phase and consequently greater is the distance through which the continuous phase is carried upward before it starts to peel. In case of an unstratified ambient, the buoyancy of the continuous phase is everywhere equal to zero because the entrained fluid will always have the same density as the ambient irrespective of the location where it is entrained from. With stratification present, the fluid entrained at a higher level of stratification when carried upward has a higher density compared to the ambient because of the ambient density gradient which gives rise to a negative buoyancy flux to the entrained continuous phase at this level. The higher the ambient stratification gradient, the quicker will the negative buoyancy of the continuous phase supercede the drag force exerted by the dispersed phase and so lesser will be the peel height.

For single-phase plumes, dimensional analysis gives a prediction for the plume trap height h_T . This is given by the following empirical relation

$$h_T = 2.8 \left(\frac{B}{N^3} \right)^{1/4} \quad (1.1)$$

where B is the initial buoyancy flux of the dispersed phase and N is the Brunt-Vaisälä buoyancy frequency. This relationship has been verified for single-phase plumes from laboratory scales to the scales of forest fires and volcanic eruptions (Turner 1986). However the trap height observed in the case of multiphase plumes is found to deviate significantly from that obtained from the above empirical relation depending on the properties of the dispersed phase. Other important factors include interaction with downdraught plumes, the generation of secondary plumes and entrainment between counterflows. All these processes need to be considered properly in multiphase plume formulations and this is what the various numerical models try to accomplish.

1.1. Multiphase Plume Types

Multiphase plumes can be broadly classified into three categories based on the nature and extent of the peeling phenomenon that the plume undergoes. This classification was made by (Asaeda & Imberger 1993) based on their experiments with bubble plumes in linear stratification. These categories or modes are termed Type 1, 2 and 3 respectively. Type 1 plumes are characterized by the fact that no separation between phases occur until the plume reaches the free surface where all of the entrained fluid in the plume detrains radially outwards as a surface jet. Type 2 plumes on the other hand have multiple separation and peeling events occurring and each intrusion is a distinct layer. Type 3 plumes have the characteristic of having several random secondary peeling mechanisms happening along with entrainment so that they form a continuous structure of sub-surface intrusions. Shown in Figure 2 are the several

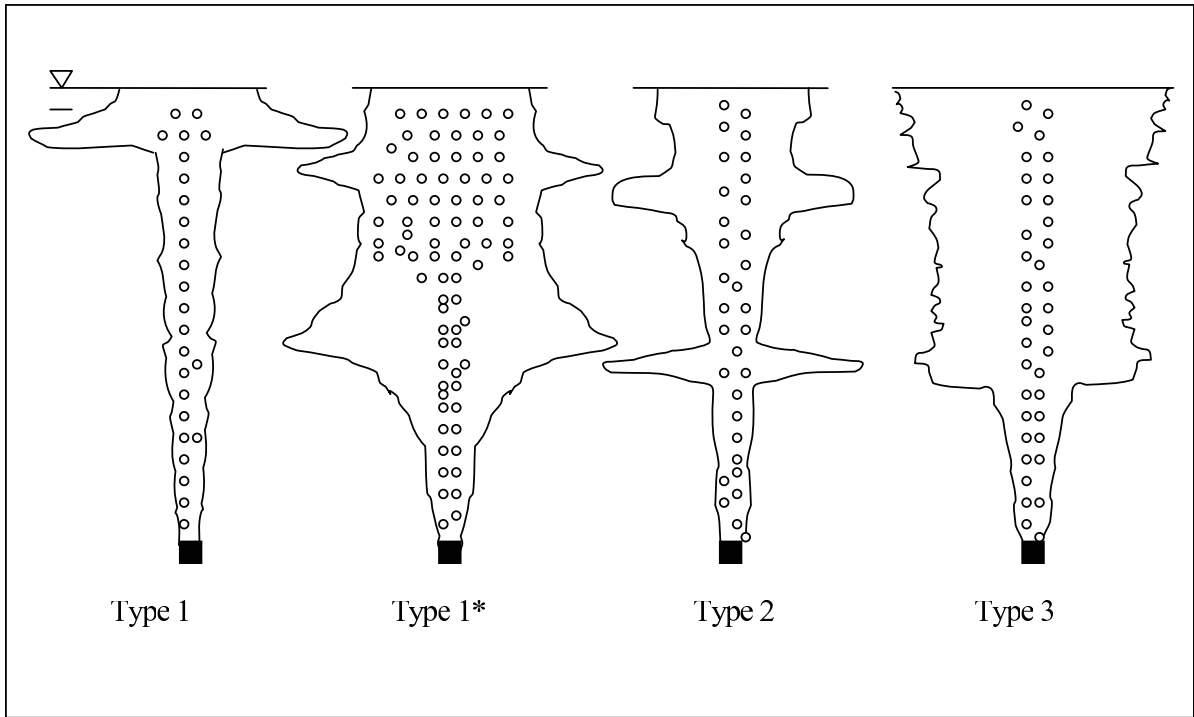


Fig. 2. Types of multiphase plumes

categories of multiphase plumes.

Socolofsky (2001) added one more mode to the list from his experimental observations. He categorised this mode as Type 1* which has the unique feature that peeling of the dispersed phase happens together with the continuous phase. This can happen if the slip velocity of the dispersed phase is low enough compared to the turbulence generated at the peeling locations so that the dispersed phase fails to ascend further. This phenomenon is rare in case of moderate to large air bubble plumes where the slip velocity is typically of the order of 20 cm/s or more. However the slip velocity is found to be as low as 3 - 8 cm/s in case of oil droplets, fine air bubbles or sediments (Socolofsky 2001) and in these cases, the dispersed phase is more spread out after the first peel rather than being localised in an inner core. The dispersed phase eventually rises out of the intrusion and the plume water is re-entrained out of the intrusion and

carried upward by the peeled dispersed phase as they form secondary plumes.

Socolofsky (2001) was also able to make a quantitative classification of multiphase plumes from the experiments with air-bubbles, oil droplets and glass beads which he conducted in a 1.22 m x 1.22 m x 2.44 m deep tank in linear stratification. This classification was based on a non-dimensional parameter U_N called the non-dimensional slip velocity given by

$$U_N = \frac{u_s}{(BN)^{1/4}} \quad (1.2)$$

where u_s is the slip velocity, that is the velocity of the dispersed phase relative to the continuous phase. Based on this parameter Socolofsky (2001) found that Type 1* plumes are generated for values of U_N less than 1.5. Type 2 plumes were found to exist for U_N between 1.5 and 2.4 and for U_N greater than 2.4 the plumes were found to be of Type 3. The Type 1 plumes did not plot in this parameter space since the reservoir depth does not appear in the non-dimensionalization.

2. Numerical Modeling of Multiphase Plumes

Numerical modeling of bubble plumes has been done extensively for lake and reservoir management, both to enhance vertical mixing and to provide reaeration to the hypolimnion (Goossens 1979, Patterson & Imberger 1989, Wüest et al. 1992, Schladow 1993). By using the integral model of McDougall (1978) and by coupling it to the one-dimensional dynamic reservoir model DYRESM, Patterson & Imberger (1989) were able to predict the turn-over time for a reservoir that was mixed by a bubble plume and they subsequently used the model to enhance the plume system design. Wüest et al. (1992) developed a simple integral plume model by including the gas exchange between the bubbles to study the phenomena of reaeration in a lake and mixing in a

reservoir. Their model was aimed at tracking the water quality changes by calculating the concentrations of gases in the reservoir. The knowledge of single-phase plumes has been employed in the mixing zone model CORMIX to predict the steady state mixing behavior and plume geometry for environmental impact assessment of regulatory mixing zones resulting from point source discharges (Jirka, Doneker & Hinton n.d.). With regard to CO₂ plumes, Liro et al. (1992) and Crouse (2000) have used integral models to simulate the release of CO₂ in the ocean. Liro et al. (1992) also proposed to couple the integral model to larger scale oceanographic circulation and transport models to assess the ultimate fate of the released CO₂.

All of the numerical models related to multiphase plumes mentioned in the last paragraph are integral models based on an Eulerian formulation. However researchers have also begun to use integral plume models based on a Lagrangian concept with the JETLAG model coming up in the early 90's developed by Lee & Cheung (1990). However the Lagrangian model has only been applied to model deep sea oil well blowout problems (Yapa & Zheng 1999). Johansen (2000) presented a subsea blowout model which he called DEEPBLOW based on the Lagrangian concept by varying the BLOW model (Rye 1994) that was formulated based on an Eulerian concept. Johansen (2000) successfully applied his Lagrangian model to simulate multiphase plume discharges in the form of water, oil and gas in a stratified water column with variable currents. Recent advances in computational fluid dynamics (CFD) have enabled the possibility to characterize turbulence in bubble plumes by extracting the coherent structures in the flow using a Large Eddy Simulation (LES) approach (Deen, Solberg & Hjertager 2001).

2.1. The Mixed-fluid Model

McDougall (1978) first proposed a double plume model to simulate the dynamics

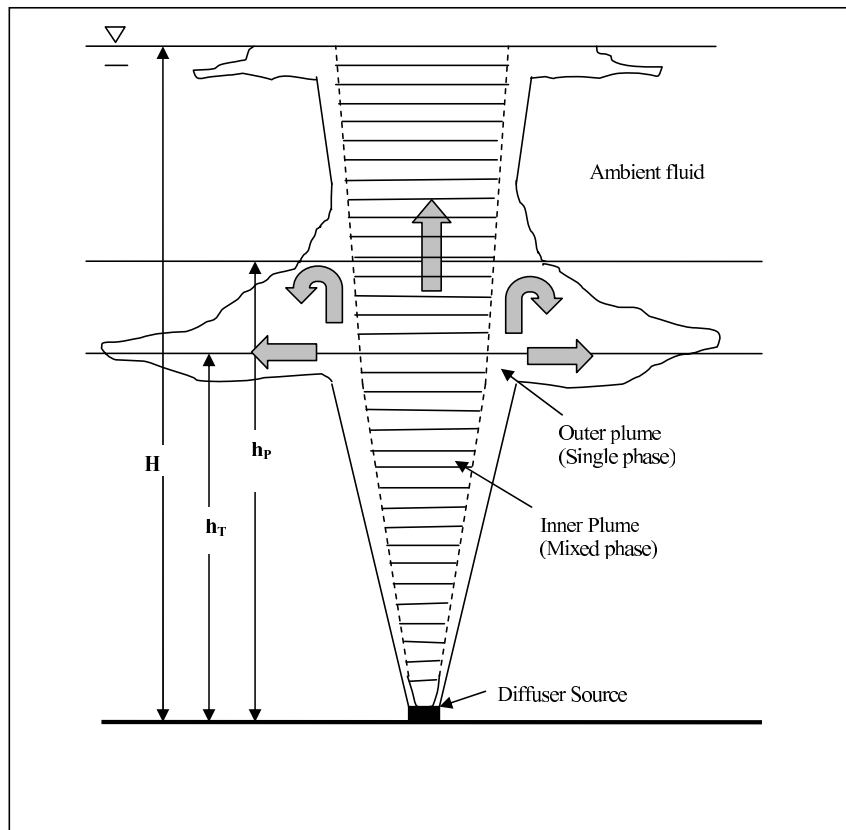


Fig. 3. Double plume model of McDougall(1978)

of multiphase plumes, which he designed to predict the distribution of oil in the water column after an oil-well blowout. This model developed out of experiments he performed in a 0.6 x 0.6 x 1.3 m deep tank. This model was classified as a mixed-fluid model because of the way he treated the buoyancy flux of the dispersed and continuous phases. In his model, he treated the two phases as a single mixture and argued that the multiphase plume created by air-bubbles moving through a surrounding fluid of water consists of an inner plume comprising of an upward rising mixture phase surrounded by an annular outer plume of entrained water from the ambient fluid as shown in Figure 3. The outer plume fluid was considered to rise upward until peeling occurred, when the fraction of the fluid that was negatively buoyant started to descend downward. Thus, in McDougall's model, the outer plume consists of both an ascending and a descending continuous phase.

The double plume model of McDougall (1978) was able to simulate several peeling events, but as was confirmed by Baines & Leitch (1992) in a series of additional experiments in linear and step-stratified environments, it underestimated the level of the first peel in the experiments by up to 40 percent. Asaeda & Imberger (1993) modified the double-plume model of McDougall by changing the definition of the outer plume. They considered the upward rising phases to form the inner plume as a whole and only the descending continuous phase confined within the peel and trap heights to form the outer plume, as shown in Figure 4. They conducted experiments with linear stratification in a 1.0 m x 1.0 m x 0.75 m deep tank and variable bubble source strengths, and their observations led them to develop their modified double plume model. By way of changing the definition of the outer plume and with the incorporation of the corresponding modeling algorithm, they were able to represent multiple peeling events better than McDougall's model.

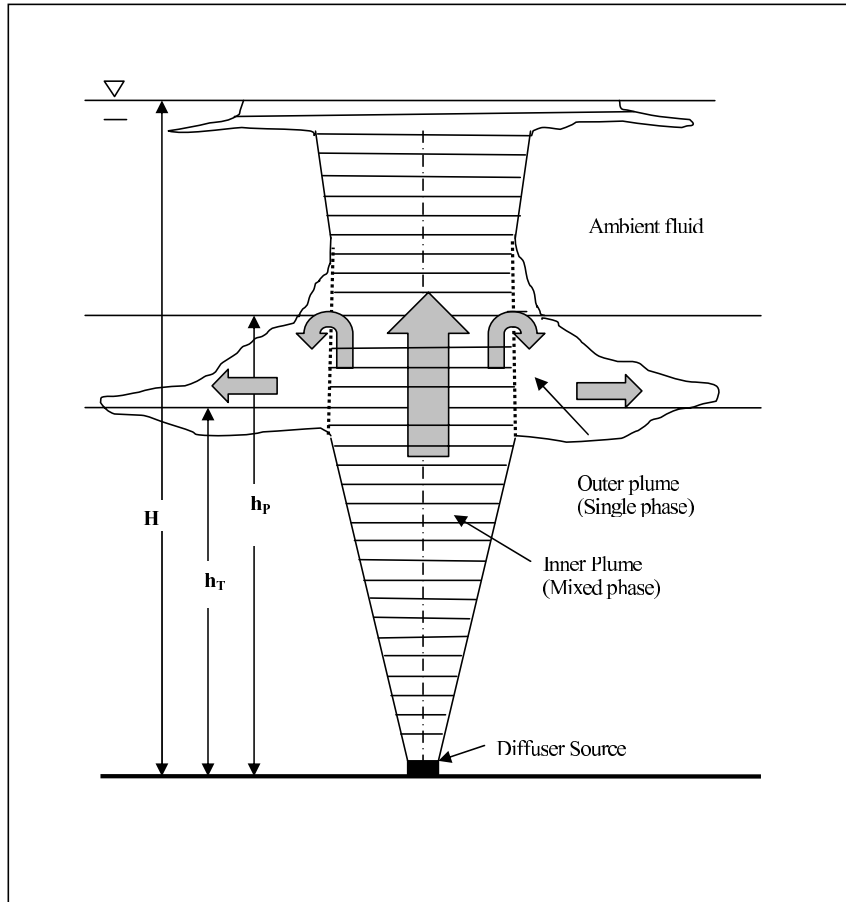


Fig. 4. Double plume model of Asaeda & Imberger(1993)

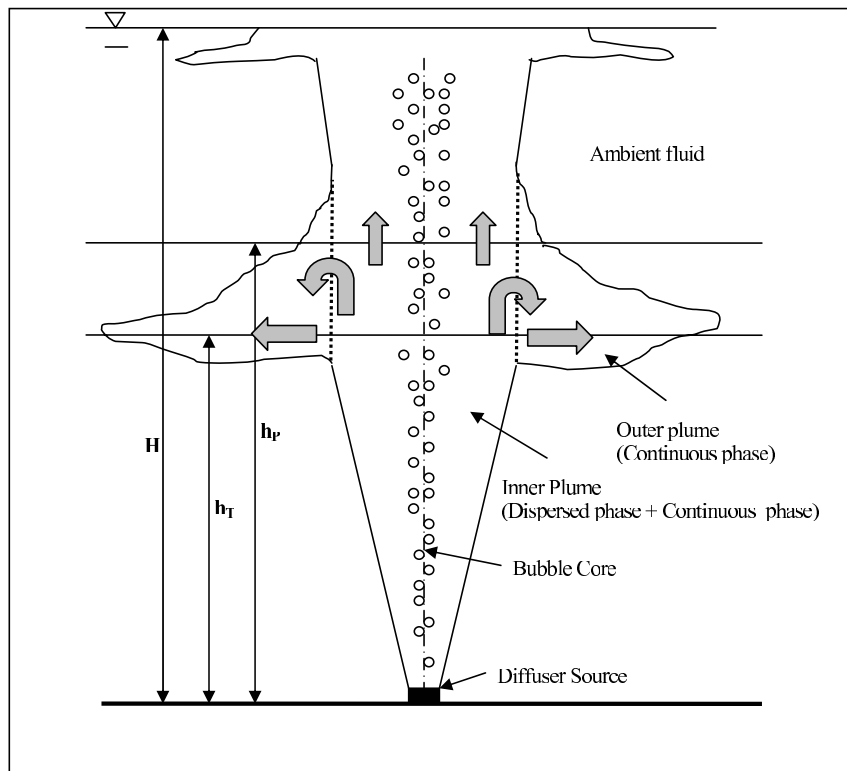


Fig. 5. Double plume model of Socolofsky, Crouse & Adams(2002)

2.2. The Two-fluid Model

The mixed-fluid approach to integral models for multiphase plumes was accepted by researchers until Socolofsky et al. (2002) introduced a slightly different perspective of looking at the physical model, shown schematically in Figure 5. They argued that the plume geometry is best represented if the rising bubble plume is treated by taking the two phases separately in the inner plume of Asaeda & Imberger's model and not as a homogeneous mixture. The outer plume definition was kept the same as that of Asaeda & Imberger (1993) because the outer plume is assumed to be a single-phase plume. Also they identified that the flux of the dispersed phase and continuous phase result from different transport velocities. The dispersed phase was found to have a higher velocity as compared to the continuous phase and this relative velocity was termed the slip velocity. Hence they presented an approach classified as a two-fluid model, with the incorporation of the slip velocity resulting in a separate treatment of the buoyancy flux of the dispersed and continuous phases in the inner plume and using a suitable distribution pattern for the dispersed phase void fraction verified from experiment (Bergmann et al. 2004). Crouse (2000) developed a numerical model including the phenomena of bubble dissolution, bubble expansion and compressibility effects. In the present work, all of these phenomena have been considered too. In addition, an analysis of using the right choice of initial conditions for the numerical models verified from laboratory scale experiments and a judicious choice of the model parameters based on sensitivity analyses are the improvements to the two-fluid model made in the present work.

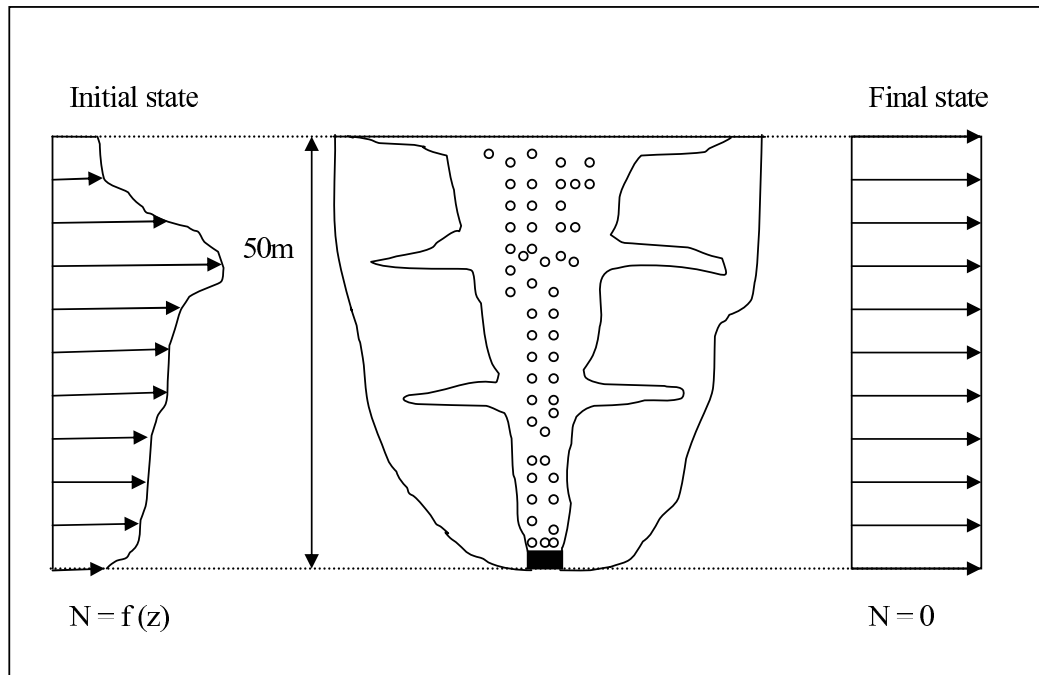


Fig. 6. Destratification of a lake by air-bubble plume

3. Case Studies

3.1. Case 1: Lake Destratification

Reservoir destratification using the kinetic energy of air-bubble plumes is extensively used nowadays. Moreover, artificial destratification of lakes by the use of energetic air-bubble plumes (Figure 6) is one of the commonly used techniques to counter the harmful consequences that thermal stratification during summer has on fish and other aquatic organisms. By injecting air at the bottom of the reservoir or lake at a high enough flow rate it is possible to destroy or modify the existing stratification, and thereby generate a well-mixed system. The present work proposes a hypothetical case in which a lake having a non-linear stratification gradient will be destratified numerically. The lake data has been taken from (Nepf 1995). Hence the two-fluid and the mixed-fluid models will be applied to find the optimal air-flow rate and

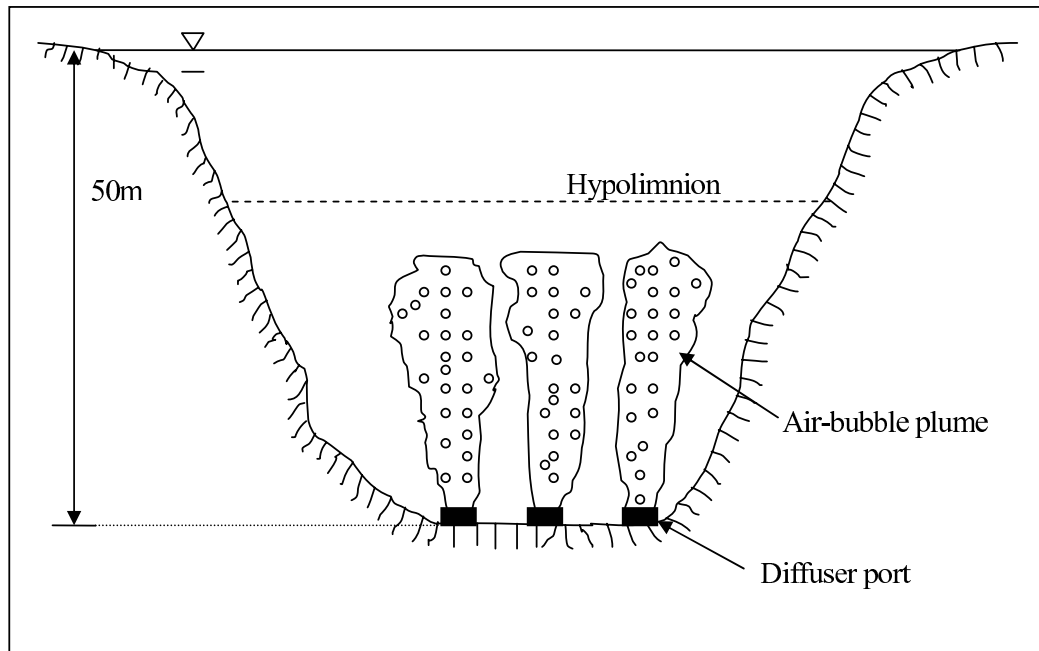


Fig. 7. Aeration of a lake by air-bubble plume

diffuser orifice diameter necessary to destratify the lake and to study a comparison of the corresponding input power and turnover times. The hydrography, temperature and salinity data of the lake is presented in Chapter VII.

3.2. Case 2: Lake Aeration

Lake eutrophication is the rapid aging of a lake in which the water quality of a lake deteriorates due to steady accumulation of mineralized biomass in the hypolimnion leading to depletion of the dissolved oxygen. This can lead to widespread fish kills. In order to prevent the hypolimnion from becoming anoxic during the summer, oxygen can be artificially injected by means of discharge through diffuser ports. The released oxygen forms a multiphase plume of surrounding water until it dissolves in the hypolimnion as seen in Figure 7. To optimize the design of such a diffuser port system, bubble plume models are frequently employed to study the multiphase plume

kinematics.

In the present work, the two-fluid and the mixed fluid models will be compared against each other to see the differences in the depth of maximum plume rise (DMPR) where all of the injected oxygen (air) dissolves. The lake considered is the same (Nepf 1995) as in the last section. Results will be compared between those obtained from the two-fluid model against those from the mixed-fluid model and the DMPR will be the basis of comparison. Also the fate of the different flux variables namely mass, momentum, buoyancy, temperature, concentration and salinity will be tracked as a function of height. Through this analysis, optimal specifications for the diffuser orifice diameter, air-flow rate and the number of such ports necessary to dissolve a measured quantity of air in a given time of operation will also be studied.

3.3. Case 3: CO₂ Sequestration in the Ocean

Sequestration of carbon dioxide and other atmospheric greenhouse gases into the deeper layers of the ocean has recently been proposed by several researchers to serve as one of the alternative measures to mitigate the problem of global warming which the earth is facing today. Carbon dioxide is a greenhouse gas which absorbs the infra-red radiation leaving the earth and reflects it back to earth. This phenomenon can significantly perturb the radiative balance of the earth if ways are not devised to mitigate the release of CO₂ into the atmosphere due to various anthropogenic activities, chiefly the burning of fossil fuels. Hence a proposal was made by a team of researchers (Crouse 2000) to sequester CO₂ into the deeper layers of the ocean where the positively buoyant CO₂ phase would dissolve before being able to escape out of the water surface. However the dynamics of the sequestered gases (or droplets if released in liquid form) and the mixing phenomenon that the sequestered CO₂ phase undergoes with the ambient ocean waters has serious environmental safety concerns

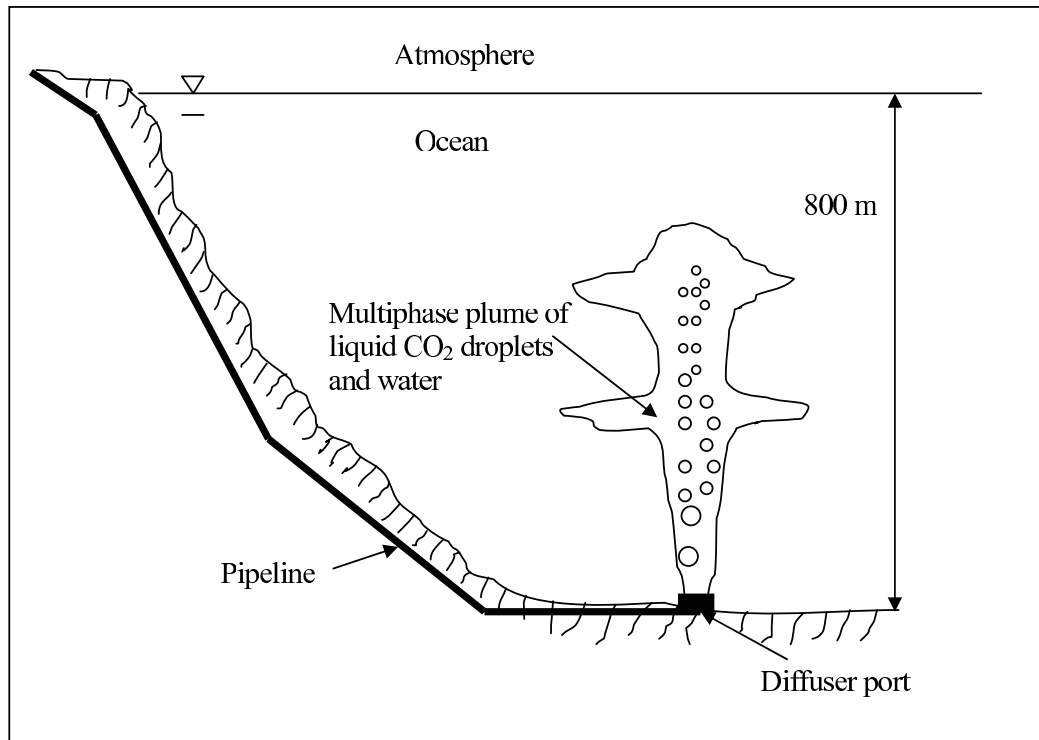


Fig. 8. CO₂ sequestration in ocean

because it will lower the seawater pH in the near field. This necessitates an accurate simulation of the CO₂ sequestration process to determine the requisite depth at which it needs to be released so that all of it dissolves without threatening the habitat of marine life and without posing problems for underwater activities.

Crouse (2000) developed a model of the release of liquid CO₂ droplets in the ocean at a depth of 800m at a rate of 1 kg/s with the objective of studying the feasibility of a CO₂ sequestration technique undertaken in a joint research project by the countries of Japan, Norway, the United States, Canada and Australia as well as the company ABB. Figure 8 represents a rough overview of that proposed scheme. The present work proposes to come up with a CO₂ sequestration scheme on the same lines of (Crouse 2000) but with a different perspective. Here the goal is to see the difference in the predictions of the two-fluid vs. the mixed-fluid model with regard

to the depth at which all of the released CO_2 droplets dissolve for the same release rate and other ambient conditions namely temperature, salinity and dissolved *in-situ* concentration of CO_2 in the ocean water. The sensitivity of the model predictions to the CO_2 mass transfer coefficient to account for the uncertainty involved in the formation of clathrate hydrate film around the surface of the CO_2 droplet (Hirai, Okazaki, Araki, Yazawa, Ito & Hijikata 1996, Warzinski & Holder 1999) will also be studied. The density and hence the phase of CO_2 will also be tracked as it ascends as a function of the pressure, temperature and salinity as given by the CO_2 equation of state described in Appendix A.

4. Thesis Organization

This thesis is divided into eight chapters all of which are centered around numerical modeling of air-bubble and CO_2 droplet plumes. In Chapter I, the basics and applications of multiphase plumes and an overview of the different numerical models and modeling approaches have been outlined. Along with these, the objective of this present work which is the comparative study between the mixed-fluid and two-fluid models with respect to three case studies has been illustrated. The governing equations for the mixed-fluid and the two-fluid models in terms of the flux variables are derived in Chapter II. This includes the relevant additions to the equation for the conservation of buoyancy flux of dispersed phase introduced by Socolofsky et al. (2002). Chapter III is meant to physically and mathematically describe each of the parameters involved in the model equations and how to calculate their values for the case studies. Chapter IV describes the model algorithm, the numerical scheme applied, issues regarding the numerical scheme convergence and demonstrates the functioning of a graphical user interface designed to condense all the computational work involved

in the three case studies. Chapter V deals with the derivation of initial conditions based on the previous works of McDougall (1978), Ditmars & Cederwall (1974) and Wüest et al. (1992) and introduces a new algorithm of obtaining problem-specific initial conditions. A comparison between these different concepts of evaluating the initial conditions is also presented followed by a critical review of issues concerning the sensitivity of the initial conditions to the model outputs. Chapter VI describes the calibration of the model by comparison to two different experimental data obtained by Bergmann et al. (2004) at the Hydromechanics Laboratory, Texas A&M University, College Station, and, by Socolofsky (2001) at the Parsons Laboratory, Massachusetts Institute of Technology, Cambridge. Chapter VII presents the results obtained from the calibrated models for the three case studies. This is followed by a summary section (Chapter VIII) where the conclusions derived out of this present work are listed. The appendix in the end gives details about the computation of the densities of the phases using the Equation of State.

CHAPTER II

GOVERNING EQUATIONS

The governing equations for multiphase plumes are a set of coupled, non-linear ordinary differential equations derived on the basis of the well-established conservation principles and by making the assumption of self-similarity. These equations are the conservation equations for different flux variables which form the state space vector. All of these conservation equations can be written in a form in which the derivative of the state space vector is equated to an expression containing the physical quantities responsible for its change. This form of representing the governing equations enables the computation of the state space vector at each progressive step of the independent variable by numerical integration over each step, and this forms the basis of integral models.

In case of the mixed-fluid integral plume model formulation of McDougall (1978) and Asaeda & Imberger (1993), the state space vector consists of three elements, namely, the volume flux, the momentum flux and the buoyancy flux of the mixture of phases. In their formulations, instead of treating the buoyancy fluxes of the dispersed and continuous phases as separate, they treated them together as a single variable by considering the two phases to form a *mixture* within the plume. The difference between McDougall's and Asaeda & Imberger's model lies in the definition of the outer plume which has been explained in the last chapter.

Wüest et al. (1992) and Crouse (2000) added the conservation equations for heat, temperature and salinity to the integral plume model. They also added the conservation of the mass flux of dispersed phase through which they incorporated the important phenomenon of dispersed phase dissolution into the plume dynamics. They however removed the equation for the buoyancy flux of the mixed phase and

instead calculated the buoyant forces acting on the dispersed and continuous phases separately by calculating the plume fluid density and the dispersed phase density from the equation of state. So both of their formulations should be recognized as two-fluid model formulations.

Socolofsky et al. (2002) proposed the two-fluid model formulation for multiphase plumes in the most explicit form in which the buoyancy flux of the continuous phase is separately treated as a flux variable in the conservation equations as opposed to the buoyancy flux of the *mixture* as was done by McDougall (1978) and Asaeda & Imberger (1993). The buoyancy flux of the dispersed phase is separately treated and it does not appear in the form of a separate conservation equation. This is because it is more convenient to calculate it separately from the equation of state by calculating the dispersed phase density which is a function of the other flux variables, namely, temperature, pressure and salinity; therefore, in doing so, the coupling between the dispersed phase buoyancy flux and the other flux variables is not lost. The major difference in the two-fluid integral plume model of (Socolofsky et al. 2002) from the mixed fluid integral plume model of (McDougall 1978, Asaeda & Imberger 1993) stem from the formulation of the conservation equation for the momentum flux and the incorporation of the relative transport velocity of the dispersed phase. Instead of considering the buoyant force due to a mixture being responsible for the momentum generation for the plume, the net buoyant force due to the difference in the buoyant forces acting on the two phases is considered instead.

The present work is based on the two-fluid model formulations of Socolofsky et al. (2002), Wüest et al. (1992) and Crounse (2000). Thus, in this thesis the proposed numerical model is a two-fluid model in which the state space vector consists of seven elements for the inner plume, namely the conservation equations of volume flux, momentum flux, buoyancy flux of continuous phase, temperature flux, concentration

flux, salinity flux and dispersed phase mass flux. The outer plume has all of the same equations as that of the inner plume except the equation for the dispersed phase mass flux because the outer plume in the two-fluid model formulation is assumed to be devoid of the dispersed phase. The outer plume equations are the same as those derived by Asaeda & Imberger (1993).

To begin with, the governing equations for the two models will be derived by considering only a single plume for simplicity. This will only involve two upward moving phases inside and the entrainment of ambient fluid into the plume. Following this derivation, the more general case of a double plume will be considered by incorporating the outer plume. The derivations are primarily based upon an important assumption called the self-similarity assumption to result in a set of 1-D ordinary differential equations, which is discussed in the next subsection.

1. The Self-Similarity Assumption

The derivation of the governing equations is based on an important assumption called the self-similarity assumption that states - state variables have similar lateral profiles at different plume heights. Self-similarity has been found to be satisfied for the state variables in the zone of established flow for single-phase plumes. Multiphase plumes, however, are often observed to violate self-similarity even in the existence of an unstratified ambient (Bergmann et al. 2004). Nevertheless, this assumption helps to compress the multi-dimensional nature of the problem to one dimension only and hence has been utilized by several researchers (McDougall 1978, Asaeda & Imberger 1993, Wüest et al. 1992, Socolofsky et al. 2002).

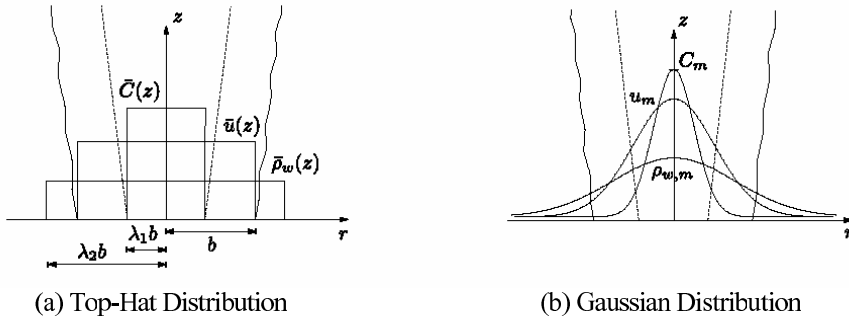


Fig. 9. Top-hat and Gaussian distribution for the state variables

1.1. Gaussian and Top-Hat Distribution

Gaussian (McDougall 1978) or Top-Hat (Asaeda & Imberger 1993) profiles are the typical choices for representing the lateral variation of state variables, as represented in Figure 9. Both of these distributions involve two independent variables: the radial coordinate r and the vertical coordinate z . The Gaussian and Top-Hat profiles are respectively given by the following expressions:

Gaussian:

$$X(r, z) = X_m(z) \exp\left(-\frac{r^2}{\lambda^2 b(z)^2}\right) \quad (2.1)$$

Top-Hat:

$$X(r, z) = \begin{cases} \bar{\chi}(z) & -\lambda b(z) \leq r \leq \lambda b(z), \\ 0 & \text{otherwise} \end{cases} \quad (2.2)$$

Here X is the state variable of interest, $X_m(z)$ or $\bar{\chi}(z)$ is the centerline value of the state variable X , depending on whether the distribution is Gaussian or Top-Hat, $b(z)$ is the characteristic profile half-width, and λ is a scaling factor that allows different state variables to have a characteristic width proportional to the half-width $b(z)$. Each of these variables changes with height due to entrainment. The variables of interest

are namely the plume velocity u , the bubble void fraction c and the reduced gravity g' of the plume fluid. For $X = u$, $\lambda = 1$, for $X = c$, $\lambda = \lambda_1$ and for $X = g'$, $\lambda = \lambda_2$.

Eq. (2.1) when integrated in the radial direction from 0 to ∞ and through 2π radians of rotation reduces the number of independent variables from three to one. This integration process can be generalized to all heights by the help of the self-similarity assumption. Thereby, a system of non-linear ordinary differential equations is obtained in which the derivatives of the integral fluxes are obtained as functions of the fluxes themselves with respect to only one independent variable, the vertical coordinate z .

1.2. Relationship between Gaussian and Top-Hat Variables

The governing equations can be derived using either of the distributions for the state variables - Top-Hat or Gaussian. McDougall (1978) used Gaussian profiles for deriving the equations for the mixed-fluid model. This was later on replaced by the Top-Hat version by Asaeda & Imberger (1993). In deriving the two-fluid model equations for Socolofsky et al. (2002), the Top-Hat version will be used. The corresponding equations for the Gaussian case can be derived by adjusting the state variables u and b and the entrainment coefficient α in the equations as follows:

$$\begin{aligned}\bar{u} &= \frac{u_m}{2}, \\ b_{th} &= \sqrt{2}b_g, \\ \alpha_{th} &= \sqrt{2}\alpha_g\end{aligned}\tag{2.3}$$

This derivation is based on the principle that the volume and momentum fluxes of the plume are the same irrespective of the choice of the type of distribution for the variables inside the plume.

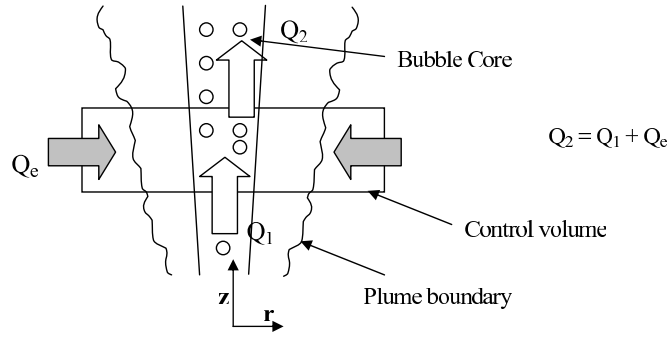


Fig. 10. The entrainment hypothesis

2. Conservation Equations

To derive the conservation equations, we follow the Eulerian reference frame in which the flux terms are considered entering and leaving a cylindrical control volume of radius equal to the plume radius b and thickness dz fixed in space and time. Next, we consider the density of the fluid inside the control volume to remain locally invariant. This assumption leads to cancellation of the density term from both sides of the mass conservation equation so that the mass terms for the continuous phase essentially reduces to corresponding volume terms. Next, the reference frame is chosen such that the vertical coordinate z is positive upwards with the origin at the diffuser source. Also, all forces are considered positive along the positive z direction.

2.1. Single Plume Model Equations

2.1.1. Conservation of Volume Flux

The general expression for the volume flux Q across a cross-section of this cylindrical control volume is given as follows:

$$Q(z) = \int_0^b u(z, r)(1 - c(z, r))2\pi r dr + \int_0^b u_b(z, r)c(z, r)2\pi r dr \quad (2.4)$$

where u_b is the velocity of the dispersed phase.

For Gaussian profiles

$$u_b(z) = U_m + (1 + \lambda_1^2)u_s \quad (2.5)$$

and for Top-Hat profiles

$$u_b(z) = \bar{u} + u_s \quad (2.6)$$

where u_s is the slip velocity, that is, the velocity of the dispersed phase relative to that of the continuous phase.

The integration involved in the R.H.S of Eq. (2.4) is simplified if we make use of the dilute plume assumption by arguing that the dispersed phase void fraction $c(z, r)$ is small so that $(1 - c(z, r)) \sim 1$ and $c(z, r) \sim 0$. Hence we obtain

$$Q(z) = \pi b^2 \bar{u} \quad (2.7)$$

Finally, we resort to the famous entrainment hypothesis (Figure 10) by Morton, Taylor & Turner (1956) which states that the induced entrainment velocity u_e at the boundary of a turbulent plume is proportional to a characteristic velocity within the plume. For a multiphase plume, we take the centerline velocity u_c of the continuous phase as the characteristic plume velocity. For the particular choice of a Top-Hat profile for the state variable u we have from Eq. (2.2), $u_c = \bar{u}$ and hence by the entrainment hypothesis we can write

$$u_e = \alpha \bar{u} \quad (2.8)$$

where α is the *turbulent entrainment coefficient*. Now the change in volume flux dQ inside the control volume for a steady flow is equal to the entrained volume flux which is given by the product of the entrainment velocity u_e and the circumferential area

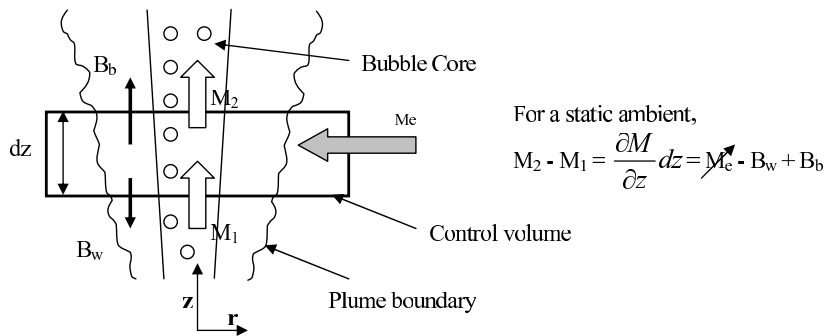


Fig. 11. Conservation of momentum inside control volume

$2\pi b dz$ of the control volume so that from Eq. (2.4), Eq. (2.7) and Eq. (2.8) we obtain the conservation of volume flux equation as follows:

$$\frac{d}{dz} (\pi b^2 \bar{u}) = 2\pi b \alpha \bar{u} \quad (2.9)$$

2.1.2. Conservation of Momentum Flux

The conservation of momentum is basically Newton's 2nd law of motion which says that a direct proportionality exists between the rate of change of momentum and the driving force. In a multiphase plume, this driving force is attributed to buoyancy. In this context, the two-fluid model differs from the mixed-fluid model in the way the net buoyant force acting on the plume is treated. In the mixed-fluid model, the dispersed phase (bubbles, droplets or particles) and the continuous phase (water) are treated as a mixture which gives rise to only one buoyant force term for the mixture as a whole. In case of the two-fluid model however there is a clear distinction between the dispersed and continuous phases and buoyant forces on each are calculated separately to compute the net applied force responsible for the momentum generation (Figure 11). The buoyancy of either phase drives the plume against gravity in the case each is lighter than the ambient fluid or towards gravity in the case of a lighter

ambient.

Thus from Newton's 2nd law, for the two-fluid model we can write

$$\frac{dJ}{dz} = \hat{B}_{dispersed} + \hat{B}_{continuous} \quad (2.10)$$

where J is the rate of change of momentum flux, $\hat{B}_{dispersed}$ is the buoyant force acting due to the dispersed phase and $\hat{B}_{continuous}$ is the buoyant force acting due to the continuous phase. For the mixed-fluid model we have,

$$\frac{dJ}{dz} = \hat{B}_{mixture} \quad (2.11)$$

where $\hat{B}_{mixture}$ is the buoyant force acting on the mixture phase.

The rate of change of momentum flux, J is given by

$$J(z) = \gamma \left[\int_0^b u^2(z, r)(1 - c(z, r))2\pi r dr + \int_0^b u_b^2(z, r)c(z, r)2\pi r dr \right] \quad (2.12)$$

γ is a momentum amplification factor that accounts for the added momentum of the turbulence above that of the mean flow (Milgram 1983). $c(z, r)$, as defined before, is the void fraction of the dispersed phase, which accounts for the fact that the plume width is not entirely occupied by bubbles. Using the dilute plume assumption, the momentum of the dispersed phase can be neglected in comparison to that of the continuous phase. The net momentum is therefore $\pi b^2 \bar{u}^2$ for both models, obtained by integrating the R.H.S of Eq. (2.12). The buoyant forces of each phase are however not negligible. These are given by:

$$\hat{B}_{continuous} = \int_0^{\min(\lambda_1 b, \lambda_2 b)} \frac{\Delta \rho_w}{\rho_r} g u(z, r)(1 - c(z, r))2\pi r dr \quad (2.13)$$

where subscript w is for water (continuous phase), and

$$\hat{B}_{dispersed} = \int_0^{\min(\lambda_1 b, \lambda_2 b)} \frac{\Delta \rho_b}{\rho_r} g u_b(z, r)c(z, r)2\pi r dr \quad (2.14)$$

where subscript b is for bubbles (dispersed phase). $\Delta\rho_w = \rho_a - \rho_w$ and $\Delta\rho_b = \rho_a - \rho_b$.

Hence using Eq. (2.10) to Eq. (2.14) we get the equation for conservation of momentum flux as:

$$\frac{d}{dz} (\pi b^2 \bar{u}^2) = \frac{\pi b^2}{\gamma} \left(\lambda_1^2 \bar{c} \frac{\Delta\rho_b g}{\rho_r} + \lambda_2^2 \frac{\Delta\rho_w g}{\rho_r} \right) \quad (2.15)$$

for the two-fluid model, and

$$\frac{d}{dz} (\pi b^2 \bar{u}^2) = \frac{\pi b^2}{\gamma} \left(\lambda^2 \frac{\Delta\rho_{mix} g}{\rho_r} \right) \quad (2.16)$$

for the mixed-fluid model. In this derivation, no additional momentum flux is added due to entrainment because the ambient fluid is assumed to have zero vertical momentum.

The momentum amplification for the mean flow is less for increased turbulence and so the factor γ has a value greater than or equal to 1 since it appears in the denominator in the R.H.S of Eq. (2.15) and Eq. (2.16). Hence we have

$$\hat{B}_{dispersed} = \frac{\Delta\rho_b g}{\rho_r} \pi b^2 (\bar{u} + u_s) \bar{c} \lambda_1^2 \quad (2.17)$$

$$\hat{B}_{continuous} = \frac{\Delta\rho_w g}{\rho_r} \pi b^2 \bar{u} (1 - \bar{c}) \lambda_2^2 \quad (2.18)$$

$$\hat{B}_{mixture} = \frac{\Delta\rho_{mix} g}{\rho_r} \pi b^2 \bar{u} \lambda^2 \quad (2.19)$$

and

$$\Delta\rho_{mix} = \bar{c} \Delta\rho_b + (1 - \bar{c}) \Delta\rho_w \quad (2.20)$$

λ_1 is the spreading ratio between the bubble concentration and plume velocity profile (generally less than 1), λ_2 is the spreading ratio between the continuous phase buoyancy and velocity profile (generally greater than 1), and λ is the spreading ratio between the buoyancy and velocity profile for the mixed-fluid model.

From Eq. (2.17), Eq. (2.18), Eq. (2.19) and Eq. (2.20) it can be shown by algebraic manipulation that

$$\begin{aligned} \hat{B}_{mixture} = & \left(\hat{B}_{dispersed} + \hat{B}_{continuous} \right) + \\ & \left[\frac{\Delta\rho_b g}{\rho_r} \pi b^2 (\bar{u} + u_s) \bar{c} (\lambda^2 - \lambda_1^2) + \frac{\Delta\rho_w g}{\rho_r} \pi b^2 \bar{u} (1 - \bar{c}) (\lambda^2 - \lambda_2^2) \right. \\ & \left. - \frac{\Delta\rho_b g}{\rho_r} \pi b^2 u_s \bar{c} \lambda^2 \right] \end{aligned} \quad (2.21)$$

Thus, $\hat{B}_{mixture} = \hat{B}_{dispersed} + \hat{B}_{continuous}$ if and only if $u_s = 0$ and $\lambda_1 = \lambda_2 = \lambda$. In case of multiphase plumes, $u_s \neq 0$ in general and usually $\lambda_1 < \lambda_2$. Therefore, in general

$$\hat{B}_{mixture} \neq \left(\hat{B}_{dispersed} + \hat{B}_{continuous} \right) \quad (2.22)$$

Therefore, the momentum flux predicted by the two-fluid model will be different from that predicted by the mixed-fluid model. The sign and magnitude of this difference can be obtained from the term in brackets in Eq. (2.21). This difference in non-dimensional form is given as

$$\begin{aligned} \eta = & \frac{\hat{B}_{mixture} - \left(\hat{B}_{dispersed} + \hat{B}_{continuous} \right)}{\left(\hat{B}_{dispersed} + \hat{B}_{continuous} \right)} \\ = & \left[\frac{\left(1 + \frac{u_s}{\bar{u}} \right) \left(\frac{\lambda_1}{\lambda} \right)^2 + \left(\frac{\Delta\rho_w}{\Delta\rho_b} \right) \left(\frac{1}{\bar{c}} - 1 \right) \left(\frac{\lambda_2}{\lambda} \right)^2}{1 + \left(\frac{\Delta\rho_w}{\Delta\rho_b} \right) \left(\frac{1}{\bar{c}} - 1 \right)} \right]^{-1} - 1 \end{aligned} \quad (2.23)$$

For the particular case when $\lambda_1 = \lambda_2 = \lambda = 1$ and $u_s = 0$, it is seen that Eq. (2.23) simplifies to $\eta = 0$.

For typical values of $\bar{c} = 0.01$, $u_s = \bar{u} \neq 0$ (that is, the bubbles move twice as fast as the continuous phase), $\lambda_1 = 0.8$, $\lambda_2 = \lambda = 1.0$, $\Delta\rho_w = -2 \text{ kg/m}^3$ and $\Delta\rho_b = 998 \text{ kg/m}^3$ (for air bubbles), Eq. (2.23) gives $\eta = -0.26$, which means that the mixed-fluid model differs in the prediction of the net buoyant force acting on the continuous

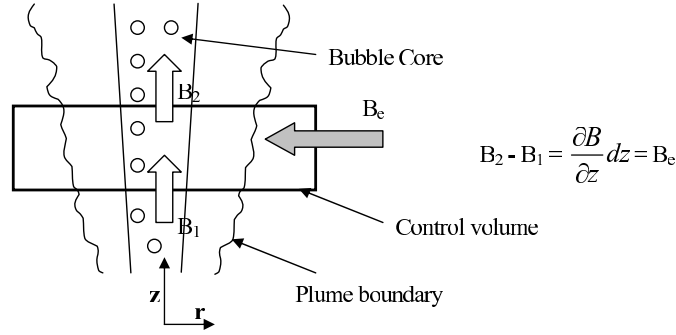


Fig. 12. Conservation of buoyancy inside control volume

phase by 26% in case of air-bubble plumes, which is quite significant. In case of CO_2 plumes, typically $\Delta\rho_b = 70 \text{ kg/m}^3$ and this gives $\eta = -0.21$. Qualitatively, this difference will increase with increase in the value of the slip velocity and will also depend on the relative values of the spreading ratios, density stratification of the ambient and change in the density of the dispersed phase with depth.

2.1.3. Conservation of Buoyancy Flux

The conservation of buoyancy flux can be derived by using the physical fact that the change in buoyancy flux B with height z across any level of the plume is due to the buoyancy flux B_e of the entrained fluid (Figure 12). This leads to the following equation:

$$\frac{\partial B}{\partial z} dz = B_e \quad (2.24)$$

where

$$B = \int_0^b (\rho_r - \rho_w) u(r, z) (1 - \bar{c}) 2\pi r dr + \int_0^{\lambda_1 b} (\rho_r - \rho_w) u_b \bar{c} 2\pi r dr \quad (2.25)$$

and

$$B_e = \int_0^b (\rho_r - \rho_a) \alpha u(r, z) 2\pi r dr \quad (2.26)$$

In this respect, we use the Boussinesq approximation which states that *only density differences are important for buoyancy terms*. As a result of this approximation, it is possible to formulate the buoyancy flux terms relative to a constant reference density ρ_r . Therefore, in deriving the conservation equations for the buoyancy flux, the density differences between the constituents and the reference density are taken into account as seen in Eq. (2.25) and Eq. (2.26). The density difference of the continuous phase (the plume fluid) changes with height due to entrainment of fluid of different density at each successive level of height in case of a stratified ambient and this gives rise to the classic plume buoyancy equation for the continuous phase (Morton et al. 1956) as follows:

$$\frac{d}{dz} \left(\frac{\pi \lambda^2 b^2 \bar{u} g'_w}{1 + \lambda^2} \right) = -\pi b^2 \bar{u} N^2 \quad (2.27)$$

where N is the Brunt-Vaisala buoyancy frequency ($= 0$ in case of an unstratified ambient) given by

$$N^2 = -\frac{g}{\rho_r} \frac{d\rho_a}{dz} \quad (2.28)$$

The buoyancy conservation equation for the mixed-fluid model (McDougall 1978) is given by the following equation:

$$\frac{d}{dz} (\pi \lambda^2 b^2 \bar{u} g'_{mix}) = -\pi b^2 \bar{u} N^2 + \frac{g Q_0 H_A \bar{u}}{(H_T - z)^2 (\bar{u} + (1 + \lambda_1^2) u_s)^2} \left[\bar{u} (\bar{u} + (1 + \lambda_1^2) u_s) + (1 + \lambda_1^2) u_s (H_T - z) \frac{d\bar{u}}{dz} \right] \quad (2.29)$$

In this derivation it was assumed that the bubble slip velocity does not vary with

depth ($\frac{du_s}{dz} = 0$). The main error in this equation is that g'_{mix} is transported at the velocity \bar{u} of the continuous phase \bar{u} while g'_{mix} includes both the continuous as well as the dispersed phases. Hence, the dispersed phase slip velocity u_s is not properly accounted for in this transport equation for the mixed fluid model.

2.1.4. Conservation of Temperature Flux

The conservation of temperature flux is derived on the basis of the fact that the change in the heat content of the plume inside the control volume is due to the heat of the entrained fluid and the heat released due to dissolution of the dispersed phase.

This is expressed by the following equation:

$$\frac{d}{dz}(\pi b^2 \bar{u} T) = 2\pi b \alpha \bar{u} T_e + \frac{\Delta H_{sol}}{\rho_w C_p} \quad (2.30)$$

where T is the temperature of the continuous phase, T_e is the temperature of the entrained ambient fluid, ΔH_{sol} is the heat of dissolution of the dispersed phase, ρ_w is the density of the continuous phase and C_p is the specific heat of the continuous phase.

2.1.5. Conservation of Concentration Flux

The conservation of concentration flux is derived on the basis of the fact that the change in the concentration of plume fluid inside the control volume is due to the concentration of the entrained fluid and due to the concentration of the dissolved dispersed phase. This is expressed by the following equation:

$$\frac{d}{dz}(\pi b^2 \bar{u} c) = 2\pi b \alpha \bar{u} c_e + \frac{4\pi b^2 N_b}{(\bar{u} + u_b)} \beta (C_s - c) \quad (2.31)$$

where c is the concentration of the continuous phase inside the plume, c_e is the concentration of the entrained ambient fluid and $C_s [M/L^3]$ is the solubility of the

dispersed phase.

2.1.6. Conservation of Salinity Flux

The conservation of salinity flux is derived on the basis of the fact that the change in the salinity of the plume inside the control volume is due to the salinity of the entrained fluid. This is expressed by the following equation:

$$\frac{d}{dz}(\pi b^2 \bar{u} s) = 2\pi b \alpha \bar{u} s_e \quad (2.32)$$

where s is the salinity of the continuous phase inside the plume and s_e is the salinity of the entrained ambient fluid.

2.1.7. Conservation of Mass Flux of Dispersed Phase

The rate of mass transfer, or dissolution of dispersed phase is described by the empirical Ranz-Marshall equation (Crounse 2000) given by

$$\frac{dm_b}{dt} = -\pi d_b^2 \beta (C_s - c_i) \quad (2.33)$$

where m_b is the mass of a single dispersed phase droplet, d_b is the diameter of the dispersed phase droplet, $\beta[L/T]$ is a mass transfer coefficient, $C_s[M/L^3]$ is the solubility of the dispersed phase and C_i is the concentration of the *insitu* dissolved dispersed phase inside the plume.

Multiplying Eq. (2.33) by the number flux Φ_b of dispersed phase and dividing by the nominal dispersed phase velocity $(\bar{u} + u_b)$ gives the conservation equation for the mass flux of dispersed phase as follows:

$$\frac{d\dot{m}}{dz} = -\Phi_b \pi d_b^2 \frac{K(C_s - c_i)}{(\bar{u} + u_b)} \quad (2.34)$$

2.2. Closure Equations

To close the system of equations Eq. (2.9) to Eq. (2.34) two more equations to compute the dispersed phase buoyancy and the dispersed phase slip velocity are needed. These are now discussed one after another.

2.2.1. Buoyancy Flux of Dispersed Phase

The variation of the buoyancy flux of the dispersed phase is not best described by the change in ambient stratification, rather it is dominated by the phenomena of the dispersed phase expansion and dissolution. These two phenomena are explained by the equation of state which is given by:

$$pQ_b = Z\dot{m}RT \quad (2.35)$$

where p is the total pressure at a height z above the diffuser source, Q_b is the volume flux of the bubbles at that height, \dot{m} is the mass flow rate of the bubbles, R is the universal gas constant, Z is a compressibility factor (equal to 1 for an ideal gas at STP and equal to about 0.14 for CO₂ droplets at 800 m depth in the ocean) and T is the absolute temperature of the medium. In the present work, the phenomenon of bubble dissolution is considered and hence \dot{m} varies with depth and vanishes when all of the dispersed phase dissolves in the medium. Z is found to remain fairly constant with depth, so that we have

$$p_0Q_0 = Z_0\dot{m}_0RT_0 \quad (2.36)$$

where p_0 is the pressure at the diffuser level ($z = 0$), T_0 is the absolute temperature at the diffuser level and Q_0 is the flow rate of dispersed phase at STP.

From Eq. (2.35) and Eq. (2.36) we have

$$\begin{aligned}
Q_b(z) &= Q_0 \frac{p_0}{p} \frac{T}{T_0} \frac{\dot{m}}{\dot{m}_0} \frac{Z}{Z_0} \\
&= \frac{Q_0}{T_0 Z_0 \dot{m}_0} \frac{\rho_A g H_T T Z \dot{m}}{\rho g (H_A + H - z)} \\
&= \left(\frac{Q_0 H_T}{\dot{m}_0 T_0 Z_0} \right) \frac{T Z \dot{m}}{H_T - z}
\end{aligned} \tag{2.37}$$

Here again we use the Boussinesq approximation by which we use $\rho_A \approx \rho$. The bubble buoyancy flux is given by

$$B_b(z) = \frac{\Delta \rho_b}{\rho_r} g Q_b(z) \tag{2.38}$$

From Eq. (2.37) and Eq. (2.38) we can write the equation of buoyancy flux for the dispersed phase explicitly as follows:

$$B_b(z) = \left(\frac{\Delta \rho_b}{\rho_r} g \right) \frac{Q_0 H_T}{\dot{m}_0 T_0 Z_0} \frac{T Z \dot{m}}{H_T - z} \tag{2.39}$$

and also it is given by the following expression:

$$\begin{aligned}
B_b(z) &= \int_0^b \frac{\Delta \rho_b}{\rho_r} g (u(r, z) + u_s) c(r, z) 2\pi r dr \\
&= \frac{\Delta \rho_b}{\rho_r} g \pi \lambda_1^2 b^2 (\bar{u} + u_s) \bar{c}
\end{aligned} \tag{2.40}$$

From Eq. (2.39) and Eq. (2.40) it is possible to calculate the dispersed phase void fraction, which is given by the following expression:

$$\bar{c}(z) = \left[\frac{\dot{m}}{\dot{m}_0} \frac{T}{T_0} \frac{Z}{Z_0} \frac{H_T}{(H_T - z)} \right] \frac{Q_0}{\pi b^2 (\bar{u} + u_s)} \tag{2.41}$$

2.2.2. Slip Velocity of Dispersed Phase

The slip velocity of the dispersed phase is calculated using relationships in Clift, Grace & Weber (1978) which are based on several non-dimensional numbers, namely the

Morton number, M , the Eötvös number, E_o , and the Reynolds number R_e defined as

$$M = \frac{g\mu^4\Delta\rho}{\rho^2\sigma^3} \quad (2.42)$$

$$E_o = \frac{g\Delta\rho d_e^2}{\sigma} \quad (2.43)$$

$$R_e = \frac{\rho d_e u_s}{\mu} \quad (2.44)$$

where μ is the viscosity of the continuous phase, $\Delta\rho$ is the density difference between the ambient and the continuous phase within the plume, ρ is the density of the continuous phase, σ is the surface tension of water, d_e is the diameter of the dispersed phase and u_s is the slip velocity which is the velocity of the dispersed phase relative to the continuous phase inside the plume. Hence, u_s is computed based on the following algorithm:

$$H = \frac{4}{3}E_oM^{-0.149}\left(\frac{\mu}{\mu_b}\right)^{-0.14} \quad (2.45)$$

$$J = \begin{cases} 0.94H^{0.757} & \text{if } 2 < H \leq 59.3, \\ 3.42H^{0.441} & \text{if } H > 59.3 \end{cases} \quad (2.46)$$

$$R_e = M^{-0.149}(J - 0.857) \quad (2.47)$$

where μ_b is the viscosity of the dispersed phase.

2.3. Double Plume Model Equations

The double plume consists of an ascending inner plume of dispersed and continuous phases and a descending outer plume consisting only of the peeled or detrained continuous phase confined in between the peel and trap heights. The governing equations for the double-plume, mixed-fluid model has been derived previously by Asaeda & Imberger (1993). The corresponding equations for the two-fluid model

of Socolofsky (2001) will now be derived. This will involve a few additional terms depending on the entrainment phenomena just the way Asaeda & Imberger did before.

These are:

1. Entrainment of fluid from the outer to the inner plume
2. Detrainment of fluid from the inner to the outer plume
3. Entrainment of fluid from the ambient to the outer plume

The corresponding entrainment coefficients will be denoted as α_1 , α_2 and α_3 respectively. The other important aspect in the dynamics of double plumes is the modification of the entrainment hypothesis by (Asaeda & Imberger 1993) which says that the entrainment to the inner plume is proportional to the difference in velocities of the inner and outer plumes, whereas the entrainment to the outer plume is proportional to the velocity of the outer plume only. With this assumption, the double plume equations have been derived separately for the inner and the outer plumes for the two-fluid model and are represented below. The subscript i denotes parameters concerning inner and the subscript o for outer plumes.

2.3.1. Inner Plume Equations

1. Conservation of Volume Flux:

The conservation of volume flux equation for the inner plume is obtained by equating the rate of change of mass flux with height to the mass flux of the entrained and detrained mass fluxes to and from the inner plume as represented below:

$$\frac{d}{dz} (\pi b^2 \bar{u}) = 2\pi b \alpha_1 (\bar{u} - \bar{v}) + 2\pi b \alpha_2 \bar{v} \quad (2.48)$$

In Eq. (2.48), v is positive in the direction against gravity.

2. Conservation of Momentum Flux:

In case of a single plume, the rate of change of momentum flux is simply equal to the net forces of buoyancy of the dispersed and continuous phases. However in case of double plumes, two additional terms need to be considered for inner plumes. These are the entrained momentum flux to the inner plume with the outer plume velocity \bar{v} and the detrained momentum flux from the inner to the outer plume plume with the inner plume velocity \bar{u} .

$$\frac{d}{dz} (\pi b^2 \bar{u}^2) = \frac{1}{\gamma} (\pi b^2 \lambda_1^2 \bar{c} g_b' + \pi b^2 \lambda_2^2 g_w' + 2\pi b \alpha_1 (\bar{u} - \bar{v}) \bar{v} + 2\pi b \alpha_2 \bar{v} \bar{u}) \quad (2.49)$$

3. Conservation of Buoyancy Flux of Continuous Phase:

In the conservation of buoyancy flux of the continuous phase for the inner plume, the two additional terms are the entrained and detrained buoyancy fluxes. This is represented in the equation below:

$$\frac{d}{dz} (\pi b^2 \bar{u} g_w') = -\pi b^2 \bar{u} N^2 + 2\pi b \alpha_1 (\bar{u} - \bar{v}) g_{wo}' + 2\pi b \alpha_2 \bar{v} g_{wi}' \quad (2.50)$$

where

$$g_{wi}' = \frac{(\rho_a - \rho_{wi})}{\rho_r} g \quad g_{wo}' = \frac{(\rho_a - \rho_{wo})}{\rho_r} g$$

4. Conservation of Buoyancy Flux of Dispersed Phase:

The conservation of buoyancy flux for the dispersed phase for the inner plume of a double plume remains the same as that of a single plume because it is assumed that there are no bubbles present in the outer plume.

5. Conservation of Temperature Flux:

An additional term in the equation for conservation of temperature flux of the inner plume is due to the detrainment from the inner to the outer plume, and

hence the equation is given as follows:

$$\frac{d}{dz}(\pi b^2 \bar{u} T_i) = 2\pi b \alpha_1 (\bar{u} - \bar{v}) T_o + 2\pi b \alpha_2 \bar{v} T_i + \frac{\Delta H_{sol}}{\rho_w C_p} \quad (2.51)$$

where T_i and T_o are the *insitu* temperatures of the continuous phase in the inner and outer plume respectively.

6. Conservation of Concentration Flux:

An additional term in the equation for conservation of concentration flux of the dissolved dispersed phase of the inner plume is due to the detrainment from the inner to the outer plume, and hence the equation is given as follows:

$$\frac{d}{dz}(\pi b^2 \bar{u} c_i) = 2\pi b \alpha_1 (\bar{u} - \bar{v}) c_o + 2\pi b \alpha_2 \bar{v} c_i + \frac{4\pi b^2 N_b}{(\bar{u} + u_b)} \beta (C_s - c_i) \quad (2.52)$$

where c_i and c_o are the dissolved *insitu* concentrations of the dispersed phase in the inner and outer plume respectively.

7. Conservation of Salinity Flux:

An additional term in the equation for conservation of salinity of the inner plume is due to the detrainment from the inner to the outer plume, and hence the equation is given as follows:

$$\frac{d}{dz}(\pi b^2 \bar{u} s_i) = 2\pi b \alpha_1 (\bar{u} - \bar{v}) s_o + 2\pi b \alpha_2 \bar{v} s_i \quad (2.53)$$

where s_i and s_o are the *insitu* salinities of the continuous phase in the inner and outer plumes respectively.

8. Conservation of Mass Flux of Dispersed Phase:

The conservation of mass flux of the dispersed phase in case of a double plume remains the same as that in case of a single plume because the outer plume is considered to be devoid of dispersed phase. Noting that d_b is the diameter of

a single dispersed phase entity and Φ_b is the number flux, this equation is the same as Eq. (2.34) given by

$$\frac{d\dot{m}}{dz} = -\Phi_b \pi d_b^2 \frac{\beta(C_s - c_i)}{(\bar{u} + u_b)} \quad (2.54)$$

where

$$\dot{m} = \frac{\pi}{6} d_b^3 \Phi_b \rho_b \quad (2.55)$$

2.3.2. Outer Plume Equations

1. Conservation of Mass Flux:

The conservation of mass equation for the outer plume is similarly obtained by equating the rate of change of mass flux with height to the mass flux of the entrained and detrained mass fluxes to and from the outer plume (Asaeda & Imberger 1993). Unlike in the inner plume, here we have entrainment from the static ambient fluid as well. a is the outer plume radius.

$$\frac{d}{dz} (\pi (a^2 - b^2) \bar{v}) = -2\pi b \alpha_1 (\bar{u} - \bar{v}) - 2\pi b \alpha_2 \bar{v} - 2\pi a \alpha_3 \bar{v} \quad (2.56)$$

The negative sign on the R.H.S of Eq. (2.56) takes into account that the volume flux is kept positive. This is because the sign of \bar{v} is negative owing to the *descending* outer plume.

2. Conservation of Momentum Flux:

In case of the outer plume, the terms needed to be considered are the entrained momentum flux to the outer plume with the inner plume velocity \bar{u} , the detrained momentum flux from the outer to the inner plume with the outer plume velocity \bar{v} and the buoyant force of the outer plume fluid (Asaeda & Imberger 1993). There is no momentum of the volume of fluid entrained from

the ambient as the ambient fluid is assumed to have zero vertical momentum.

$$\frac{d}{dz} (\pi(a^2 - b^2)\bar{v}^2) = \frac{1}{\gamma} [\pi(a^2 - b^2)\lambda_2^2 g_{wo}' - 2\pi b\alpha_1(\bar{u} - \bar{v})\bar{v} - 2\pi b\alpha_2\bar{v}\bar{u}] \quad (2.57)$$

3. Conservation of Buoyancy Flux:

The conservation of buoyancy flux of the continuous phase for the outer plume is similar to that for the inner plume with a reversal of sign and replacement of \bar{u} with \bar{v} at appropriate places.

$$\frac{d}{dz} (\pi(a^2 - b^2)\bar{v}g'_w) = \pi(a^2 - b^2)\bar{v}N^2 + 2\pi b\alpha_1(\bar{u} - \bar{v})g'_{wo} + 2\pi b\alpha_2\bar{v}g'_{wi} \quad (2.58)$$

4. Conservation of Temperature Flux:

The change in temperature flux of the outer plume is due to the entrainment and detrainment to and from the outer plume, and the corresponding conservation equation is given as follows:

$$\frac{d}{dz} (\pi(a^2 - b^2)\bar{v}T_o) = -2\pi b\alpha_1(\bar{u} - \bar{v})T_o - 2\pi b\alpha_2\bar{v}T_i - 2\pi a\alpha_3\bar{v}T_a \quad (2.59)$$

where T_a is the temperature of the ambient fluid.

5. Conservation of Concentration Flux:

The change in concentration flux of the outer plume is due to the entrainment and detrainment to and from the outer plume, and the corresponding conservation equation is given as follows:

$$\frac{d}{dz} (\pi(a^2 - b^2)\bar{v}c_o) = -2\pi b\alpha_1(\bar{u} - \bar{v})c_o - 2\pi b\alpha_2\bar{v}c_i - 2\pi a\alpha_3\bar{v}c_a \quad (2.60)$$

where c_a is the concentration of the dissolved dispersed phase in the ambient fluid.

6. Conservation of Salinity Flux:

The change in salinity flux of the outer plume is due to the entrainment and detrainment to and from the outer plume, and the corresponding conservation equation is given as follows:

$$\frac{d}{dz}(\pi(a^2 - b^2)\bar{v}s_o) = -2\pi b\alpha_1(\bar{u} - \bar{v})s_o - 2\pi b\alpha_2\bar{v}s_i - 2\pi a\alpha_3\bar{v}s_a \quad (2.61)$$

where s_a is the salinity of the ambient fluid.

3. Summary of Equations

3.1. State Variables

To solve the system of coupled equations for the inner and outer plume, it is necessary to define the terms inside the derivative in the L.H.S as a single variable and then write the equations in terms of these variables. Since all of these terms denote some kind of flux, the variables are called the flux variables. Also, since these variables form the state space vector, they are also known as state variables.

State variables for the inner plume:

$$\begin{aligned}
Q_i &= \pi b^2 \bar{u} \\
J_i &= \pi b^2 \bar{u}^2 \\
F_i &= \frac{\Delta \rho_{wi}}{\rho_r} g \pi b^2 \bar{u} \\
F_b &= \frac{\Delta \rho_b}{\rho_r} g \pi b^2 (\bar{u} + u_s) \bar{c} \\
H_i &= \pi b^2 \bar{u} T_i \\
C_i &= \pi b^2 \bar{u} c_i \\
S_i &= \pi b^2 \bar{u} s_i \\
W_b &= \dot{m} = \frac{\pi}{6} d_b^3 \Phi_b \rho_b
\end{aligned} \tag{2.62}$$

State variables for the outer plume:

$$\begin{aligned}
Q_o &= \pi b^2 \bar{u} \\
J_o &= \pi b^2 \bar{u}^2 \\
F_o &= \pi b^2 \bar{u} \frac{\Delta \rho_{wi}}{\rho_r} g \\
H_o &= \pi b^2 \bar{u} T_o \\
C_o &= \pi b^2 \bar{u} c_o \\
S_o &= \pi b^2 \bar{u} s_o
\end{aligned} \tag{2.63}$$

3.2. Primary Variables

Inner Plume:

$$\begin{aligned}
\bar{u} &= \frac{J_i}{Q_i} \\
b &= \frac{Q_i}{\sqrt{\pi J_i}} \\
T_i &= \frac{H_i}{Q_i} \\
c_i &= \frac{C_i}{Q_i} \\
s_i &= \frac{S_i}{Q_i} \\
d_e &= \left(\frac{6W_b}{\pi \Phi_b \rho_b} \right)^{1/3}
\end{aligned} \tag{2.64}$$

Outer Plume:

$$\begin{aligned}
\bar{v} &= \frac{J_o}{Q_o} \\
a &= \left(\frac{Q_i^2}{\pi J_i} + \frac{Q_o^2}{\pi J_o} \right)^{1/2} \\
T_o &= \frac{H_o}{Q_o} \\
c_o &= \frac{C_o}{Q_o} \\
s_o &= \frac{S_o}{Q_o}
\end{aligned} \tag{2.65}$$

3.3. Two-fluid Model Equations

Inner Plume:

$$\frac{dQ_i}{dz} = 2\sqrt{\pi} \frac{Q_i}{\sqrt{J_i}} \left[\alpha_1 \left(\frac{J_i}{Q_i} - \frac{J_o}{Q_o} \right) + \alpha_2 \frac{J_o}{Q_o} \right] \quad (2.66)$$

$$\begin{aligned} \frac{dJ_i}{dz} = \frac{1}{\gamma} \left[\frac{F_b}{\left(\frac{J_i}{Q_i} + u_b \right)} + \lambda_2^2 \frac{F_i Q_i}{J_i} \right. \\ \left. + 2\sqrt{\pi} \frac{Q_i}{\sqrt{J_i}} \left(\alpha_1 \left(\frac{J_i}{Q_i} - \frac{J_o}{Q_o} \right) \frac{J_o}{Q_o} + \alpha_2 \frac{J_o J_i}{Q_o Q_i} \right) \right] \end{aligned} \quad (2.67)$$

$$\frac{dF_i}{dz} = -Q_i N^2 - 2\sqrt{\pi} \frac{Q_i}{\sqrt{J_i}} \left(\alpha_1 \left(\frac{J_i}{Q_i} - \frac{J_o}{Q_o} \right) \frac{F_o}{Q_o} - \alpha_2 \frac{J_o F_i}{Q_o Q_i} \right) \quad (2.68)$$

$$\frac{dH_i}{dz} = 2\sqrt{\pi} \frac{Q_i}{\sqrt{J_i}} \left[\alpha_1 \left(\frac{J_i}{Q_i} - \frac{J_o}{Q_o} \right) \frac{H_o}{Q_o} + \alpha_2 \frac{J_o H_i}{Q_o Q_i} \right] + \frac{\Delta H_{sol}}{\rho_w C_p} \quad (2.69)$$

$$\frac{dC_i}{dz} = 2\sqrt{\pi} \frac{Q_i}{\sqrt{J_i}} \left[\alpha_1 \left(\frac{J_i}{Q_i} - \frac{J_o}{Q_o} \right) \frac{C_o}{Q_o} + \alpha_2 \frac{J_o C_i}{Q_o Q_i} \right] + \frac{4\pi \frac{Q_i^2}{\pi J_i} N_b}{\left(\frac{J_i}{Q_i} + u_b \right)} \beta \left(C_s - \frac{C_i}{Q_i} \right) \quad (2.70)$$

$$\frac{dS_i}{dz} = 2\sqrt{\pi} \frac{Q_i}{\sqrt{J_i}} \left[\alpha_1 \left(\frac{J_i}{Q_i} - \frac{J_o}{Q_o} \right) \frac{S_o}{Q_o} + \alpha_2 \frac{J_o S_i}{Q_o Q_i} \right] \quad (2.71)$$

$$\frac{dW_b}{dz} = -(\pi \Phi_b)^{1/3} \left(\frac{6W_b}{\rho_b} \right)^{2/3} \left[\frac{\beta \left(C_s - \frac{C_i}{Q_i} \right)}{\left(\frac{J_i}{Q_i} + u_b \right)} \right] \quad (2.72)$$

Outer Plume:

$$\begin{aligned} \frac{dQ_o}{dz} = & -2\sqrt{\pi} \frac{Q_i}{\sqrt{J_i}} \left[\alpha_1 \left(\frac{J_i}{Q_i} - \frac{J_o}{Q_o} \right) + \alpha_2 \frac{J_o}{Q_o} \right] \\ & - 2\sqrt{\pi} \alpha_3 \left(\frac{Q_o^2}{J_o} + \frac{Q_i^2}{J_i} \right)^{1/2} \frac{J_o}{Q_o} \end{aligned} \quad (2.73)$$

$$\frac{dJ_o}{dz} = \frac{1}{\gamma} \left[-\lambda_2^2 \frac{F_o Q_o}{J_o} - 2\sqrt{\pi} \frac{Q_i}{\sqrt{J_i}} \left(\alpha_1 \left(\frac{J_i}{Q_i} - \frac{J_o}{Q_o} \right) \frac{J_o}{Q_o} + \alpha_2 \frac{J_o}{Q_o} \frac{J_i}{Q_i} \right) \right] \quad (2.74)$$

$$\frac{dF_o}{dz} = Q_o N^2 - 2\sqrt{\pi} \frac{Q_i}{\sqrt{J_i}} \left[\alpha_1 \left(\frac{J_i}{Q_i} - \frac{J_o}{Q_o} \right) \frac{F_o}{Q_o} + \alpha_2 \frac{J_o}{Q_o} \frac{F_i}{Q_i} \right] \quad (2.75)$$

$$\begin{aligned} \frac{dH_o}{dz} = & -2\sqrt{\pi} \frac{Q_i}{\sqrt{J_i}} \left[\alpha_1 \left(\frac{J_i}{Q_i} - \frac{J_o}{Q_o} \right) \frac{H_o}{Q_o} + \alpha_2 \frac{J_o}{Q_o} \frac{H_i}{Q_i} \right] \\ & - 2\sqrt{\pi} \alpha_3 \left(\frac{Q_o^2}{J_o} + \frac{Q_i^2}{J_i} \right)^{1/2} \frac{J_o}{Q_o} T_a \end{aligned} \quad (2.76)$$

$$\begin{aligned} \frac{dC_o}{dz} = & -2\sqrt{\pi} \frac{Q_i}{\sqrt{J_i}} \left[\alpha_1 \left(\frac{J_i}{Q_i} - \frac{J_o}{Q_o} \right) \frac{C_o}{Q_o} + \alpha_2 \frac{J_o}{Q_o} \frac{C_i}{Q_i} \right] \\ & - 2\sqrt{\pi} \alpha_3 \left(\frac{Q_o^2}{J_o} + \frac{Q_i^2}{J_i} \right)^{1/2} \frac{J_o}{Q_o} c_a \end{aligned} \quad (2.77)$$

$$\begin{aligned} \frac{dS_o}{dz} = & -2\sqrt{\pi} \frac{Q_i}{\sqrt{J_i}} \left[\alpha_1 \left(\frac{J_i}{Q_i} - \frac{J_o}{Q_o} \right) \frac{S_o}{Q_o} + \alpha_2 \frac{J_o}{Q_o} \frac{S_i}{Q_i} \right] \\ & - 2\sqrt{\pi} \alpha_3 \left(\frac{Q_o^2}{J_o} + \frac{Q_i^2}{J_i} \right)^{1/2} \frac{J_o}{Q_o} s_a \end{aligned} \quad (2.78)$$

3.4. Mixed-fluid Model Equations

The model equations for the mixed-fluid model differ from the two-fluid model in the following aspects:

1. Conservation of Momentum flux equation for the inner plume
2. Conservation of Buoyancy flux equation for the inner plume
3. Conservation of Buoyancy flux equation for the outer plume

Also, in case of the mixed-fluid model, there are no separate equations for the buoyancy fluxes for the dispersed and continuous phases. Instead one single equation exists for the buoyancy flux of the mixture phase. All other equations are identical to that of the two-fluid model shown in the earlier subsection.

The conservation equations for the mixed-fluid model that are different from those of the two-fluid model are summarised below.

Inner Plume:

$$\frac{dJ_i}{dz} = \frac{1}{\gamma} \left[\lambda^2 \frac{F_i Q_i}{J_i} + 2\sqrt{\pi} \frac{Q_i}{\sqrt{J_i}} \left(\alpha_1 \left(\frac{J_i}{Q_i} - \frac{J_o}{Q_o} \right) \frac{J_o}{Q_o} + \alpha_2 \frac{J_o J_i}{Q_o Q_i} \right) \right] \quad (2.79)$$

$$\begin{aligned} \frac{dF_i}{dz} = & -Q_i N^2 - 2\sqrt{\pi} \frac{Q_i}{\sqrt{J_i}} \left[\alpha_1 \left(\frac{J_i}{Q_i} - \frac{J_o}{Q_o} \right) \frac{F_o}{Q_o} - \alpha_2 \frac{J_o}{Q_o} \left(\frac{F_i}{Q_i} - g\bar{c} \right) \right] + \\ & \frac{gQ_b H_T}{u_b(H_T - z)} \left(\frac{J_i}{Q_i(H_T - z)} + \frac{1}{Q_i} \frac{dJ_i}{dz} - \frac{J_i}{Q_i^2} \frac{dQ_i}{dz} \right) \end{aligned} \quad (2.80)$$

Outer Plume:

$$\frac{dF_o}{dz} = Q_o N^2 - 2\sqrt{\pi} \frac{Q_i}{\sqrt{J_i}} \left[\alpha_1 \left(\frac{J_i}{Q_i} - \frac{J_o}{Q_o} \right) \frac{F_o}{Q_o} + \alpha_2 \frac{J_o}{Q_o} \left(\frac{F_i}{Q_i} - g\bar{c} \right) \right] \quad (2.81)$$

Qualitatively, the difference between the mixed-fluid and the two-fluid models lie in

three major aspects. The first difference is in the equation for momentum flux. In the mixed-fluid model, buoyant forces are calculated for a mixture phase, while in the two-fluid model they are calculated separately for the dispersed and the continuous phases. Secondly, in the expression for the buoyancy flux of the mixture phase in the mixed fluid model, the transport of buoyancy is assumed to occur at the transport velocity of the continuous phase, which however is not true due to the existence of the dispersed phase slip velocity. Finally, the entrained buoyancy to the outer plume in case of a mixed fluid model involves the use of the void fraction by which the dispersed phase entrainment has to be subtracted from the mixture phase in the inner plume, as seen in Eq. (2.80) and Eq. (2.81). This adjustment in the entrainment terms is not required in the two-fluid model because the phases are already accounted for separately in the formulation.

CHAPTER III

MODEL PARAMETERS

The model equations derived and summarised in Chapter II have several parameters related to the phase and ambient physical and chemical properties that need correct quantification so that the models yield realistic results. This chapter is devoted to the explanation of each of the parameters and how they are derived using the relevant physical or empirical relations.

1. Phase Properties

As has been described in Chapter I, the present work is based on three case studies which basically involves the study of the physics of multiphase plumes of air-bubbles or CO₂ droplets in water. So the dispersed phases whose properties need to be determined are air and carbon dioxide and the continuous phase is water. The exact value or the approximate ranges of values of these parameters and of the phase properties will be discussed here for each of the three case studies which are as follows:

Case 1: Lake Destratification

Case 2: Lake Aeration

Case 3: CO₂ Sequestration

1.1. Density

The ideal gas equation of state for air shows significant deviation in the density from measured values at low temperatures and high pressures when it can no longer be assumed incompressible. Lemmon, Jacobsen, Penoncello & Friend (2000) developed the equation of state using experimental data for pressure-density-temperature (p, ρ, T), isochoric heat capacity, speed of sound, and second virial coefficients. The equa-

tion was based upon the calculation of the compressibility by calculating the residual Helmholtz energy contribution to the equation of state detailed in Appendix A. This formulation was found to be valid for liquid, vapor and supercritical air temperatures from 60 K to 2000 K and pressures up to 2000 MPa. In the absence of reliable experimental data for air above 873 K and 70 MPa, air properties were predicted from nitrogen data in this region. The expression for the compressibility is given as

$$Z = \frac{p}{\rho RT} \quad (3.1)$$

and also

$$Z = 1 + \delta \left(\frac{\partial \alpha_r}{\partial \delta} \right)_\tau \quad (3.2)$$

where δ is the reduced density, τ is the reduced temperature and α_r is the residual of the Helmholtz energy given in (Lemmon et al. 2000). The derivation is shown in Appendix A.

For the present case studies, the temperature and pressure would most likely vary between 273 K - 323 K and 0.1 - 1.0 MPa respectively and therefore this equation of state can be applied to calculate the density of air at the *insitu* temperature, salinity and pressure. The method applied to calculate the density is a standard root-finding method that starts with an initial guessed value of the density ρ and then iterates until the difference in the computed values of Z using Eq. (3.1) and Eq. (3.2) lies within an acceptable tolerance, typically 1 percent.

The density of CO₂ is computed using the IUPAC Equation of State (Angus, Armstrong & Reuck 1976). The method of computation is also similar to that of the equation of state for air. For given values of temperature, salinity and pressure, the compressibility of the CO₂ phase is computed for a guessed value of the CO₂ density and compared with the actual value until the residual for the compressibility vanishes

or lies within an acceptable tolerance. The analytic equation of state is detailed in the appendix. This equation is not accurate near the critical point for CO₂ which is located at 304.2 K and 73.86 bars. The present case has temperatures in the range of 273 - 323 K and pressure in the range 0.1 - 80 Mpa but the critical point is never encountered, so the equation is applicable.

The dispersed phase density values for the different cases are now listed below.

Cases 1 and 2: In these two cases, the temperature will vary with depth in the range of 5°C to 20°C. The salinity will vary between 35 and 30 psu at the corresponding depths. The depth of consideration is 50m to 0. In these design limits, the air equation of state gives the density of air-bubbles to vary from 7.60 kg/m³ at the bottom of the lake to about 1.20 kg/m³ at the top. This signifies that there is a significant amount of bubble expansion.

Case 3 In this case the temperature will vary with depth in the range of 5°C to 10°C. The salinity will correspondingly vary between 40 and 35 psu. The depth of consideration is 800m to 600m. In these design limits, the CO₂ equation of state gives the density of liquid CO₂ droplets to vary from 935 kg/m³ at a depth of 800 m to about 900 kg/m³ at a depth of 600 m. The CO₂ droplets are expected to dissolve completely by then; if not, the upper bound of the depth has to be relaxed to a lower value until all of the droplets dissolve. It is important to note here that the phase of CO₂ is a function of the temperature, salinity and pressure as well. So if the liquid CO₂ does not dissolve completely within a specific range of depth which is about 450m, it would translate itself to the vapor phase after which it would escape into the atmosphere in case of incomplete dissolution. Therefore, the tracking of the density as a function of the temperature, salinity and pressure data is important as it will help assess the feasibility study of the CO₂ sequestration project at the design depth of release at the design flowrate.

The density of the continuous phase(water) is calculated using the UNESCO Seawater equation of state (Gill 1982) which is given in Appendix A. This equation calculates the density of water as a function of temperature, salinity and pressure.

1.2. Viscosity

Viscosity has been found to be a weak function of pressure but is strongly dependent on the temperature. From standard thermodynamic tables, the viscosity of air at 0°C and 30°C are found to be 1.729×10^{-5} kg/m/s and 1.872×10^{-5} kg/m/s respectively. The intermediate values are obtained by interpolation. The viscosity of liquid CO₂ remains fairly constant in the temperature of consideration and the value of 0.14 centipoise or 1.4×10^{-4} kg/m/s has been used in the calculations.

The viscosity of water μ in kg/m/s is calculated by the equation (Lund 1995)

$$\mu = (2.6 \times 10^{-6}) e^{\frac{1750}{T}} \quad (3.3)$$

where T is the temperature in degree K.

1.3. Surface Tension

The surface tension of water provides the necessary wall tension for the formation of bubbles with water. The tendency to minimise that wall tension pulls the bubbles into spherical shapes. The surface tension σ can be calculated from a knowledge of the pressure difference ΔP between the inside and outside of a bubble and the radius r of the bubble and is given by

$$\Delta P = \frac{2\sigma}{r} \quad (3.4)$$

The surface tension of water is nearly constant over the range of interest and is taken to be 7.1×10^{-2} N/m.

1.4. Mass Transfer Coefficient

Motarjemi & Jameson (1978) measured the mass transfer coefficient β_O for oxygen in tap water and based on their data, β_O increases linearly up to 4×10^{-4} m/s for bubble radius up to about 0.8 mm and afterwards stays fairly constant at this value. In the present work, β , the mass transfer coefficient for air has been taken to be equal to that of oxygen β_O .

For CO₂ droplets, the mass transfer coefficient is found to reduce significantly with the formation of a clathrate hydrate film which has been observed by many researchers (Hirai et al. 1996, Warzinski & Holder 1999). Hirai et al. (1996) found that the dissolution rate of a hydrate covered droplet at 278 K, which is a typical ambient temperature at 800 m, was about half that of a droplet with no hydrate formation at 286 K. Warzinski & Holder (1999) found that the dissolution rate for a hydrate shell at 275 K was three orders of magnitude lower than a droplet without a hydrate shell at 281 K. However an exact quantification of the value of the mass transfer coefficient for CO₂ droplets is still rather uncertain and therefore the value of 1.5×10^{-4} m/s corresponding to a droplet without a hydrate shell is used in this present work. Also a sensitivity analysis is performed with values of β made equal to this value, half and one-tenth of this value.

1.5. Solubility

The solubility constant K of molecular nitrogen and oxygen were measured at specific points of temperature ranging between 0 and 30°C by Marshall (1976). Wüest et al. (1992) used second order polynomial fits to Marshall's data to get the solubility values for the respective gases. In the present work which deals with atmospheric air which is roughly a mixture of nitrogen and oxygen in the proportion of 4:1, the solubility

constant of air is computed by taking a weighted average of the polynomial fits of Wüest et al. (1992) given by the equation

$$K_{air} = \frac{(4K_{N_2} + K_{O_2})}{5} \quad (3.5)$$

Based on the above equation, the solubility constant K for air is found to vary from a value of 1.28 mol/m³/bar at 0°C to 0.72 mol/m³/bar at 30°C. The intermediate values of solubility for each specific case study can be obtained using a cubic spline interpolation algorithm. Hence the solubility C_s in kg/m³ is given as

$$C_s = Kp \quad (3.6)$$

where p is the ambient pressure in bars.

Cases 1 and 2: Using the molecular weight of air which is equal to 28.8 g/mol, the value of C_s at a depth of 50m (pressure of nearly 6 bars) and 5°C is about 0.2 kg/m³ and the value near the water surface at a temperature of 30°C is about 0.02 kg/m³, that is the solubility reduces by nearly 10 times as the bubbles reach the water surface.

Case 3: The solubility of CO₂ in seawater, expressed as a mole fraction x can be obtained from an empirical relationship derived by Teng & Yamasaki (1998) based on the modification of Henry's Law using the Setchenow equation which is given by

$$x_{CO_2} = \frac{f_{CO_2}}{K_H} e^{\alpha S} \quad (3.7)$$

where f_{CO_2} is the fugacity of CO₂ which can be calculated using the CO₂ equation of state detailed in Appendix A, K_H is the Henry's Law coefficient for the CO₂-seawater system, α represents a salting-out coefficient, and S is the seawater salinity in psu. Teng & Yamasaki (1998) found empirical values for K_H and α as a function

of temperature and pressure as follows:

$$\begin{aligned}
 K_H &= a + bP + cP^2, \\
 a &= 5.20 \times 10^3 - 3.92 \times 10^1 T + 7.5 \times 10^{-2} T^2, \\
 b &= -1.03 \times 10^2 + 7.08 \times 10^{-1} T - 1.20 \times 10^{-3} T^2, \\
 c &= 2.2 \times 10^{-2}
 \end{aligned} \tag{3.8}$$

and

$$\alpha = 5.43 \times 10^{-1} - 3.54 \times 10^{-3} T + 5.69 \times 10^{-6} T^2 \tag{3.9}$$

where K_h and P has units of MPa and T has units of K.

The solubility C_s in kg/m³ can be computed from the mole fraction x of CO₂ (moles of CO₂ in 1 mole of water) from the knowlede of the molecular weight of sea-water M_{H_2O} (= 19.7) and that of CO₂ (= 44.01) as follows:

$$C_s = x_{CO_2} \frac{M_{CO_2}}{M_{H_2O}} \cdot 1000 \tag{3.10}$$

where 1000 is a conversion factor.

1.6. Solute Density Effect

The dissolution of CO₂ into sea-water increases the density of sea-water. This phenomenon is called the solute density effect. The solute density effect is a critical factor affecting the behavior of a CO₂ droplet plume which postulates an increase in the seawater density by $\delta\rho$ due to the dissolved CO₂, given by

$$\delta\rho = (1 - \bar{V}\rho_{ref}) [CO_2] \tag{3.11}$$

where \bar{V} is the specific volume [m^3/kg], ρ_{ref} is a reference density usually taken as 1000 kg/m^3 and $[\text{CO}_2]$ is the concentration of the dissolved CO_2 in kg/m^3 . \bar{V} was calculated to have the value of $7.05 \times 10^{-4} \text{ m}^3/\text{kg}$ from experimental density measurements taken at 276 K and 343 atm, with CO_2 concentrations ranging from 4.4 to 15.4 kg/m^3 (Ohsumi, Nakashiki, Shitashima & HIRAMA 1992). It has been found that the water is cooled as the CO_2 dissolves, that is, the reaction is endothermic.

After calculating the density of the continuous phase from the equation of state from the values of temperature, pressure and salinity at each step, $\delta\rho$ should be added to get the correct density of seawater to calculate the buoyancy fluxes and other parameters in the model.

The solute density effect in case of air-bubbles dissolving in water is negligible.

1.7. Heat of Dissolution

The heat of dissolution is the heat released or absorbed due to dissolution. For dissolution of air in water this is negligible but for CO_2 droplets it is quite significant having a value of $\Delta H_{sol} = 25 \text{ kJ/mol} = 568 \text{ kJ/kg}$ (Lund 1995). A positive sign denotes heat is absorbed by the reaction from the system.

1.8. Specific Heat

The specific heat of water is required in the model equation for temperature flux. Its value is a function of temperature which can be obtained from standard thermodynamic tables. The value is found to vary nonlinearly with temperature from 4217 kJ/kmol/K at 0°C to 4178 kJ/kmol/K at 30°C . The intermediate values are obtained by interpolation.

1.9. Compressibility

The compressibility or Z -factor is the parameter incorporated in the models to take into account of the fact that deviations from the ideal gas law $P = \rho RT$ results due to compressibility effects. The modified equation for the ideal gas law due to the compressibility effect is

$$P = Z\rho RT \quad (3.12)$$

where Z is the compressibility. $Z = 1$ for an ideal gas.

Cases 1 and 2: The compressibility of air bubbles at a depth of 50 m where the ambient temperature and salinity are expected to be 5°C and 35 psu respectively is 0.9969 which increases to a value of 0.9997 at the free surface where the base case ambient temperature is 25°C and ambient salinity is 35 psu. Since the change is less than 1 percent, the compressibility effects for air-bubbles for these two case studies can be neglected.

Case 3: The compressibility of CO₂ droplets at a depth of 800 m where the ambient temperature is 5°C and ambient salinity is 35 psu is found to be 0.16 and this reduces to a value of 0.12 at a depth of 600 m with ambient temperature and salinity of 10°C and 35 psu respectively. In this case the reduction in the compressibility is about 25 percent which is quite significant.

2. Ambient Properties

2.1. Temperature

The vertical ambient temperature profile in lakes, oceans and other water bodies on earth are seen to follow a general pattern. The temperature at the surface is higher than at the bottom due to the solar heat. The temperature at the bottom is close to

4°C at which water attains its highest density. In these two regions the temperature remains fairly constant and in between there is a region of sharp thermal gradient which is known as the *thermocline*.

In the present work, the temperature data for the lake has been obtained from Nepf (1995) and for the ocean it is taken from Teng, Masutani, Kinoshita & Nihous (1996). These are shown in detail in Chapter VII.

2.2. Salinity

The pattern of the salinity is similar to that of the temperature profile except for the fact that the variation is in the reverse order, that is more saline water is at the bottom than at the top due to its heavier density.

The salinity data for the lake has been obtained from Nepf (1995) and for the ocean it is taken from Teng et al. (1996). These are also shown in Chapter VII.

2.3. Dissolved Insitu Concentration

Wüest et al. (1992) measured the ambient dissolved insitu concentration of nitrogen in Lake Baldeggersee in Switzerland to be equal to 0.02 kg/m³ and found it to remain fairly constant over the depth of the lake equal to 70 m. In the present work, ambient dissolved insitu concentration of air is also kept constant at this value for Cases 1 and 2.

The pH of pure water is equal to 7. However due to the presence of dissolved CO₂ and other inorganic salts in water it is slightly basic in nature and the measured pH of seawater has been found to be about 7.8 which corresponds to a dissolved insitu concentration of 0.01 kg/m³ (Crouse 2000). This value of ambient dissolved insitu concentration for CO₂ has been used for Case 3 of this present work.

2.4. Entrainment Coefficient

The entrainment coefficient has a value of 0.116 for single phase plumes with a Top-Hat velocity profile. This value has been found from experiments to remain fairly constant with depth for single-phase plumes as a consequence of the self-similarity of the flow. However deviations from the self-similar behavior occur in the case of stratified flows and also in unstratified flows in the case of multiphase plumes, when the entrainment coefficient may no longer remain constant with depth. Bergmann et al. (2004) found a variation of the entrainment coefficient with depth experimentally in case of an unstratified ambient which is given as:

$$\alpha(z) = 0.0004 \left(\frac{z}{H_T} \right) + 0.0459 \quad (3.13)$$

where H_T is the total pressure head at the diffuser level. This formulation is based on Gaussian profiles and was obtained using PIV measurements of velocity of air-bubbles released in water in a 40 cm x 40 cm x 70 cm experimental tank from a depth of 9 cm to 60 cm above the diffuser source. The mixed-fluid and two-fluid models are compared against each other using this formulation of α over this depth, which is detailed in Chapter VI. The question that remains unanswered is whether Eq. (3.13) can be used to extrapolate the values beyond 60 cm. The depth-averaged value of α for the Top-Hat version was found to be 0.087 (the corresponding value for Gaussian profiles is 0.062) which will be used in the present work to simulate the three case studies. Milgram (1983) observed α to span the range of 0.037 to 0.165 for Gaussian profiles and he justified the phenomenon by arguing that this was due to an increase in the bubble Froude number that enhances turbulent entrainment near the entrainment interface.

2.5. Momentum Amplification Factor

The momentum amplification factor γ takes into account the added momentum flux due to turbulence generated by the dispersed phase above that of the mean flow (Milgram 1983). It has a value of 1.07 for single-phase plumes and has a higher value for multiphase plumes and increases for decreasing air-flow rate (Baines & Leitch 1992). Crouse (2000) varied the value of γ from 1.0 to 2.0 to explore its sensitivity and found that his model was quite insensitive to this parameter. In the present work, a constant value of $\gamma = 1.2$ has been chosen as verified from laboratory experiment (Bergmann et al. 2004) detailed in Chapter VI.

3. Design Variables

3.1. Flow Rate

Air-flow rates from as low as 0.024 l/min (Baines & Leitch 1992) to as high as 660 l/s (Topham 1975) have been used in bubble plume experiments and applications. For lake aeration and destratification, Wüest et al. (1992) used diffuser units with an air input of 5-15 l/s per unit for the purpose of artificial mixing of the Swiss lake Baldeggersee. Crouse (2000) took the diffuser air flow rate to be equal to 20 l/s for his base case. In the present work, for cases 1 and 2, diffuser air-flow rates of 3, 6 and 9 l/s have been considered. For Case 1, the optimal air-flow rate suitable for destratification of the lake will be determined.

The release rate of the CO₂ droplets was proposed to be 1 kg/s which corresponds to a volume flow rate of 1.1 l/s at a depth of 800m in the ocean for the International Field Experiment intended for CO₂ sequestration (Crouse 2000). For Case 3 of this present work, this value of the initial flow rate of the CO₂ droplets is used.

3.2. Diffuser Dimensions

The important parameters of the diffuser geometry that are involved in the model equations are the diffuser diameter and the orifice diameter which essentially is the initial diameter of the released dispersed phase. The diffuser diameter is used to compute the location of the virtual point source below the diffuser level (Ditmars & Cederwall 1974) and the initial plume width (Wüest et al. 1992) for the purpose of computing the initial conditions, detailed in Chapter V. The system *Tanytarsus* (Wüest et al. 1992) which has a diameter of 7 m is used to destratify a typical lake of 60 to 70 m water depth. This value of the diffuser diameter will be used in this present work for Cases 1 and 2. For Case 3, a diffuser source having a diameter of 1 m has been considered.

The orifice diameter controls the initial size of the dispersed phase dimensions. The diameter of air-bubbles droplets should be small enough for aeration so that they dissolve before escaping into the atmosphere. For destratification, they should be big enough so that the plume is able to overcome the stratification. The size of the CO₂ droplets should be small enough so that all of them dissolves before the phase changes from liquid to gaseous. The airflow rate also determines the initial size of the released dispersed phase. Larger air-flow rates produce larger bubbles and vice versa. It also depends on the ambient properties. Socolofsky et al. (2002) found from their experiments that the same diffuser unit that produces 2 mm diameter bubbles in fresh water produces 0.5 mm diameter bubbles in sea water.

Wüest et al. (1992) found from their lake model that the initial bubble diameters of 2 and 12 mm respectively in summer (July) and winter (November) were enough to dissolve all the bubbles. Since the lake temperature data used in this present work (Nepf 1995) corresponds to summer (August), therefore the orifice diameter is

chosen as 2 mm and 1 mm in two successive runs of the models for Case 2. For Case 1, the orifice diameter is kept fixed at 10 mm and for this value of the diffuser orifice diameter, comparisons are made between the optimal air flowrate necessary for destratification as predicted by the two models. The orifice diameter for case 3 is kept the same as the base case of Crouse (2000) which is equal to 5 mm.

3.3. Number Flux of Dispersed Phase

The number flux Φ_b of the dispersed phase is assumed to remain constant with depth, which means the model assumes no coalescence of the dispersed phase and that they have a uniform rate of shrinkage due to dissolution. Φ_b is calculated using the equation

$$\Phi_b = \frac{6Q_b}{\pi d_b^3} \quad (3.14)$$

rounded to the nearest integer. For cases 1 and 2 of this present work, $\phi_b = O \sim (10^4)$ and for case 3, $\phi_b = O \sim (10^3)$.

3.4. Spreading Ratio

The model uses two spreading ratios λ_1 and λ_2 which are defined as the ratio of the width of bubble core to that of the velocity profile and the ratio of width of the relative density profile of the continuous phase to that of the velocity profile respectively. The value of λ_1 has been observed to range between 0.3 and 1.0 by researchers (Ditmars & Cederwall 1974, Milgram 1983). The values on the lower side are taken when there is significant plume wandering. Wüest et al. (1992) used the constant value of 0.8 in their model. A sensitivity analysis performed in Chapter VI shows that the model results are quite insensitive to the value of λ_1 . Crouse (2000) took the value to be 1.0 arguing that the inner plume is bound to shrink up to the bubble core interface due to the descending outer plume. In the present work, $\lambda_1 = 0.8$ is taken for all

the cases. The value of λ_2 is found to be close to or slightly greater than 1. For the present work, $\lambda_2 = 1.0$ has been taken.

CHAPTER IV

MODEL ALGORITHM AND GRAPHICAL USER INTERFACE

In this chapter, the algorithm for the numerical model is described. The mixed-fluid and two-fluid models work along the same algorithm, the only difference being in the equations to be solved. The algorithm used in this present work is the one proposed by Socolofsky et al. (2002). The numerical scheme used is the well-known 4th order Runge-Kutta method. Crouse (2000) used a slightly different version of the same algorithm to run his two-fluid model. He integrated all the inner plumes at a time and then the outer plumes, whereas, the algorithm used in the present work integrates every peel in succession consisting of an inner and an outer plume at a time. This is described in detail in the following section.

1. Model Algorithm

The way the present algorithm works is that at first since only the inner plume exists, the model solves only the single plume equations until the first peel occurs which happens when the momentum flux of the continuous phase becomes non-positive, or when the water surface is reached. The direction of model computation is then reversed and the outer plume is then integrated downwards until the momentum flux of the outer plume equals zero, or when trapping occurs. During the integration of the outer plume, the inner plume is considered to be present and so, this time the equations that are solved are the double plume equations. Trapping of the outer plume signals the end of that level of iteration. The next level of iteration is then started for the same plume from the same starting point (which for the first plume is the level of the diffuser) and this time the model solves the single plume equations until the beginning of the trap height recorded at the previous level of iteration, but with

the outer plume existing. From then on the model solves the double-plume equations for the inner plume until peeling occurs, after which the outer plume is integrated in the same fashion as before until trapping occurs. Thus a new set of peel and trap heights are recorded. The iterations are continued until the convergence criterion is met. Convergence is reached when the value of the outer plume buoyancy flux between two consecutive iterations at the peel height differ by less than 1 percent. If the convergence criteria is met, the next plume is started from the peel height reached at convergence and the same process is continued until finally the water surface is reached or the dispersed phase dissolves completely (greater than 99%). The Runge-Kutta scheme is implemented in *rk4.m* and the model equations are solved at every level of depth in *derivs.m*.

A computer program has been written in MATLAB 6.5 that has a GUI front end that reads in all of the input data required. Figure 13 depicts the flowchart for the program. First the different inputs and the ambient field data are read into the graphical user interface supplied by the user which are then passed on to the driver function *rk4_driver.m*. This function starts the model computation from the starting point which is the release point of the dispersed phase. It uses the function *derivs.m* to solve for the flux variables in the equations at each successive step using the knowledge of the corresponding values at the previous steps wherever necessary and two other functions *integrator.m* and *rk4.m* to integrate each of the flux variables over each step using the Runge-Kutta scheme. To start the model computation, the first set of values for the flux variables need to be provided as required by this scheme. These initial values govern the model outputs eventually and therefore are very important. The methods used to evaluate them are discussed in detail in the next chapter.

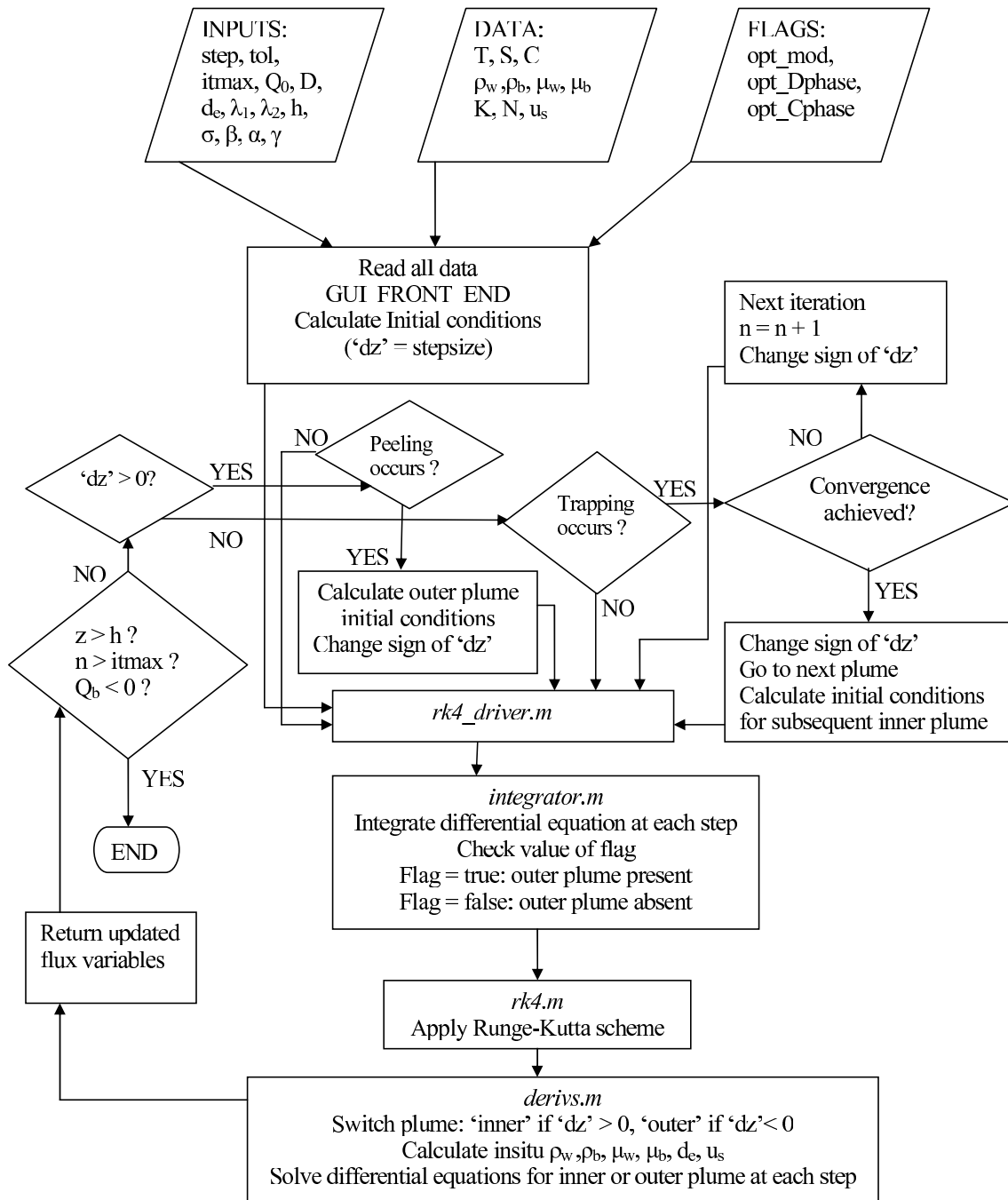


Fig. 13. Flowchart of model algorithm

2. Program Inputs

Reading the values of the model parameters correctly and efficiently is a crucial aspect which needs to be dealt with in an organized manner. This is achieved by identifying which of the parameters are constants and which of them vary with respect to depth. Several of the model parameters are functions of temperature and salinity which are both functions of depth and therefore they are variables with respect to depth. The following section describes how the input data can be handled efficiently.

2.1. Constant Input Data

Constant data refers to the model parameters that remain unchanged with respect to depth. These include the following:

1. *Step size*

This is the stepsize to be specified for running the numerical scheme. The depth over which the equations are integrated for the three different cases is divided into steps that are small enough, so that the applied numerical scheme gives a stable solution. A stepsize of 0.05 m is found to achieve this for all the three case studies. For the lake of depth 50 m, this amounts to 1000 grid points and for the ocean where the integration is carried out from a depth of 800 m to a depth of 600 m, 4000 grid points are generated where the data must be available for all the model parameters. The data which remain constant with depth can be provided all at once but for data varying with depth, calculations need to be done dynamically at every grid point to extract the data corresponding to that particular level of depth.

Crouse (2000) used an adaptive grid in the numerical scheme to capture some of the finer scales that occur during peeling. He introduced a peeling parameter

called ϵ in his model which allows fluid to peel from the plume as needed and with less than 100% efficiency. This allowed his model to simulate Type 3 plumes. However in the present work, the phenomenon of partial peeling is not considered because the primary purpose here is to determine the peel and trap heights and DMPR. Thus, this model can simulate only Type 2 plumes and not Type 3. In producing the model results, the choice of a constant step-size was found to be sufficient therefore, and an adaptive grid was not necessary.

2. *Tolerance*

This is the convergence criterion to be specified in terms of the tolerance which is the relative difference between the calculated values of the outer plume buoyancy flux in two consecutive iterations, expressed in percent. In the present work, it has been set equal to 1%.

3. *Maximum number of iterations*

This denotes the maximum number of iterations the model runs for each plume. It is seen that convergence is achieved in the successful cases in less than 10 iterations. However the maximum value is set at 15 for this model, which if crossed causes the program to terminate with an error message indicating possible oscillations.

4. *Diffuser air flow rate*

This is the value of the diffuser air flow rate to be entered having the units of liters/minute. The values for the different case studies have been discussed in Chapter III.

5. *Diffuser Diameter*

This is the value of the diffuser diameter to be specified in cm.

6. *Diffuser Orifice Diameter*

This is the value of the orifice diameter or the initial diameter of the dispersed phase, to be specified in mm.

7. *lambda_1*

This is the spreading ratio λ_1 of the width of the dispersed phase void fraction profile relative to the width of the continuous phase velocity profile. The value has been discussed in Chapter III.

8. *lambda_2*

This is the spreading ratio λ_2 of the width of the profile for the continuous phase density difference with the ambient relative to the width of the continuous phase velocity profile. The value has been discussed in Chapter III.

9. *Depth of release*

This is the water depth in m equal to the distance below the free surface where the dispersed phase is released.

10. *z_upper*

This is the height above the injection in m up to which the model executes.

11. *z_lower*

This is the height above the diffuser in m from which the model executes. In most cases, the model runs from the diffuser level which is the origin and then this is set equal to zero.

12. *Surface Tension Coefficient*

This is the value of the surface tension σ of the continuous phase to be specified in mN/m.

13. *Mass transfer coefficient*

This is the value of the mass transfer coefficient β to be specified in cm/s.

14. *Entrainment coefficient*

This is the value of the entrainment coefficient α .

15. *Momentum amplification factor*

This is the value of the momentum amplification factor γ .

16. *Entrainment ratio*

This is the value of the ratio κ which is equal to the ration of the entrainment coefficient from inner to outer plume to that from outer to inner plume.

17. *mu_p*

This is the value of the fractional peeling parameter to be specified for the calculation of the outer plume initial conditions and is discussed in detail in Chapter V.

18. *mu_e*

This is the value of the extra entrainment parameter to be specified for the calculation of the outer plume initial conditions and is discussed in detail in Chapter V.

2.2. Data Varying with Depth

The parameters that vary with water depth include the ambient temperature, salinity and dissolved concentration of the dispersed phase (air or CO₂ in the present work). The ambient dissolved *insitu* concentration is taken to be a constant in this present work as mentioned before in the last chapter. Based on the ambient temperature and salinity, the density of the ambient fluid are computed using the equation of state

at each grid point. The stratification frequency N can then be computed over the interval between each two consecutive grid points. A backward difference is used to approximate $\frac{d\rho}{dz}$ when computing N . The value of N for the first grid point is then taken to be the same as that of the second grid point, and this assumption is valid because the stepsize used is sufficiently small so that stratification does not change significantly over one particular step. The values for the phase density, viscosity, slip velocity, solubility and compressibility are computed based on the *insitu* values of the temperature and salinity at the height of consideration. These values are obtained by calling the following functions from *derivs.m*:

1. *air_ ES.m*:

Using the in-built function *fzero* in MATLAB, this function can be used to compute the density and compressibility of air for a given temperature, salinity and pressure using the air equation of state.

2. *co2_ ES.m*:

Using the in-built function *fzero* in MATLAB, this function can be used to compute the density and compressibility of CO₂ for a given temperature, salinity and pressure irrespective of its phase (liquid or gaseous) using the CO₂ equation of state.

3. *seawater_ ES.m*:

Using the in-built function *fzero* in MATLAB, this function can be used to compute the density of seawater for a given temperature, salinity and pressure using the seawater equation of state.

4. *mu_ wf.m*:

This function computes the viscosity of water as a function of temperature. The

analytical relationship was mentioned earlier in Chapter III.

5. *mu_b.m*:

The viscosity of air and liquid CO₂ are obtained as functions of temperature from thermodynamic tables and then least square fit is used to get an analytical relationship describing the variation. The analytical relationship was mentioned earlier in Chapter III.

6. *Kf.m*:

This function computes the solubility of air in water as a function of temperature. The analytical relationship was mentioned in Chapter III.

7. *cal_sol.m*:

This function computes the solubility of liquid CO₂ in water as a function of temperature, salinity, pressure and fugacity. The analytical relationship and equations used were mentioned earlier in Chapter III.

8. *slip.m*:

This function is used to calculate the slip velocity of the dispersed phase as a function of its diameter as per the empirical equations of Clift et al. (1978) detailed in Chapter II.

3. Graphical User Interface

Figure 14 is a view of the GUI designed for organizing all of the computational work. As seen in the figure, it has the following computational blocks:

1. Choose Integral Model:

This block asks the user to opt either the two-fluid or the mixed-fluid model

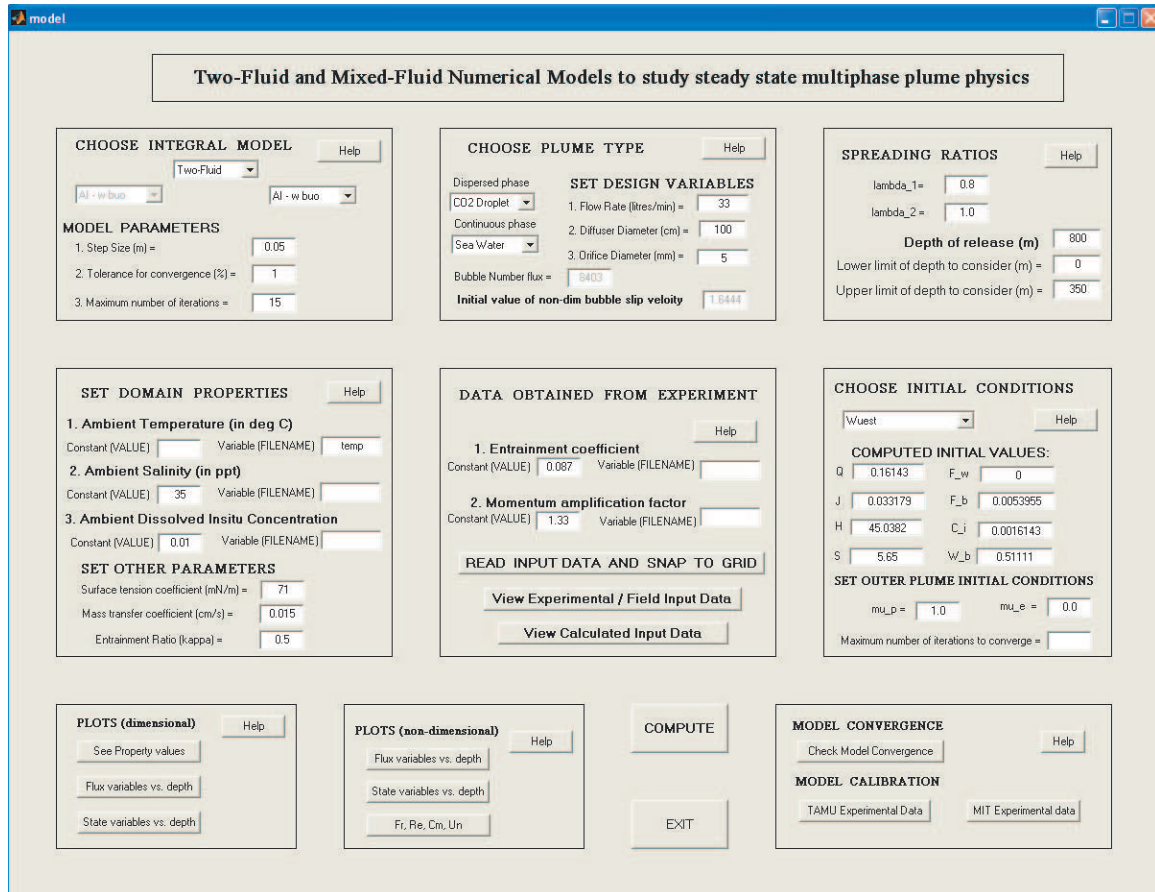


Fig. 14. Graphical user interface designed for the multiphase plume integral models

and takes the inputs $step$, tol and $itmax$.

2. Choose Plume Type:

This block asks the user to select the dispersed and continuous phase based on which the respective phase properties are determined. In the present model, the options are either air-bubbles or liquid CO₂ droplets as the dispersed phase and water as the continuous phase. It also takes the inputs Q_0 , D and d_e from the user. Care must be taken to enter the proper units of the values as asked. The values of the bubble number flux N_b and the non-dimensional slip velocity U_N are calculated later and are displayed as outputs in this block.

3. Specify other constants:

This block takes some other constant inputs namely λ_1 , λ_2 , h , h_{upper} and h_{lower} .

4. Set Domain Parameters:

This block takes the inputs of the ambient properties in the form of the ambient temperature, ambient salinity and ambient concentration, either as constants when a number needs to be entered or as a variable dataset in which case the name of the textfile containing the data should be entered without the extension. The extension (.txt) is appended automatically. The value of σ , β and κ are also asked from the user to be provided as constant inputs.

5. Data obtained from Experiment:

This block asks the user to provide the values of the parameters α and γ either as a number (which is usually a depth-averaged value obtained from experiment) or as a dataset (as a function of depth measured experimentally) when the name of the data file leaving the extension must be entered. After this, by pressing the

button labeled *READ INPUT DATA AND SNAP TO GRID* the model reads all the data varying with depth and maps it to the corresponding generated grid points spaced equally by *step*. The generated data and other relevant data calculated from the primary input data can now be viewed by pressing the buttons labeled *View Experimental/Field Input data* and *View Calculated Input data*.

6. Choose Initial Conditions:

This block asks the user to opt for the specific method of calculating the initial conditions for the first inner plume at the diffuser level which will be discussed in detail in the next chapter. The initial conditions for the first inner plume are calculated and are displayed instantly. For the calculation of the outer plume initial conditions the user has to now input the values of the peeling fraction parameter μ_e and the extra entrainment factor μ_e discussed in detail in the next chapter. The maximum number of iterations needed for the model solution to converge is displayed as output after the computation is complete.

7. Plot Results:

After evaluating the initial conditions, the model is ready to be run and this is done by pressing the button labeled *COMPUTE* which gets deactivated while the program runs and gets activated again at the completion of program execution. After this, the different dimensional and non-dimensional plots of different flux and primary variables vs. depth can be viewed.

8. Convergence Check and Model Verification:

At the extreme right hand corner of the GUI, this block is designed to see how the model solution behaves as the number of iteration increases. If the oscillation dies down progressively within a few iterations, it denotes a stable

and convergent solution. Otherwise the solution should be viewed as chaotic which can happen due to a wrong input or an absurd imaginary number being calculated or if an overflow error occurs as a result of a divide by zero. The chaos in the solution can also happen if the initial conditions are far apart from the equilibrium zone so that the system of coupled ODEs behaves as a highly undamped, oscillatory and chaotic system because of which the convergence criteria is never met.

The button labeled *TAMU Experimental data* compares the model simulation to that of experimentally measured data which is discussed in detail in Chapter VI. The button labeled *MIT Experimental data* when pressed, displays the model results compared to the experimental results of Asaeda & Imberger (1993), Lemckert & Imberger (1993) and Socolofsky & Adams (2005).

9. Exit:

To exit from the GUI, the user has to press the button labeled *EXIT*.

CHAPTER V

INITIAL CONDITIONS

In order to solve the model equations numerically using the Runge-Kutta scheme, starting values for the flux variables must be provided. Moreover, the accuracy of the numerical model prediction is quite sensitive to the initial values of these variables. This means that appropriate initial values of the unknown flux variables - Q , J , F_w , F_b , H , C , S and W_b must be known at the start of computation, that is at the point of release for the first plume and at each subsequent peeling heights for the inner and outer plumes. Physically, the values of Q , J , H , C and S for the inner plumes are equal to zero initially, which gives a starting value of zero for these flux variables. This is because a plume starts with zero initial velocity by definition. Zero values of Q and J however are inadmissible in the numerical scheme as then the solution blows up due to a division by zero. However, appropriate non-zero initial values at the starting level for Q and J can be obtained to obtain a realistic solution at higher depths. The reasoning behind this hypothesis lies in the fact that a plume, by definition, forgets its initial volume and momentum flux. The initial value of F_w is equal to zero because from physics, the buoyancy flux of the dispersed phase, F_b generates a plume. The initial values of F_b and W_b are known from the phase properties. Therefore, the crucial issue is to find ways to evaluate reasonable non-zero initial values for Q and J . In this chapter, a critical review of the different existing theories to evaluate the initial conditions for Q and J for inner as well as outer plumes are discussed. These methods can be classified under three regimes: for the starting inner plume at the diffuser source, for subsequent inner plumes after each peel and for every downdraught outer plume at the peeling locations.

1. Inner Plume Initial Conditions at the Diffuser Source

Recalling that $Q = \pi b^2 \bar{u}$ and $J = \pi b^2 \bar{u}^2$, it is easy to note that specification of non-zero initial values of Q and J essentially means finding appropriate non-zero initial values for the plume velocity \bar{u} and the plume radius b . All theories for the evaluation of initial conditions are based upon this fact.

1.1. Concept of Power Series

McDougall (1978) first proposed the mixed-fluid, double plume integral model to simulate the dynamics of multiphase plumes. To obtain the initial conditions, he obtained a power series formulation for the required parameters using perturbation analysis that provides initial values for the flux variables just above the diffuser. This was based on the assumption that stratification would not change significantly at a very small difference of depth. Asaeda & Imberger (1993) also used the power series formulation to obtain the initial conditions for the first plume.

The power series formulation of McDougall (1978) for the non-dimensional plume radius B and the non-dimensional plume centerline velocity V are as follows:

$$B = x \left[0.6 + 0.01719M^{-1/3}x^{1/3} - 0.002527M^{-2/3}x^{2/3} \right. \\ \left. + x(-0.04609 + 0.000031M^{-1}) + \dots \right] \quad (5.1)$$

and

$$V = x^{-1/3} \left[1.609 - 0.3195M^{-1/3}x^{1/3} + 0.06693M^{-2/3}x^{2/3} \right. \\ \left. + x(0.4536 - 0.0105M^{-1}) + \dots \right] \quad (5.2)$$

where x and M are the non-dimensional height and non-dimensional source strength

given by

$$x = \frac{z}{H} \quad (5.3)$$

and

$$M = \frac{Q_b g}{4\pi\alpha_g^2 H u_s^3} \quad (5.4)$$

where α_g is the entrainment coefficient for Gaussian profiles. The dimensional plume radius b and plume centerline velocity \bar{u} are obtained as

$$b = 2\alpha_g H B \quad (5.5)$$

and

$$U_m = u_s M^{1/3} V \quad (5.6)$$

McDougall (1978) proposed a value of $x = 0.025$ to get the initial values of B and V , where $x = 0$ is defined at the height of the diffuser. The limitation of this method is that it is difficult to ascertain whether or not this value of x is universally applicable for different case studies to generate the initial values of Q and J . This is because x scales on the depth and not the diffuser diameter, so it does not necessarily coincide with a physically meaningful region of the plume, such as the top of the Zone of Flow Establishment (ZFE). Also, since $x = 0.025$ is arbitrary, it may not be useful in some cases, especially when the depth H is large.

1.2. Concept of Virtual Point Source

Ditmars & Cederwall (1974) highlighted the difference between point sources and line sources and said that the diffuser source is not a point source on the basis of the fact that it has finite dimensions. They proposed that the initial conditions at the top

of ZFE can be obtained by a knowledge of the location of the virtual point source somewhere below the diffuser, which they said can be estimated from the diffuser geometry. Liro et al. (1992) approximated the distance between the release point and the location of the virtual source to be equal to five times the diameter of the diffuser source, and that between the top of ZFE and the virtual point source to be equal to ten times the diameter of the diffuser source. This is illustrated in Figure 15.

The expression for the initial plume radius b and the initial plume centerline velocity are obtained by applying analytical solutions for a single-phase plume which are given as follows:

$$b = \frac{6}{5}\alpha_g z_0 \quad (5.7)$$

and

$$U_m = \left(\frac{25gQ_b(1 + \lambda_1^2)}{24\alpha_g^2\pi z_0} \right)^{1/3} \quad (5.8)$$

where $z_0 = 10D$ and α_g is the depth-averaged value of the entrainment coefficient for Gaussian profiles in the ZFE.

The drawback of this method is that the solution to b and U_m given by Eq. (5.7) and Eq. (5.8) are valid strictly for single-phase plumes in an unstratified ambient. There might be significant deviations in these values in case of multiphase plumes and in case of a stratified ambient. This fact is found to be true from experimental measurements (Bergmann et al. 2004) and is illustrated in the next chapter.

1.3. Concept of Densimetric Froude Number

Wüest et al. (1992) proposed an alternative method of obtaining the initial conditions by studying the value of the bubble densimetric Froude number Fr (Fischer, List,

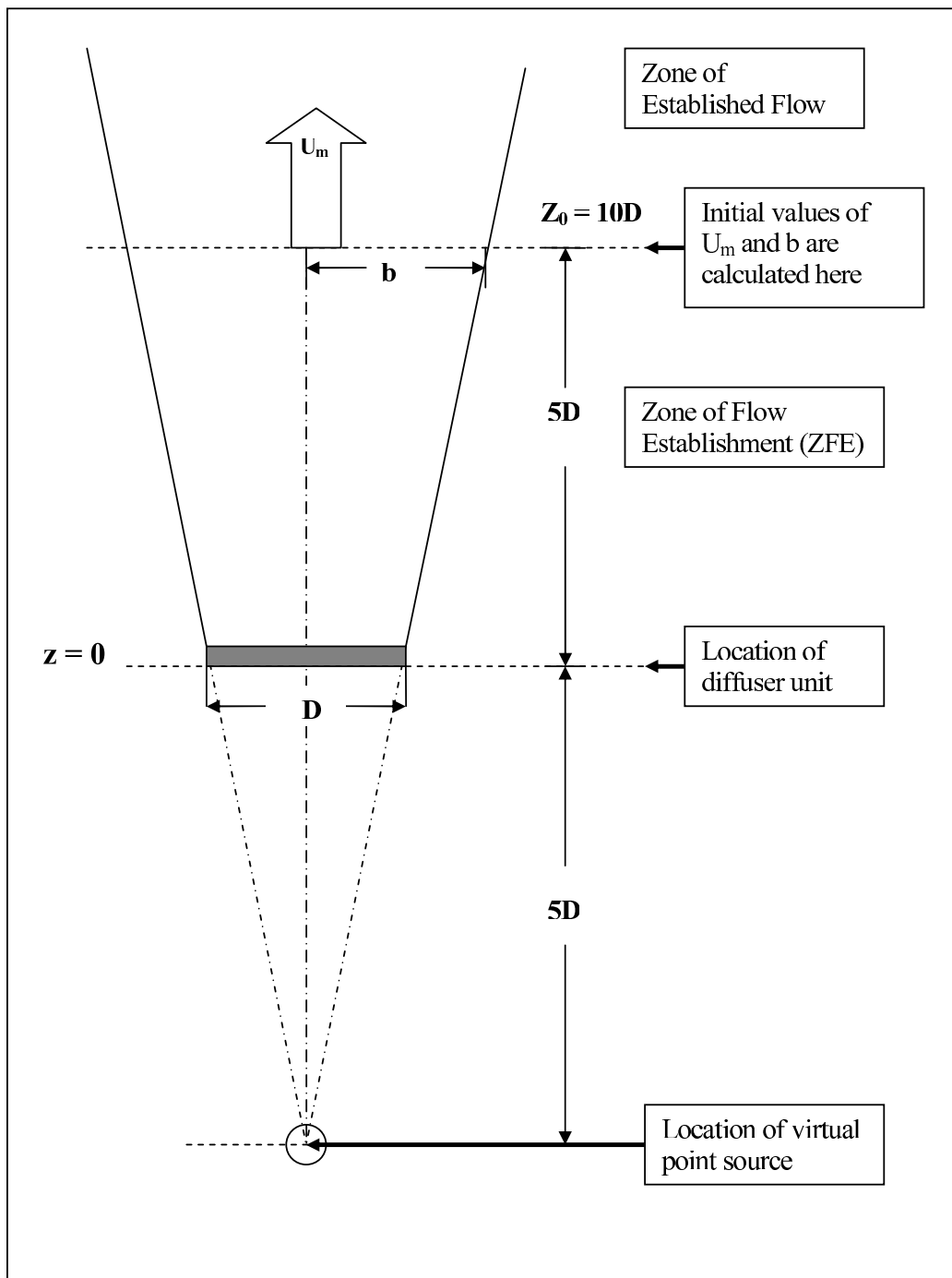


Fig. 15. Illustration of the virtual point source concept

Koh, Imberger & Brooks 1979), which is given by the expression

$$F_r = \frac{\bar{u}}{\left[2\lambda_1 b g \frac{(\rho_a - \rho_p)}{\rho_p}\right]^{1/2}} \quad (5.9)$$

where ρ_p is the plume density given by

$$\rho_p = (1 - \bar{c})\rho_w + \bar{c}\rho_b \quad (5.10)$$

where \bar{c} is the dispersed phase void fraction. Making the dilute plume assumption, we have from Eq. (5.9) and Eq. (5.10)

$$F_r = \frac{\bar{u}}{[2\lambda_1 b g \bar{c}]^{1/2}} \quad (5.11)$$

The void fraction \bar{c} can be computed from an equation relating the volume flux of the dispersed phase which is given by

$$\pi b^2 (\bar{u} + u_s) \bar{c} = Q_b \quad (5.12)$$

which yields

$$\bar{c} = \frac{Q_b}{\pi b^2 (\bar{u} + u_s)} \quad (5.13)$$

Eq. (5.11) and Eq. (5.13) yields a transcendental equation in \bar{u} which can be solved iteratively or graphically. This is given by the equation:

$$\bar{u} = F_r \left[\frac{2\lambda_1 g Q_b}{\pi b (\bar{u} + u_s)} \right]^{1/2} \quad (5.14)$$

Wüest et al. (1992) proposed the initial value of the plume radius b to be equal to the effective radius of the diffuser. The initial value of the Froude number was expected to lie (Wüest et al. 1992) between 1.0 and 1.7 for open sources (lakes or oceans) or between 0.75 and 1.0 for closed sources (experimental tanks). In the present

study, the initial Froude number is kept equal to 0.8 for the case of model calibration when the diffuser unit is placed in a closed experimental tank. For the case studies, the diffuser units are placed at the bottom of a lake or at deeper depths of the ocean and so behave as open sources, so a value of 1.6 is chosen for the initial F_r .

This method preserves the multiphase nature of the plume through the incorporation of the void fraction \bar{c} and spreading ratio λ_1 and is independent of any arbitrary parameter. Therefore this method is believed to be superior to the ones derived by McDougall (1978) and Ditmars & Cederwall (1974).

2. Outer Plume Initial Conditions

The outer plume initial conditions are derived by invoking the conservation principle at the peeling locations as was first proposed by Asaeda & Imberger (1993). However, they assumed a complete 100% peeling. In the present work, this result is extended to a more general case by incorporating a new parameter called the peeling fraction Ω_p . In addition, Socolofsky & Adams (2005) found from experimental observations that there is an enhanced entrainment at the start of the outer plume due to some extra entrainment of ambient fluid. These two phenomena of fractional peeling and extra entrainment are incorporated together through two parameters defined as μ_p and μ_e respectively.

From Asaeda & Imberger (1993) we have for a 100% peeling and zero extra entrainment from ambient,

$$Q_{o(initial)} = -Q_{i(peel)} \quad (5.15)$$

In the presence of fractional peeling and extra entrainment, Eq. (5.15) can be gener-

alized to

$$Q_{o(initial)} = -(\mu_p + \mu_e)Q_{i(peel)} \quad (5.16)$$

Thus, all the outer plume initial variables are essentially a weighted average of the corresponding variables for the inner plume fluid and the ambient fluid at the peeling height in the ratio $\mu_p : \mu_e$, which are given as follows:

$$T_{o(initial)} = \frac{[\mu_p T_{i(peel)} + \mu_e T_{a(peel)}]}{(\mu_p + \mu_e)} \quad (5.17)$$

$$c_{o(initial)} = \frac{[\mu_p c_{i(peel)} + \mu_e c_{a(peel)}]}{(\mu_p + \mu_e)} \quad (5.18)$$

$$s_{o(initial)} = \frac{[\mu_p s_{i(peel)} + \mu_e s_{a(peel)}]}{(\mu_p + \mu_e)} \quad (5.19)$$

$$\rho_{o(initial)} = \frac{[\mu_p \rho_{i(peel)} + \mu_e \rho_{a(peel)}]}{(\mu_p + \mu_e)} \quad (5.20)$$

T , c , s and ρ denote the temperature, concentration, salinity and continuous phase density respectively. Subscripts i , o and a stand for inner, outer and ambient respectively.

Thus, the outer plume initial conditions are given as follows:

$$Q_{o(initial)} = -(\mu_p + \mu_e)Q_{i(peel)} \quad (5.21)$$

$$J_{o(initial)} = (\mu_p + \mu_e)J_{i(peel)} \quad (5.22)$$

$$F_{o(initial)} = \mu_p F_{i(peel)} \quad (5.23)$$

$$H_{o(initial)} = Q_{o(initial)}T_{o(initial)} \quad (5.24)$$

$$C_{o(initial)} = Q_{o(initial)}c_{o(initial)} \quad (5.25)$$

$$S_{o(initial)} = Q_{o(initial)}s_{o(initial)} \quad (5.26)$$

Eq. (5.23) is derived algebraically as follows:

$$\begin{aligned}
F_{o(initial)} &= \left(\frac{\rho_{o(initial)} - \rho_{a(peel)}}{\rho_r} g \right) Q_{o(initial)} \\
&= \left(\frac{\rho_{a(peel)} - \rho_{o(initial)}}{\rho_r} g \right) (\mu_p + \mu_e) Q_{i(peel)} \\
&= \frac{g}{\rho_r} Q_{i(peel)} (\mu_p + \mu_e) \left(\rho_{a(peel)} - \frac{[\mu_p \rho_{i(peel)} + \mu_e \rho_{a(peel)}]}{(\mu_p + \mu_e)} \right) \\
&= \frac{g}{\rho_r} Q_{i(peel)} \mu_p (\rho_{a(peel)} - \rho_{i(peel)}) \\
&= \mu_p \left[\frac{g}{\rho_r} (\rho_{a(peel)} - \rho_{i(peel)}) Q_{i(peel)} \right] \\
&= \mu_p F_{i(peel)}
\end{aligned} \tag{5.27}$$

In the present work, a 100% peeling is assumed so that $\mu_p = 1$. If there is 80% peeling, then μ_p will have a value of 0.8. The enhanced ambient entrainment is neglected in this present work so that $\mu_e = 0$. In the presence of extra entrainment, μ_e will have a value greater than 0. In the special case, when ambient entrainment equals the entrainment from the inner plume with 100% peeling (which is considered to happen when the plume hits the water surface in this present work), μ_e has a value equal to 1. To conclude, μ_p and μ_e are two important parameters, which if experimentally determined, can aid the calibration of numerical models which can then simulate results for double plumes with a much higher degree of completeness and accuracy.

3. Initial Conditions for Subsequent Inner Plumes

3.1. Concept of Bubble Core Radius

For obtaining the initial conditions for the higher plumes after the first peel, Asaeda & Imberger (1993) used the concept of bubble core radius (Kobus 1968). Kobus

(1968) calculated the inner plume radius based on the radius of the bubble core in homogeneous water at any height, which he defined as

$$b = 2\alpha_{th}H \cdot \frac{0.1(x + 0.05)K^{3/8}}{\lambda_1\alpha} \quad (5.28)$$

where where α_{th} is the entrainment coefficient for Top-Hat profiles, $x = \frac{z_p}{H_T}$, z_p being the peel height and

$$K = \tanh \left[\frac{(gQ_0)^{1/3}}{H_A^{1/3}u_s} \right] \quad (5.29)$$

Asaeda & Imberger (1993) used Eq. (5.28) to obtain b required for calculating the initial values for Q and J for all subsequent inner plumes. \bar{u} was then derived analytically on the basis of the assumption that at the start of the inner plume, no outer plume exists and the dominant forcing is only due to the buoyancy of the dispersed phase so that the model equations for the volume flux and momentum flux can be simplified to the form

$$\frac{dQ}{dz} = 2\alpha_{th}\sqrt{\pi J} \quad (5.30)$$

and

$$\frac{dJ}{dz} = \frac{F_b}{\gamma(\bar{u} + u_s)} \quad (5.31)$$

Now differentiating the identity $J = Qu$ we get the equation

$$\begin{aligned} \frac{dJ}{dz} &= \bar{u} \frac{dQ}{dz} + Q \frac{du}{dz} \\ &= \bar{u}2\alpha_{th}\sqrt{\pi J} + \pi b^2\bar{u} \frac{du}{dz} \end{aligned} \quad (5.32)$$

From Eq. (5.30), Eq. (5.31) and Eq. (5.32) we get after making algebraic manipulations

$$2\pi\alpha_{th}b\bar{u}^2(\bar{u} + u_s) + \pi b^2\bar{u}(\bar{u} + u_s)\frac{d\bar{u}}{dz} = \frac{F_b}{\gamma} \quad (5.33)$$

At a small difference of height

$$\frac{d\bar{u}}{dz} = \frac{\Delta\bar{u}}{\Delta z} \quad (5.34)$$

Also since the plume starts with zero initial velocity, $\Delta\bar{u} = \bar{u} - 0 = \bar{u}$ using backward difference, and using this approximation the initial conditions can be specified at a small height Δz above the starting point which is the peel height. This gives

$$2\pi\alpha_{th}b\bar{u}^2(\bar{u} + u_s) + \pi b^2\bar{u}(\bar{u} + u_s)\frac{\bar{u}}{\Delta z} = \frac{F_b}{\gamma} \quad (5.35)$$

which can be simplified to

$$\bar{u}^2(\bar{u} + u_s) \left[2\pi\alpha_{th}b + \frac{\pi b^2}{\Delta z} \right] = \frac{F_b}{\gamma} \quad (5.36)$$

Eq. (5.36) is a cubic equation of the form

$$p_3\bar{u}^3 + p_2\bar{u}^2 + p_1\bar{u} + p_0 = 0 \quad (5.37)$$

where

$$\begin{aligned} p_3 &= 1, \\ p_2 &= u_s, \\ p_1 &= 0, \\ p_0 &= -\frac{F_b}{\gamma} \left[2\pi\alpha_{th}b + \frac{\pi b^2}{\Delta z} \right]^{-1} \end{aligned} \quad (5.38)$$

where

$$F_b = \frac{(\rho_a - \rho_b)}{\rho_r} g Q_b \quad (5.39)$$

This cubic equation Eq. (5.37) has three roots. The maximum real positive root is chosen as the value for \bar{u} . This method is applied for the mixed-fluid model by substituting F_b for F_{mix} .

From Eq. (5.38) it is seen that the value of p_0 depends on b and Δz . This means the initial plume radius must be specified. This is obtained from the bubble core radius as per Eq. (5.28). Hence, \bar{u} can be calculated and the obtained values of \bar{u} and b can be used to calculate the initial values of Q and J at the peel height z_p . This method has the single drawback that it is dependent on specifying the value of Δz to evaluate p_0 , the choice of which has to be done somewhat arbitrarily. However, this is the latest method available till date and hence has been followed in this present work by choosing Δz to be equal to one stepsize. For this value, the models are seen to simulate the higher plumes quite well.

After the values of $\bar{u}(z_p)$ and $b(z_p)$ are obtained for the subsequent inner plume (where z_p is the peel height or the height at which the subsequent inner plume starts), conservation principles are invoked to add the fraction of the fluxes that was not peeled at the peeling location for the previous inner plume to this subsequent inner plume. Hence, the subsequent inner plume initial conditions for the flux variables are given by:

$$Q_{s(initial)} = \pi b^2(z_p) \bar{u}(z_p) + (1 - \mu_p) Q_{i(peel)} \quad (5.40)$$

$$J_{s(initial)} = \pi b^2(z_p) \bar{u}^2(z_p) + (1 - \mu_p) J_{i(peel)} \quad (5.41)$$

$$F_{ws(initial)} = (1 - \mu_p) F_{i(peel)} \quad (5.42)$$

$$F_{bs(initial)} = F_{bi(peel)} \quad (5.43)$$

$$H_{s(initial)} = Q_{s(initial)} T_{i(peel)} \quad (5.44)$$

$$C_{s(initial)} = Q_{s(initial)} C_{i(peel)} \quad (5.45)$$

$$S_{s(initial)} = Q_{s(initial)} S_{i(peel)} \quad (5.46)$$

$$W_{bs(initial)} = W_{bi(peel)} \quad (5.47)$$

$$(5.48)$$

where the subscript s is used to denote subsequent inner plume.

CHAPTER VI

MODEL CALIBRATION

This chapter is devoted to the calibration of the GUI presented in Chapter IV for the two-fluid and mixed-fluid numerical models. The model results have been compared to two different sets of experimental data. The first set is the experiment of air-bubble plumes in unstratified water that was conducted (Bergmann et al. 2004) in the Hydromechanics Laboratory at TAMU, College Station. The second set is the experiment conducted at Parsons Laboratory, MIT (Socolofsky & Adams 2005) in the presence of stratification. The model results are also compared to experimental results of Asaeda & Imberger (1993) and Lemckert & Imberger (1993). The experimental results aid to compare and establish which set of initial conditions for the flux variables (described in Chapter V) and model parameters gives the best match for the model results with that of the experiments. A sensitivity analysis for some of the relevant model parameters, namely α (entrainment coefficient), γ (momentum amplification factor) and λ_1 (bubble spreading ratio) is also performed at the conclusion of this chapter.

1. Experiment in Unstratified Ambient

Using Particle Image Velocimetry (PIV) and Particle Tracking Velocimetry (PTV), this experiment was conducted with an attempt to obtain the value of the entrainment coefficient α and the momentum amplification factor γ as a function of depth z in an unstratified ambient (Bergmann et al. 2004). Figure 16 presents the experimental set-up. The experiment was conducted in a glass tank having dimensions 40 cm x 40 cm x 70 cm (with water filled up to a height of 60 cm) for three different values of the diffuser air-flow rate: 0.5, 1.0 and 1.5 l/min. The interrogation area

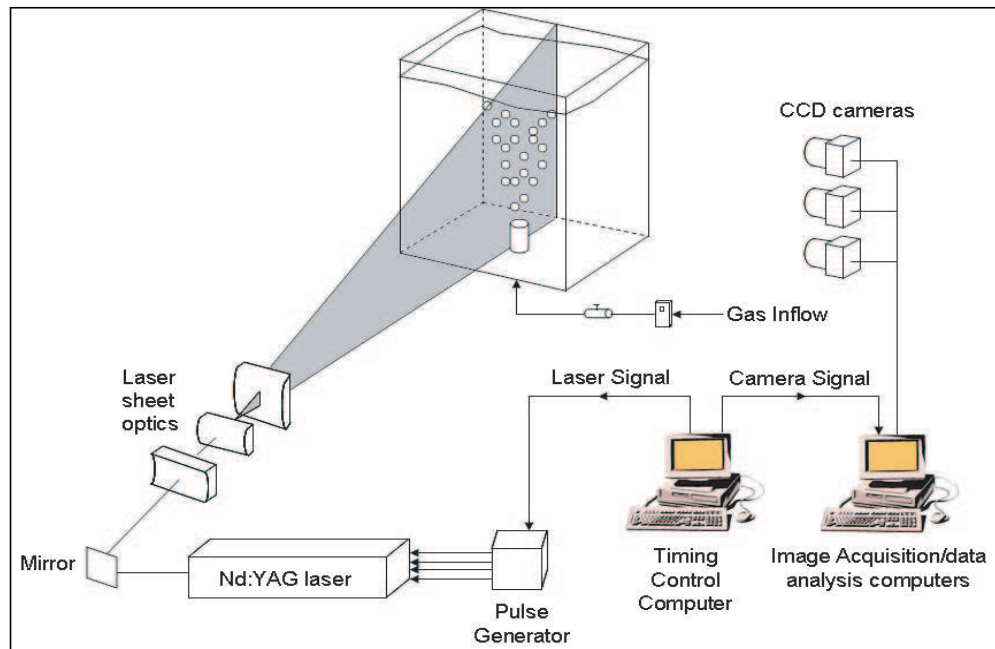


Fig. 16. Experimental set-up to simulate air-bubble plumes in an unstratified ambient (18 cm x 18 cm for each camera) was illuminated by a laser light sheet created by a system of cylindrical lenses from a pulsed laser light source. Tracer particles in the form of white polyamide spheres are used to track the motion of fluid particles (continuous phase) inside the plume. Pictures are recorded in the zone of established flow (Figure 16) within a height of 9 cm and 60 cm from the diffuser level by three high-resolution, 10 and 12-bit CCD cameras. The PIV and PTV analyses are done separately for the velocities of the continuous and dispersed phases. Because of low bubble concentration, the amount of data generated would be too small for PIV to be applied to the bubble velocity measurement, so PTV had to be applied instead for the dispersed phase (Bergmann et al. 2004). On the other hand, PIV could be applied to the mixture of bubbles and fluid with tracer particles. The continuous phase can then be filtered from the bubbles in the image through median filtering. The bubbles on the other hand can be filtered from the tracer particles in the images using a

suitable grayscale intensity threshold because the bubbles are much brighter than the seeding particles. Time-averaged velocity fields are obtained over 1200 frames for the fluid and bubbles after accounting for plume wandering (the tendency for a plume centerline to meander slowly during an experiment).

After obtaining the velocity data for the two phases, appropriate curve fitting techniques are applied to represent the velocity profiles of the two phases. It is found that the continuous phase velocity profile is best represented by a Gaussian distribution function given by

$$u(z, r) = U_m \exp \left(-(r/b)^2 \right) \quad (6.1)$$

where U_m is the centerline velocity and b is the plume radius obtained by non-linear regression. The bubble velocity profile on the other hand is found to be best described by the Monkewitz function (1988), used to describe unbounded wakes given by

$$U_b(z, r) = \frac{U_{bm}}{\left[1 + \left(\sinh\left(\frac{r}{b}\right) \right)^{2N} \right]} \quad (6.2)$$

where N is an integer number greater than 1 to describe the velocity decrease on the edge. A value of $N = 3$ is found to give the best match to the data (Bergmann 2004).

In this thesis, a Top-Hat profile is used to describe the velocity of the continuous phase in the derivation of the model equations listed in Chapter II. Hence to compare the model results with that of the experiment, the appropriate conversion factors to convert Gaussian to Top-Hat versions of the variables are applied as mentioned before in Chapter II.

The slip velocity of the dispersed phase is computed using the simple relation

$$u_s = U_b - u \quad (6.3)$$

Thus, from the experiment, the velocity u of the continuous and U_b of the dispersed phase are directly measured and then the plume radius b is estimated by curve fitting Gaussian profiles. The plume volume and momentum fluxes Q and J , the entrainment coefficient α and the dispersed phase void fraction C are then calculated using the following equations:

$$Q = \pi b^2 \bar{u} \quad (6.4)$$

$$J = \pi b^2 \bar{u}^2 \quad (6.5)$$

$$\alpha = \frac{\frac{dQ}{dz}}{2\pi b \bar{u}} \quad (6.6)$$

$$C = \frac{Q_b(z)}{\pi b^2 (\bar{u} + u_s)} \quad (6.7)$$

The momentum amplification factor γ is calculated by computing the phase distribution number N_P (Milgram 1983) which is given by the following relation:

$$\gamma(N_P) = 1.07 + \frac{D_1}{N_P^{D_2}} \quad (6.8)$$

where

$$N_P = \frac{L_V}{L_D}$$

$$L_V = \frac{U_m^2}{gC}$$

$$L_D = \frac{\sigma}{g(\Delta\rho_b)^{1/2}C^{1/3}}$$

$$D_1 = 977$$

$$D_2 = 1.5$$

σ is the surface tension coefficient for water, discussed earlier in Chapter III. The calculated α , γ and the measured slip velocity u_s for an air flow rate of 0.5 l/min are plotted in Figure 17.

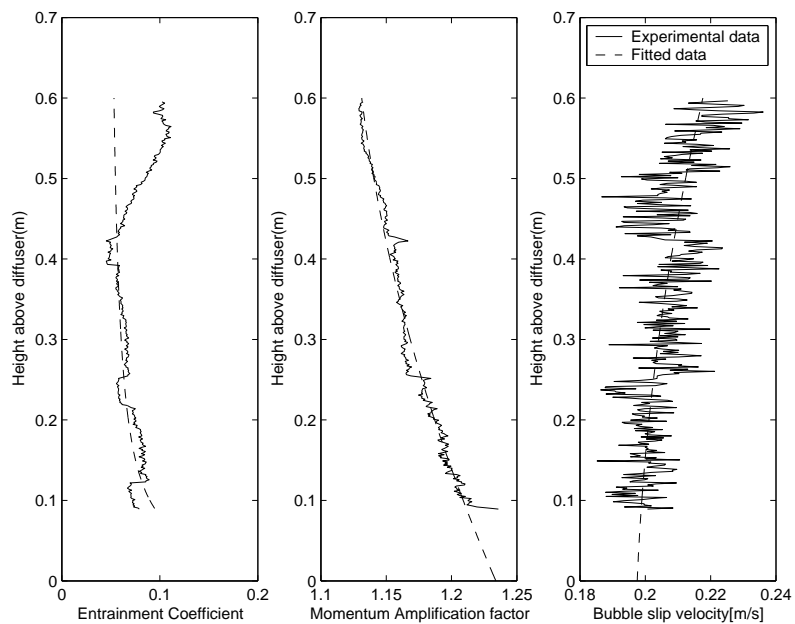


Fig. 17. Calculated values of α , γ and u_s

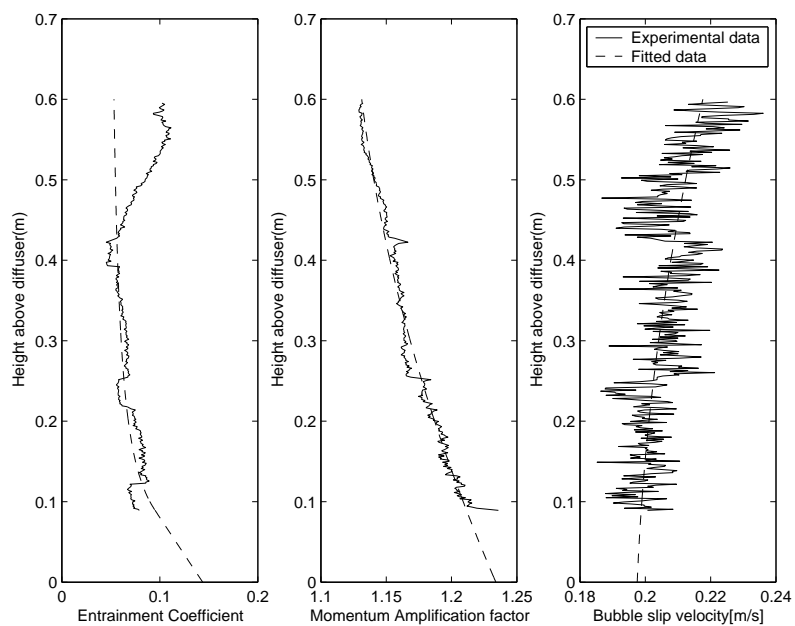


Fig. 18. Extrapolated values of α , γ and u_s

It can be seen from Figure 17 that data is not available in the region of flow establishment, that is, up to a height of 9 cm above the level of the diffuser. This gap is filled by extrapolating the plots in Figure 17 backwards as seen in Figure 18. The mathematical function representing these plots are also obtained as functions of the depth z and are given by the following equations:

$$\alpha(z) = \begin{cases} 0.0004\frac{H_T}{z} + 0.0459, & \text{if } 0.09 \leq z \leq 0.60, \\ -0.5432z + 0.1437, & \text{if } 0 \leq z \leq 0.09 \end{cases} \quad (6.9)$$

$$\gamma(z) = 0.1573z^2 - 0.2655z + 1.2339 \quad (6.10)$$

The depth-averaged values of α (for Gaussian profile) and γ in the Zone of Established Flow are computed to be 0.062 and 1.17 respectively. The corresponding top-hat value of α is 0.087. That is

$$\frac{1}{H-h} \int_h^H \alpha(z) dz = 0.062$$

where $H = 0.6$, $h = 0.09$ and

$$\frac{1}{H-h} \int_h^H \gamma(z) dz = 1.17$$

To obtain the initial conditions for Mcdougall's and Cederwall-Ditmar's methods, the entrainment coefficient in the ZFE is obtained as

$$\frac{1}{h} \int_0^h \alpha(z) dz = 0.119$$

The depth-averaged value of the slip velocity is found to be 0.21 m/s.

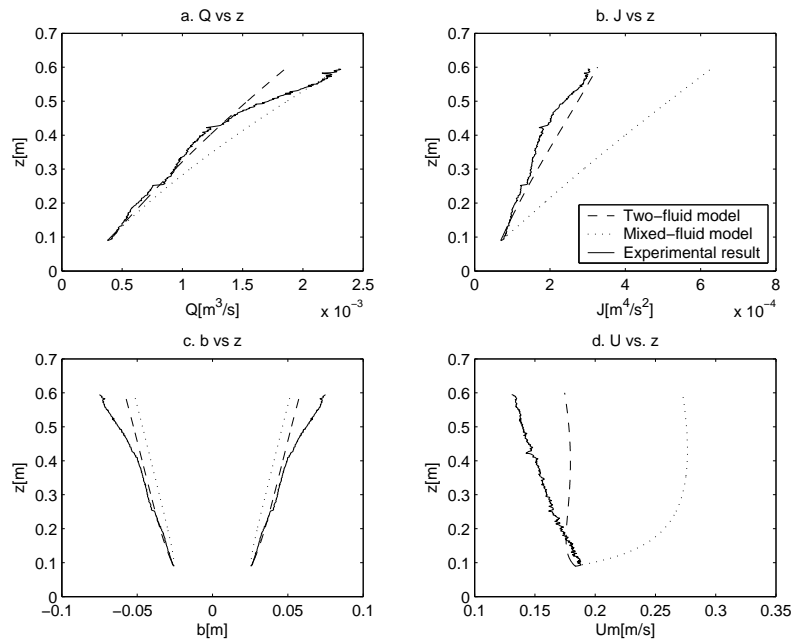


Fig. 19. Dimensional plots of Q , J , u and b vs. z with experimental initial conditions

2. Determination of the Right Choice of Initial Conditions to Match Model Results with Experimental Data

With the incorporation of $\alpha(z)$, $\gamma(z)$ and the mean value of u_s , the mixed-fluid and two-fluid models are first run for a diffuser air flow rate of 0.5 l/min using the initial conditions measured in the experiments, that is starting from a height of 9 cm above the diffuser, and the corresponding dimensional and non-dimensional plots of Q , J , u and b vs. z are shown in Figure 19 and Figure 20.

From Figure 19 and Figure 20 it is seen that the two-fluid model tracks the experimental data quite well whereas the mixed-fluid model overpredicts the continuous phase velocity and the momentum flux. The plots for the dispersed phase void fraction C and the bubble Froude number F_r (shown in Figure 21) also show that the two-fluid model matches the experimental results better than the mixed-fluid model.

Another significant fact to note from Figure 19 is that the two-fluid model un-

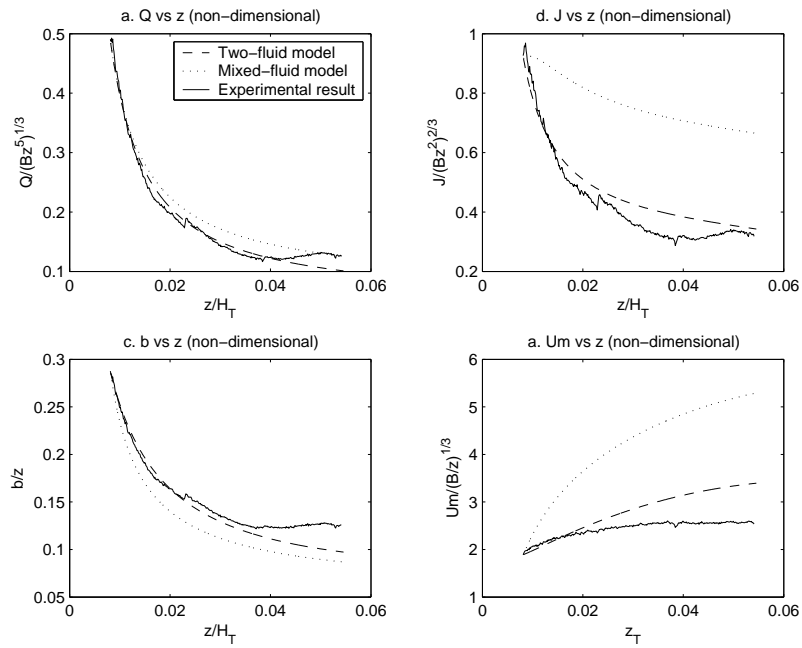


Fig. 20. Non-dimensional plots of Q , J , u and b vs. z with experimental initial conditions

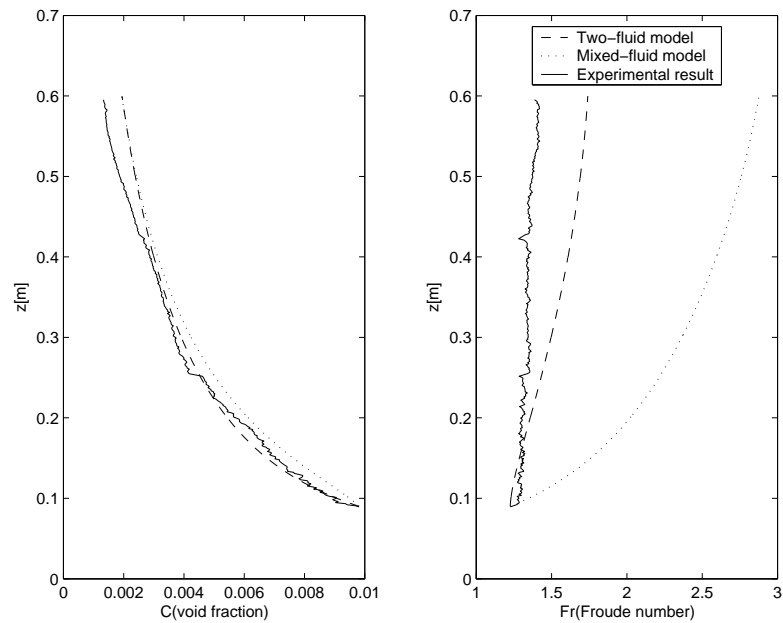


Fig. 21. Plot of C and Fr vs. z with experimental initial conditions

derpredicts the volume flux from a height of 0.4 m to 0.6 m above the diffuser, that is, close to the water surface. The reason is due to recirculation occurring from the surface, whence the entrained volume flux to the plume is increased over this region. The occurrence of recirculation is verified from the plot of entrainment coefficient vs. depth (Figure 17) where it is seen that there is a jump in the value of the entrainment coefficient above a height of 0.4 m, which is calculated based on the experimentally measured volume flux as per Eq. (6.6). Since this recirculation was not modeled in the model equations, therefore the two-fluid model gives a lower value of volume flux as compared to that of the experiment over this region. On the other hand, the mixed fluid model thoroughly overpredicts the volume flux and therefore, cannot explain this phenomenon very well.

The two models are then run starting at the level of the diffuser with initial conditions given by McDougall (1978) and Wüest et al. (1992) and at the start of the zone of established flow (which is five times the diameter of the diffuser above the level of diffuser, in this case equal to 7 cm) with initial conditions given by Ditmars & Cederwall (1974) to give Figure 22 to Figure 33.

From Figure 22 to Figure 24 it is seen that the model results starting with the initial conditions proposed by McDougall (1978) match the volume flux quite well but deviate significantly from the experimental data for the cases of momentum flux, plume radius and continuous phase velocity. The reason has been justified before in Chapter V. The computation of initial conditions as proposed by McDougall (1978) involve H as the length scale which is inappropriate. A more appropriate and physically meaningful length scale should be related to the diffuser geometry in the vicinity of which the initial conditions are calculated. This fact is taken care of in the calculation of initial conditions using the virtual point source concept proposed originally by Ditmars & Cederwall (1974) where the diffuser diameter is used as the

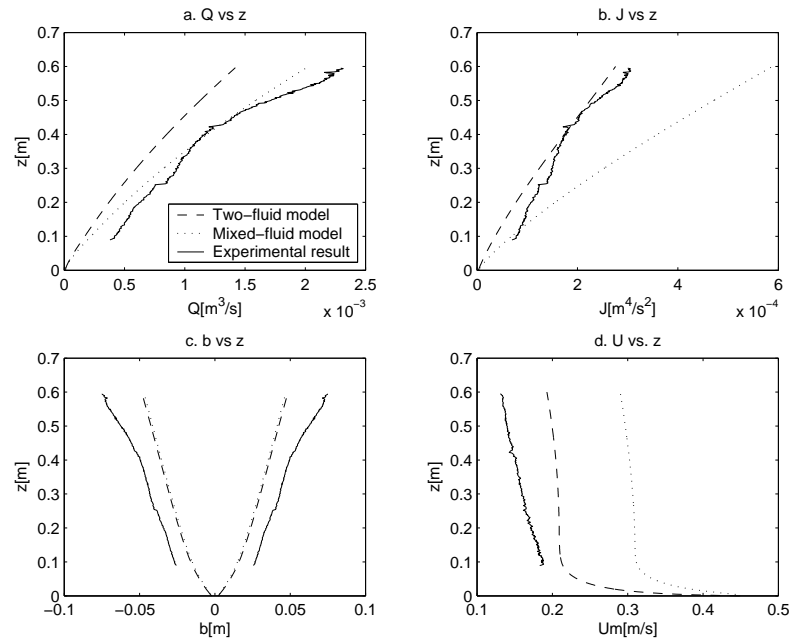


Fig. 22. Dimensional plots of Q , J , u and b vs. z using McDougall's initial conditions

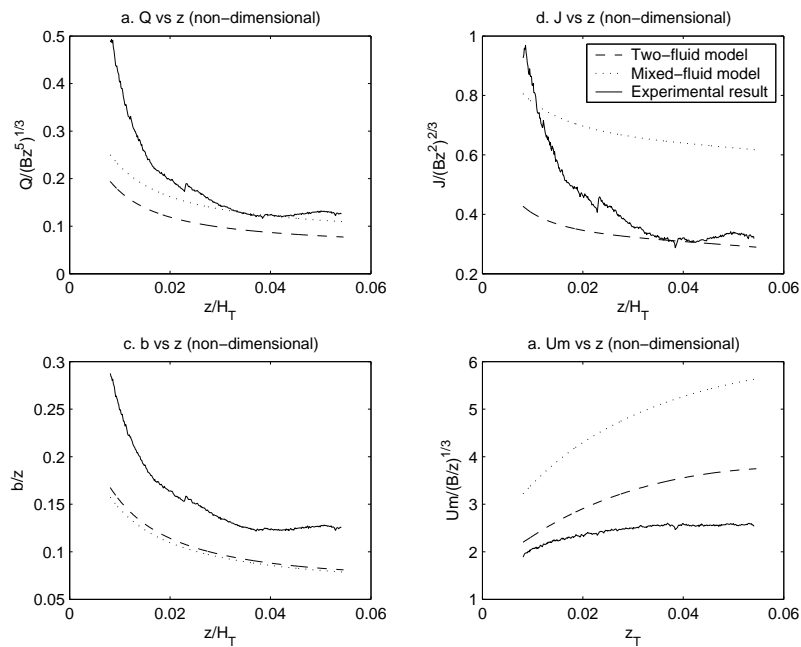


Fig. 23. Non-Dimensional plots of Q , J , u and b vs. z using McDougall's initial conditions

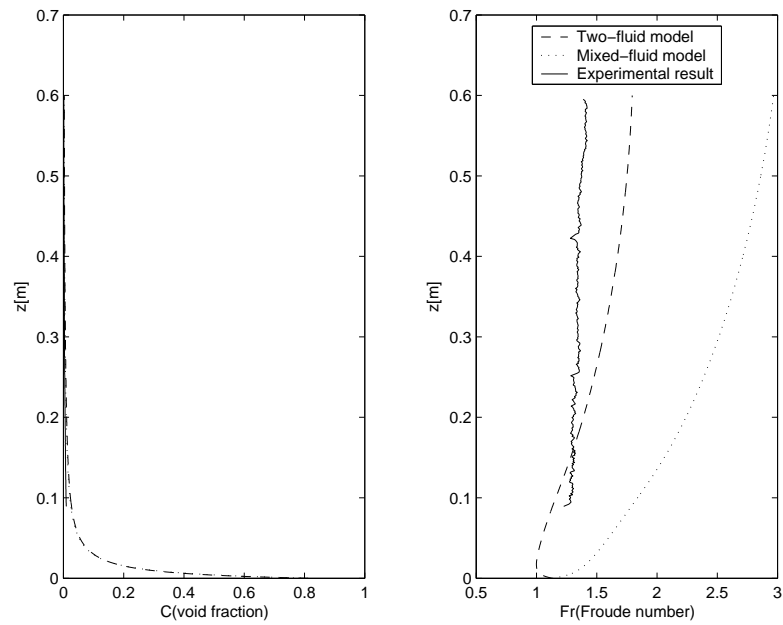


Fig. 24. Plot of C and F_r vs. z for McDougall's initial conditions

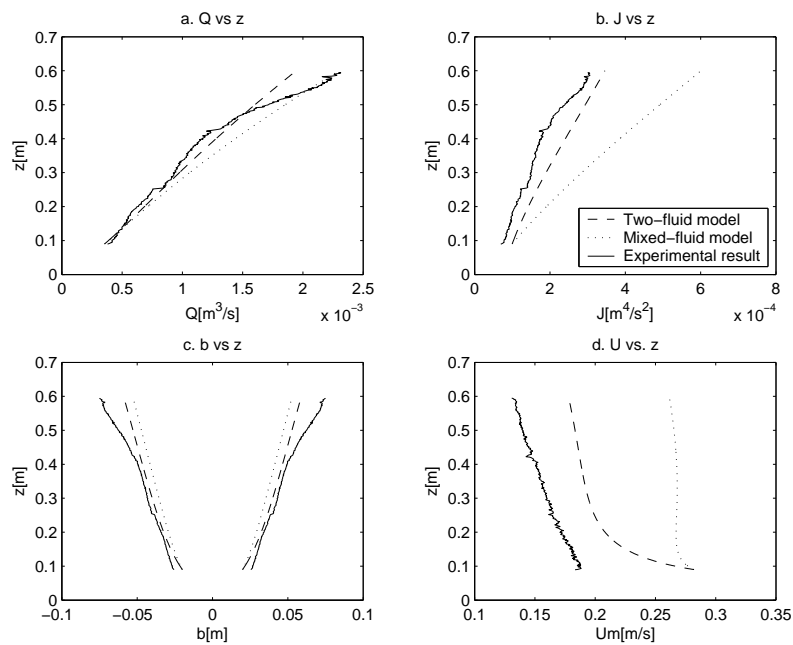


Fig. 25. Dimensional plots of Q , J , u and b vs. z using Cederwall & Ditmars' initial conditions

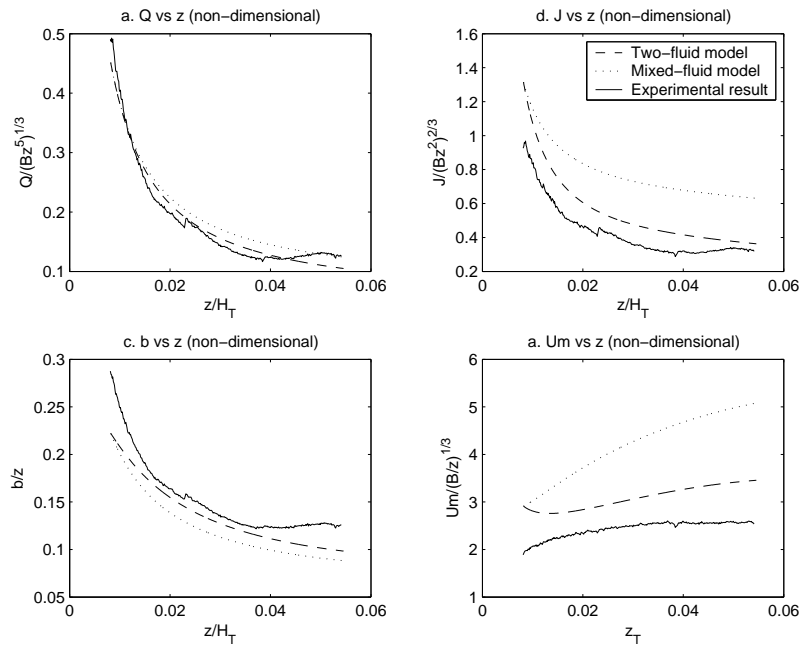


Fig. 26. Non-Dimensional plots of Q , J , u and b vs. z using Cederwall & Ditmars' initial conditions

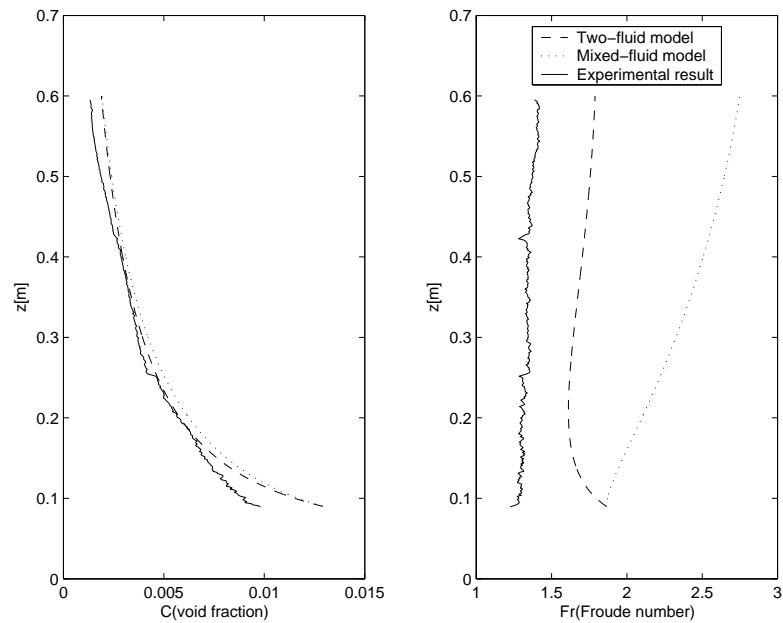


Fig. 27. Plot of C and Fr vs. z for Cederwall & Ditmars' initial conditions

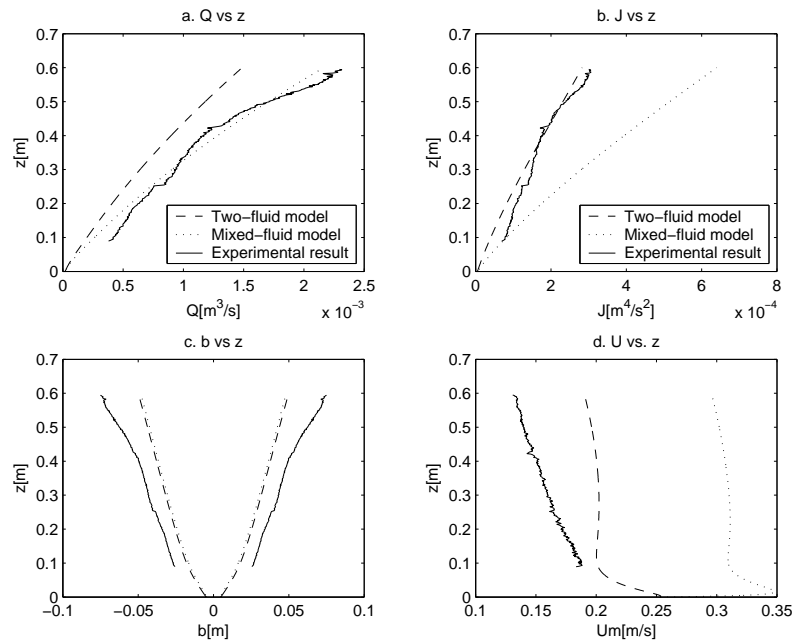


Fig. 28. Dimensional plots of Q , J , u and b vs. z using Wuest's initial conditions with initial $F_r = 0.8$

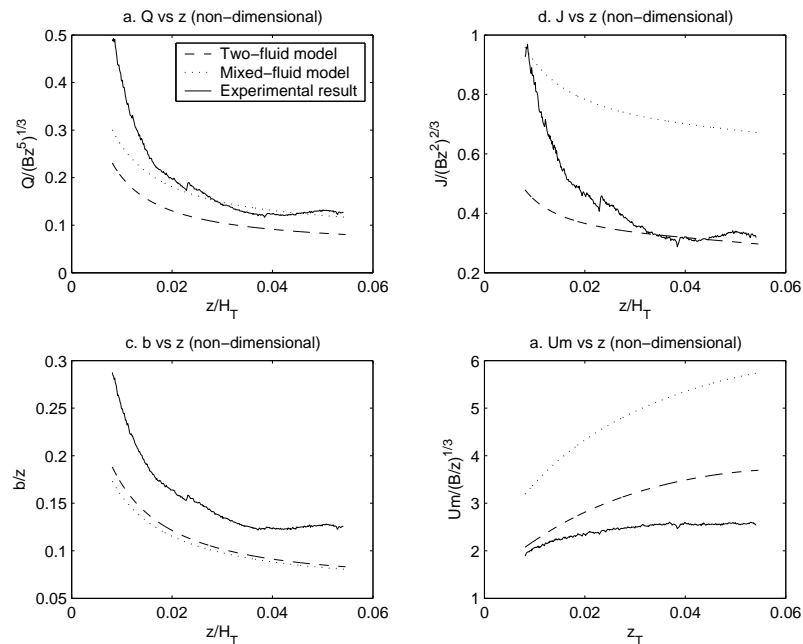


Fig. 29. Non-Dimensional plots of Q , J , u and b vs. z using Wuest's initial conditions with initial $F_r = 0.8$

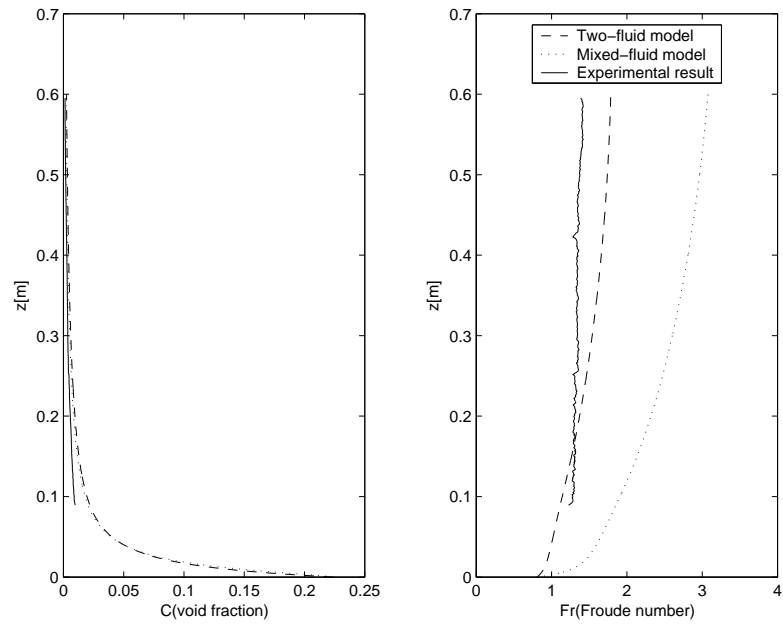


Fig. 30. Plot of C and F_r vs. z for Wuest's initial conditions with initial $F_r = 0.8$

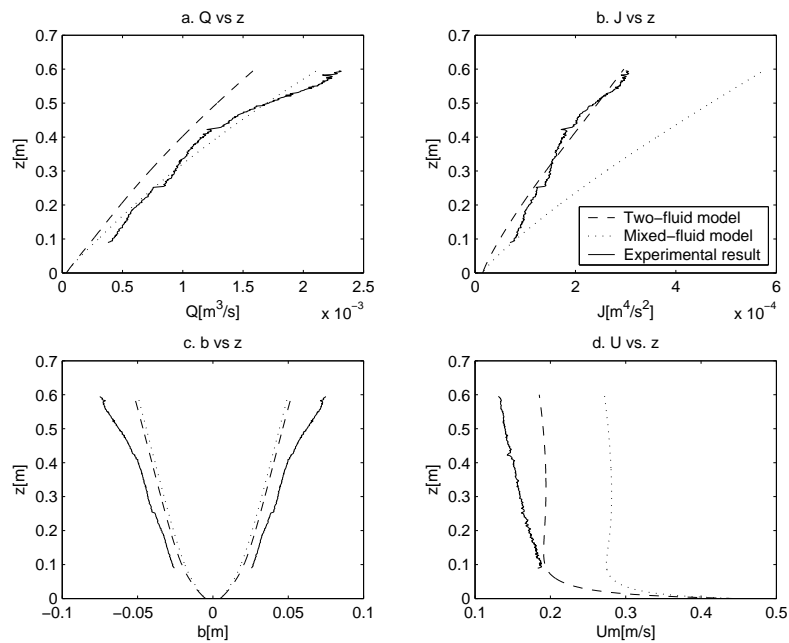


Fig. 31. Dimensional plots of Q , J , u and b vs. z using Wuest's initial conditions with initial $F_r = 1.6$

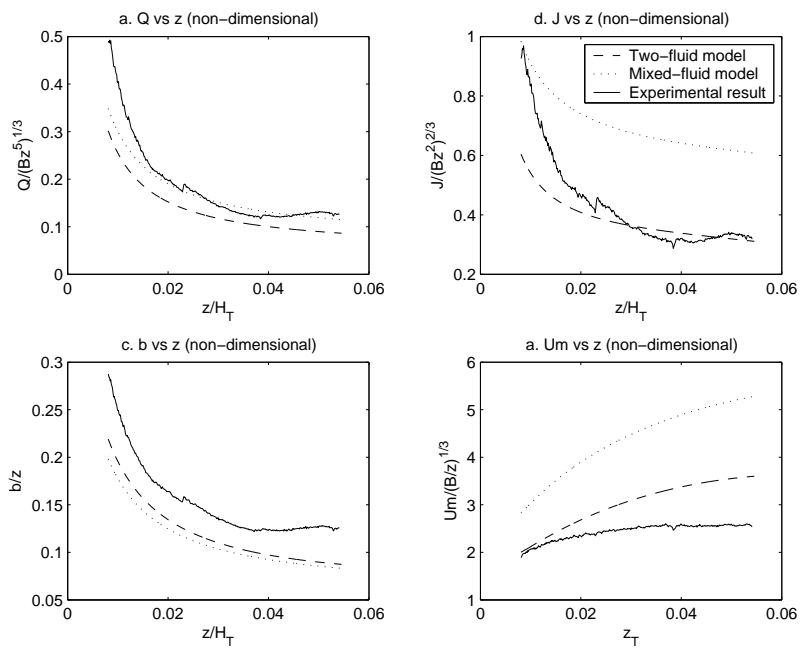


Fig. 32. Non-Dimensional plots of Q , J , u and b vs. z using Wuest's initial conditions with initial $F_r = 1.6$

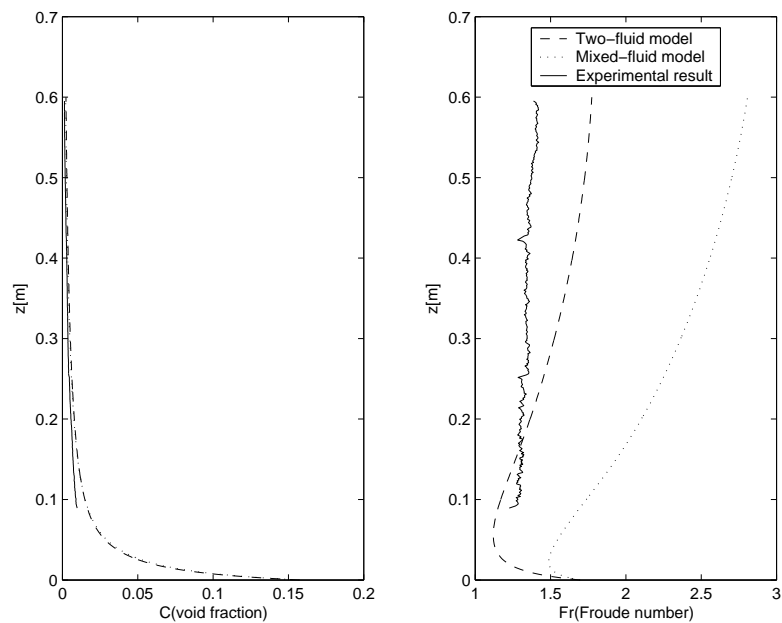


Fig. 33. Plot of C and Fr vs. z for Wuest's initial conditions with initial $F_r = 1.6$

length scale. Figure 25 to Figure 27 also confirm the validity of the virtual point source concept. The model results are found to track the experimental data quite closely from the start of the zone of established flow. The limitations of using the initial conditions of Ditmars & Cederwall (1974) is seen in the plot of Froude number vs. depth in Figure 27. It is seen that the value of the Froude number is overpredicted by both models. Figure 28 to Figure 30 and Figure 31 to Figure 33 are the plots obtained for model results obtained starting with the initial conditions proposed by Wüest et al. (1992) based on the bubble densimetric Froude number (F_r) concept with initial values of F_r equal to 0.8 and 1.6 respectively. The merits of this method of obtaining the initial conditions lie in the facts that the experimental data is tracked quite well starting right from the diffuser level and that the bubble Froude number and bubble void fraction are matched better as seen in Figure 30 and Figure 33. A comparison of Figure 30 and Figure 33 shows that for closed experimental tanks (closed sources), an initial Froude number of 0.8 is more appropriate because it gives a steady increase in the value of F_r as expected, which confirms the findings of Wüest et al. (1992).

A general trend that can be seen from all of the comparison plots is that the mixed-fluid and two-fluid models differ largely in the prediction of the plume velocity, momentum flux and bubble froude number and that the latter predicts all of these parameters much better than the former. Also it is seen that among all the applied methods of obtaining the initial conditions, the one proposed by Wüest et al. (1992) tracks the experimental measurements right from the diffuser level onwards most closely.

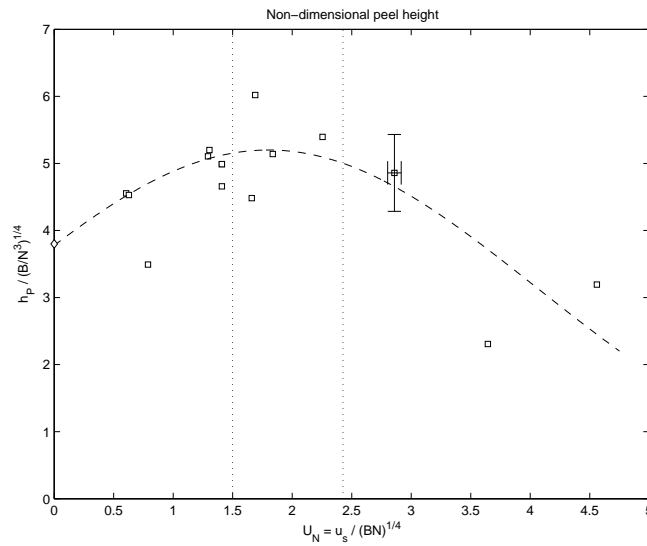


Fig. 34. Correlation of plume peel height to U_N . All data are from Socolofsky and Adams (2005). Typical error bars are shown for one data point.

3. Verification of Model Results against Experiments in Stratified Ambient

A series of experiments in stagnant stratification was performed (Socolofsky & Adams 2005) in a 1.2 m square by 2.4 m tall tank filled with water stratified with sodium chloride. Laser Induced Fluorescence (LIF) was used as the flow visualization technique using Rhodamine 6G fluorescent dye. The non-dimensional plume peel and trap heights as a function of the non-dimensional slip velocity were then plotted along with the experimental data obtained by previous researchers (Asaeda & Imberger 1993, Lemckert & Imberger 1993). These are shown in Figure 34 and Figure 35.

The equations for the best fit curves for non-dimensional peel and trap heights H_{Pn} and H_{Tn} as functions of the non-dimensional slip velocity U_N as obtained by Socolofsky & Adams (2005) are as follows:

$$H_{Pn} = 5.2 \exp\left(-\frac{(U_N - 1.8)^2}{3.2^2}\right) \quad (6.14)$$

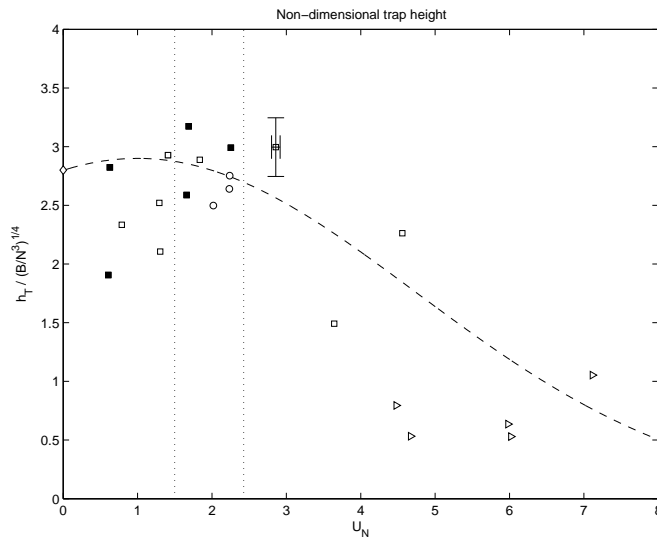


Fig. 35. Correlation of plume trap height to U_N . Right-pointing triangles are data from Lemckert and Imberger (1993), circles are from Asaeda and Imberger (1993) and squares are from Socolofsky and Adams (2005). Open symbols are air bubble experiments; closed symbols are glass bead experiments. Typical error bars are shown for one data point.

$$H_{Tn} = 2.9 \exp\left(-\frac{(U_N - 1.0)^2}{5.3^2}\right) \quad (6.15)$$

The models were then run with similar initial values of B and N as in the experiment (equal to $2 \times 10^{-5} \text{ m}^4/\text{s}^3$ and 0.3 s^{-1} respectively) and variable u_s to compare to the experiments.

The two-fluid model is run with all three different initial conditions and for different values of the initial slip velocity (that is, bubble radius) and the first peel and trap heights are recorded. Figure 36 presents this plot. The entrainment coefficient α and the momentum amplification factor γ are kept constant at their mean values obtained in the last section, that is, 0.087 and 1.17 respectively for α_{th} and γ .

The mixed-fluid model is then run with all four different initial conditions described in Chapter V and for different values of the initial slip velocity, and keeping

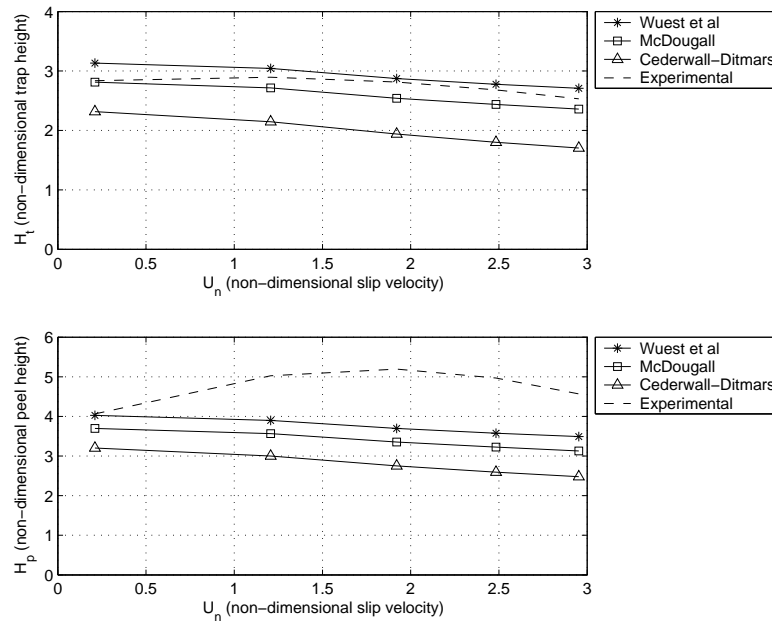


Fig. 36. Two-fluid model results for different initial conditions

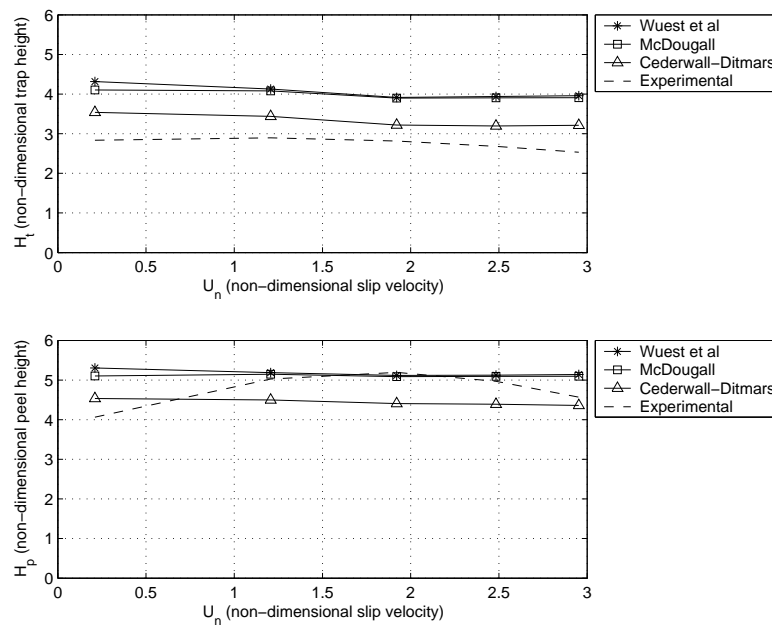


Fig. 37. Mixed-fluid model results for different initial conditions

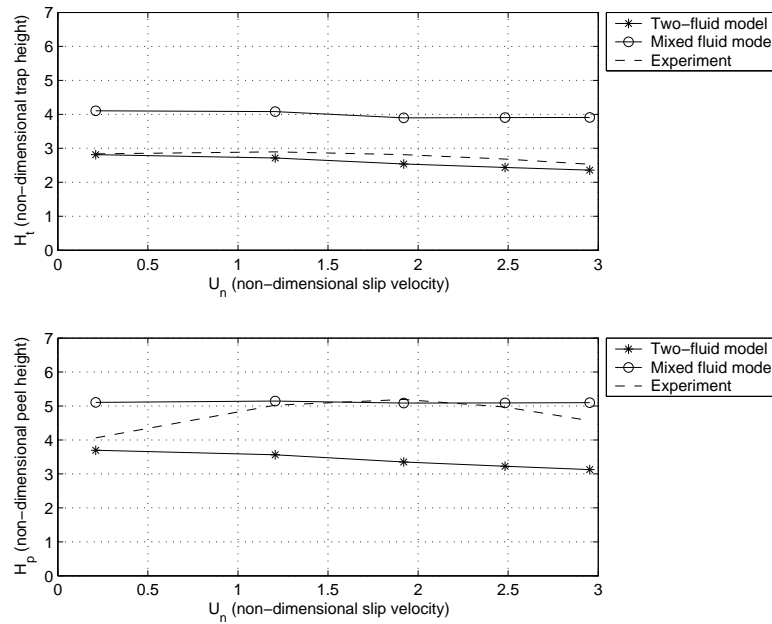


Fig. 38. Comparison of the two-fluid and the mixed-fluid model

α , γ and the other model parameters the same as those in the two-fluid model. The result is shown in Figure 37.

From Figure 36 and Figure 37 it is seen that the two-fluid as well as the mixed-fluid models starting with Wuest's initial conditions matches the fitted curve for trap height for the experimental data appreciably well.

A comparison of the two model results as seen in Figure 38 shows that the mixed-fluid model overpredicts the trap height and matches the peel height, whereas, the two-fluid model underpredicts the peel height and matches the trap height. In the region of Type 2 plumes ($1.5 \leq U_N \leq 2.4$) the two-fluid model underpredicts the peel height, but the reason for this discrepancy is most probably due to the assumption of a 100% peeling in the model to get the outer plume initial conditions discussed in Chapter V, while the experiment showed about 80–90% (Socolofsky & Adams 2005). So if the proper outer plume initial conditions are incorporated taking the phenomena

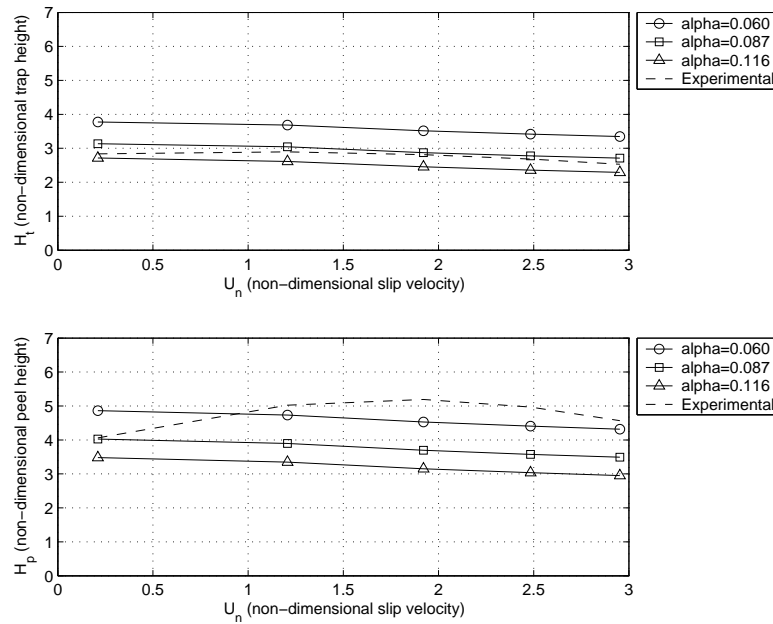


Fig. 39. Sensitivity of model to α

of fractional peeling and added entrainment into account, the two-fluid model results will most likely match up better with the experimental peel heights. The mismatch is also partly explained by the fact that the values of α and γ that are chosen here were calibrated from an experiment conducted in an unstratified ambient (detailed in the last section) with a much higher flow rate (initial B of $8 \times 10^{-5} \text{ m}^4/\text{s}^3$) which is four times the present case. The correct estimation of the peel height is dependent upon the correct calibration of the model parameters α and γ for a given flowrate in the presence of a stratified ambient, which however is an issue of future research and is outside the present scope of work. A sensitivity analysis of the model parameters α , γ and λ is performed instead and is discussed in the next section.

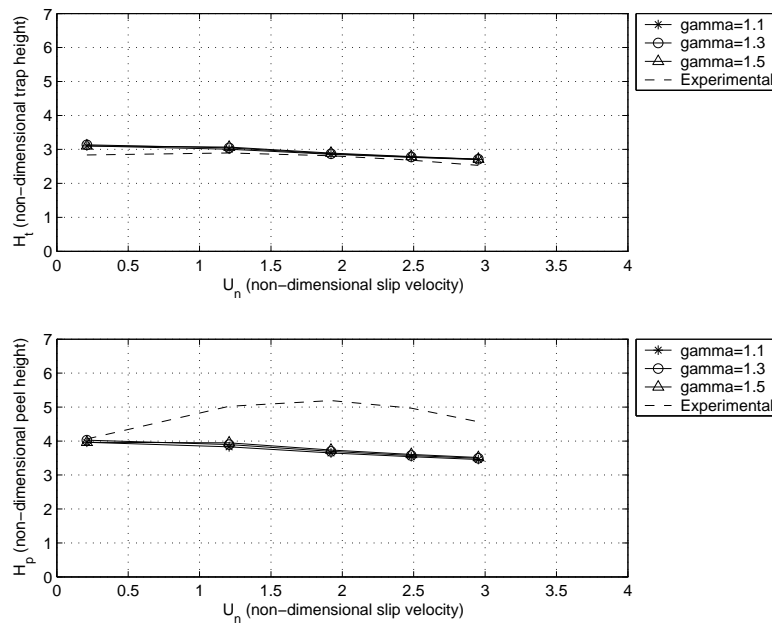
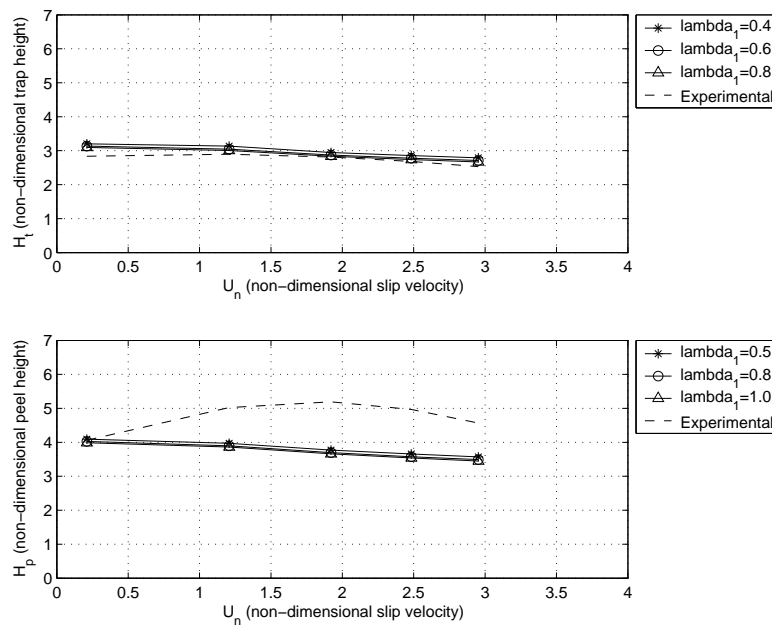
Fig. 40. Sensitivity of model to γ Fig. 41. Sensitivity of model to λ_1

Table 1. Best-fit model parameters

Model parameter	Value
α (Top-Hat)	0.087
γ	1.2
λ_1	0.8
κ	0.5

4. Sensitivity Analysis

Sensitivity analyses for α , γ and λ_1 are performed keeping other variables constant and this is represented in Figure 39 to Figure 41. The two-fluid model was run with values of α made equal to 0.060, 0,087 and 0.116, values of γ made equal to 1.1, 1.3 and 1.5 and values of λ_1 made equal to 0.4, 0.6 and 0.8. The base case values are $\alpha = 0.087$, $\gamma = 1.3$ and $\lambda_1 = 0.8$ with Wuest's initial conditions with an initial F_r of 0.8. It is seen from the plots that the model results are quite insensitive to the values of γ and λ_1 but is somewhat sensitive to the value of α . For the present case with a weak air-flow rate of about 0.12 l/min (that yields $B = 2 \times 10^{-5} \text{ m}^4/\text{s}^3$), it is seen that the peel height is matched better with lower values of α .

Lastly, the model sensitivity to the value of κ where

$$\kappa = \frac{\alpha_{inner-to-outer}}{\alpha_{outer-to-inner}} \quad (6.16)$$

is examined for values of κ made equal to 0.25, 0.5 and 0.75. It is seen from Figure 42 that $\kappa = 0.5$ gives the best match for the trap height which agrees with the findings of Asaeda & Imberger (1993). The peel heights are best matched for a value of κ lying between 0.25 and 0.5. This result is not conclusive however as a value of $\kappa = 0.4$ would correspond to a pure jet entrainment (Asaeda & Imberger 1993). However it can be conclusively said that a proper combination of the values of α

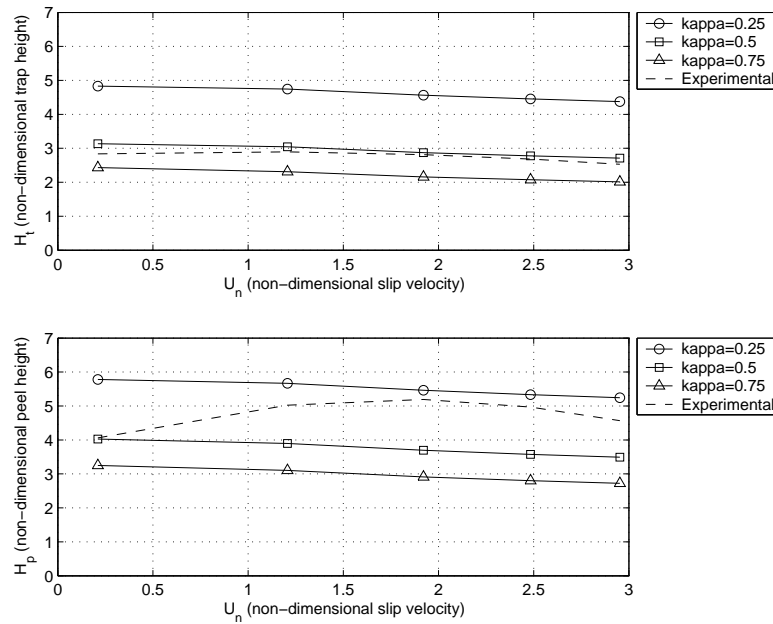


Fig. 42. Sensitivity of model to κ

and κ and a reasonable choice of values of γ and λ_1 with the proper outer plume initial conditions incorporated based on the dual phenomena of fractional peeling and enhanced entrainment can prove to be sufficient to match experimental results with numerical model predictions. Based on the best match to experimental data and the sensitivity analysis, the values of the model parameters that will be used for the field scale case studies are listed in Table 1.

CHAPTER VII

MODEL APPLICATIONS

The two-fluid and mixed-fluid numerical model results have been verified against experimental measurements in Chapter VI with the result that the model parameters could be appropriately calibrated so that the models could be run to yield realistic predictions for the field scale. The application of the two-fluid and mixed-fluid numerical models to simulate field scale phenomena are now discussed in this chapter. Three real cases are chosen to apply the numerical models with a dual purpose of assessing the usefulness and applicability of the models in practical scenarios, and to better understand what the implications of the differences in the results produced by the two different modeling approaches have in actual field studies. The chosen case studies referred to as Cases 1, 2 and 3 respectively have been outlined in Chapter I, and are as follows:

1. Lake Destratification
2. Lake Aeration
3. Ocean Sequestration of Liquid CO₂

To begin with, specific values of the model parameters lying within the calibrated ranges are chosen based on a comprehensive literature review. The selected sets of parameters form the base case parameters that serve as proper inputs to the GUI and are presented in Table 2. The two-fluid and the mixed-fluid models have been run for these three base cases with the objective of studying how differently the two models predict the several important parameters. These are now illustrated in detail one by one.

Table 2. Base case parameters

Parameter	Unit	Case 1	Case 2	Case 3
Release depth (H)	m	50.0	50.0	800.0
z_{min}	m	0.0	0.0	0.0
z_{max}	m	50.0	50.0	350.0
Droplet diameter (d_b)	mm	10.0	2.0	5.0
Diffuser flowrate (Q_0)	lit/sec	12.0	6.0	1.1
Diffuser diameter (D)	m	7.0	7.0	1.0
α_1 (Top-Hat)		0.087	0.087	0.087
α_2 (Top-Hat)		0.0435	0.0435	0.0435
α_3 (Top-Hat)		0.087	0.087	0.087
κ		0.5	0.5	0.5
γ		1.2	1.2	1.2
λ_1		0.8	0.8	0.8
λ_2		1.0	1.0	1.0
β	cm/s	0.04	0.04	0.015
σ	mN/m	71	71	71
μ_p		1.0	1.0	1.0
μ_e		0.0	0.0	0.0
Mass transfer coefficient ratio		1	1	0.5
Stepsize	m	0.05	0.05	0.05
I.C (First inner plume)		Wüest <i>et.al</i>	Wüest <i>et.al</i>	Wüest <i>et.al</i>
I.C (Subsequent inner plumes)		Asaeda <i>et.al</i>	Asaeda <i>et.al</i>	Asaeda <i>et.al</i>
F_r (at level of diffuser)		1.6	1.6	1.6
U_N (at level of diffuser)		1.84	2.25	2.41

1. Lake Destratification

Use of air-bubble plumes for artificial destratification of lakes is commonly practised to prevent the possibility of oxygen depletion in hypolimnetic waters that have become isolated from the water surface (Schladow 1993). The goal of destratification is to destroy the existing stratification gradient and produce a well-mixed system. This essentially means having to raise the potential energy of the lake and this is done by supplying kinetic energy of air-bubble plumes by releasing compressed air through a diffuser at the bottom of the lake. The required isothermal work of compression multiplied by a factor, which is the efficiency of conversion of mechanical energy gives

Table 3. Lake temperature data taken from Nepf(1995)

Depth	Temperature	Salinity	Cross-sectional Area	Density
z	$T(z)$	$S(z)$	$A(z)$	$\rho(z)$
m	$^{\circ}\text{C}$	psu	m^2	kg/m^3
0.0	22.2	0	15.0	997.7729
5.0	19.1	0	13.5	998.4558
8.0	12.8	0	12.8	998.4879
10.0	8.4	0	12.0	999.9204
13.0	6.4	0	11.2	1000.0394
15.0	5.9	0	10.5	1000.0660
20.0	5.5	0	9.0	1000.1007
30.0	5.3	0	6.0	1000.1528
40.0	5.1	0	3.0	1000.2044
50.0	5.0	0	0.0	1000.2537

the required potential energy to destratify the lake. The value of the mechanical efficiency can be obtained from available design charts.

In the present work, a hypothetical non-saline lake of 50 m depth has been chosen having a non-linear stratification with the objective of finding the optimal value of the diffuser air flowrate needed to destratify the lake based on the mixed-fluid and the two-fluid modeling approaches. The temperature data is from (Nepf 1995) and is presented in Table 3. The equation of state has been used to compute the density of water from the temperature and salinity data corresponding to each level. The computed densities and the stratification frequency N for the lake are shown in Figure 43.

Schladow (1993) has described a design procedure based on the design charts of mechanical efficiency consisting of a set of $M - \Delta T$ curves for different values of the water depth h , derived originally by Asaeda & Imberger (1993) in the presence of lin-

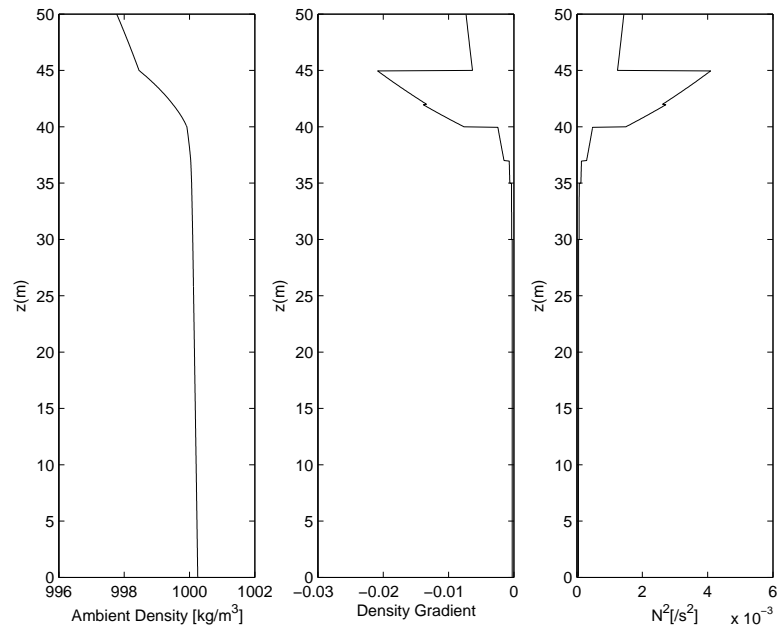


Fig. 43. Density stratification for the lake

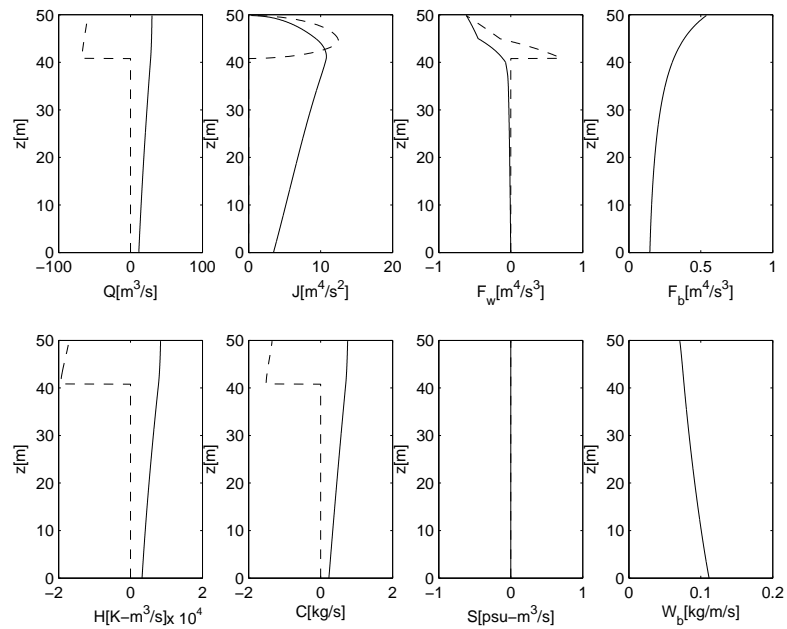


Fig. 44. Numerical simulation of air-bubble for the lake using the two-fluid modeling approach. $Q_0 = 15.0$ l/s in this figure which gives the first peel at the water surface. Bold lines denote the inner plume and dashed lines denote the outer plume.

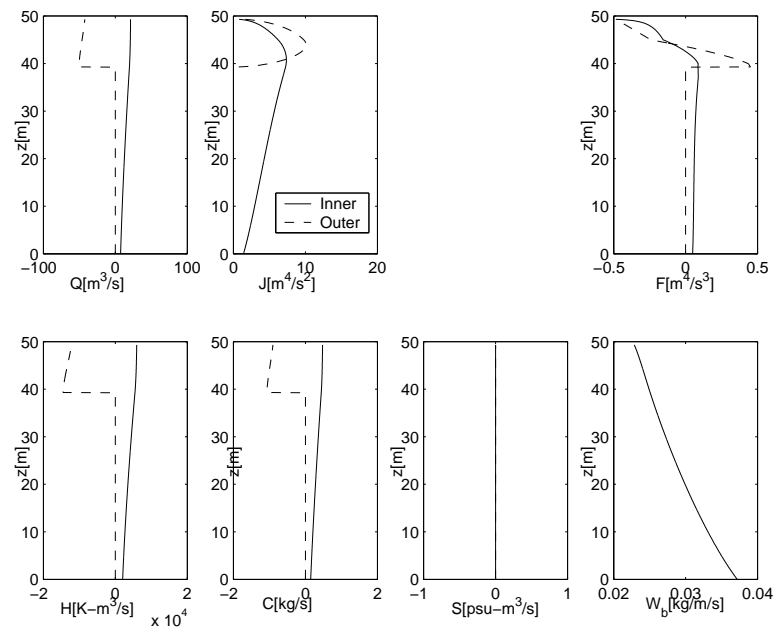


Fig. 45. Numerical simulation of air-bubble for the lake using the mixed-fluid modeling approach. $Q_0 = 5.0$ l/s in this figure which gives the first peel at the water surface. Bold lines denote the inner plume and dashed lines denote the outer plume.

ear stratification. The basic principle behind these design charts is that the efficiency of a bubble plume in destratifying a water column is dependent on two parameters M and C , where M denotes a non-dimensional bubble source strength parameter and ΔT denotes a non-dimensional stratification parameter. For the optimal case, the diffuser air flow rate produces a plume that is just strong enough so that it overcomes the stratification of the lake, thereby achieving complete mixing. This means that for the most efficient destratification system design, the bubble plume should peel just at the water depth, that is, the plume of entrained water has just sufficient kinetic energy to reach the surface of the lake with no intermediate peeling. The second most efficient design corresponds to the situation of a two-tiered plume, that is the plume reaches the surface at its second peeling height with one intermediate peel. Therefore, the bottomline of an efficient design of a destratification system is the fact that there are only certain optimal values of the diffuser air flowrate Q_0 which will ensure peelings happening just at the water surface, based on which the optimal power supply necessary to carry the plume to the surface can be computed. Any value of Q_0 other than these optimal values would mean unnecessary excess power input.

The two-fluid and mixed-fluid numerical models are run using the temperature and salinity data of the lake given in Table 3 and the different flux variables are computed. Figure 44 and Figure 45 are the plotted results of the computations. In both the plots it is seen from the plot of J (momentum flux) vs. depth that peeling occurs (where the momentum flux becomes zero) for the first time at the surface of the lake. This condition was obtained after several runs of the model with different trial values of the diffuser air flowrate Q_0 for a fixed bubble diameter d_e equal to 10 mm. It was found that the two-fluid and mixed-fluid models give quite different values of the optimal Q_0 corresponding to the first peel happening at the water surface. While the two-fluid model predicts the optimal Q_0 as 15.0 l/s, the mixed-fluid model predicts

$Q_0 = 5.0$ l/s as the optimal flowrate required for the best design, which is three times less than the former value. The consequence of this fact in the design of an efficient bubble plume destratification system for a lake is significant because this essentially means having to reconstruct the design charts for obtaining the mechanical efficiency. This is due to the reason that the design charts of Asaeda & Imberger (1993) and Schladow (1993) were prepared on the basis of determination of optimal values of Q_0 using the mixed-fluid model. Now, if the two-fluid model is used to obtain the optimal values of Q_0 , the values obtained will be widely different so that all the curves in the original design charts will completely change.

2. Lake Aeration

Thermal stratification of lakes during summer may result in lowered dissolved oxygen levels below the thermocline of lakes and reservoirs (Schladow 1993) leading to widespread fish kills and stimulation of phosphorus release from bottom sediments resulting in degradation of water quality (Chow 2004). Among the proposed remedies, oxygen injection by diffusers in the anoxic hypolimnion deserve special mention and several researchers (McGinnis et al. 2004) have proposed efficient lake aeration systems to accomplish this task. The bubble diffuser system *Tanytarsus* designed by two Swiss engineers, E. Jungo and U. Schaffner can be used to meet the dual requirements of artificial mixing in winter and oxygenation in summer (Wüest et al. 1992). A picture of this 7 m diameter diffuser (McGinnis et al. 2004) is shown in Figure 46.

The important design parameters in lake aeration are the diffuser air flow rate and the bubble diameter which together control the rate of dissolution of the released oxygen within a desired depth. In the present work, the two-fluid and mixed-fluid integral plume models are run to make a comparative study of the phenomenon of

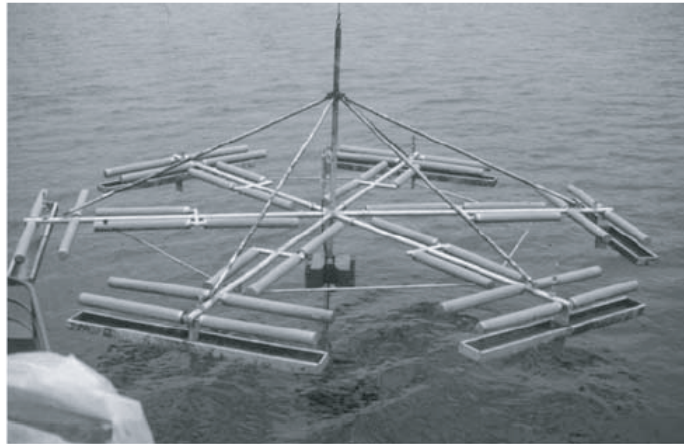


Fig. 46. Top view of the 7 m diameter diffuser *TANYTARSUS* (McGinnis et al. 2004)

dissolution of air in a lake The lake data used is the same as in the previous case, shown in Table 3. The different flux variables over depth and the DMPR (Depth of Maximum Plume Rise) predicted by the two models are compared against each other.

The base case parameters for this case study have been listed in Table 2. With these parameters, the two-fluid and mixed-fluid models were run for the same lake data and with exactly same values of the base case parameters. The comparison of the computed values of the flux variables Q , J , F_w , F_b , H , C , S and W_b are shown in Figure 47. It is to be noted that the plot of F_w vs. z does not contain the computations corresponding to the mixed-fluid model. This is because in a mixed-fluid model, the dispersed and continuous phases are assumed to form a mixture. The mixture buoyancy flux F for the mixed fluid model has been compared against the dispersed phase buoyancy flux F_b for the two-fluid model, because initially these two values are the same.

It is seen from the plot of the dispersed phase mass flux W_b vs. the depth z that, while the two-fluid model predicts all of the released air bubbles to dissolve at a

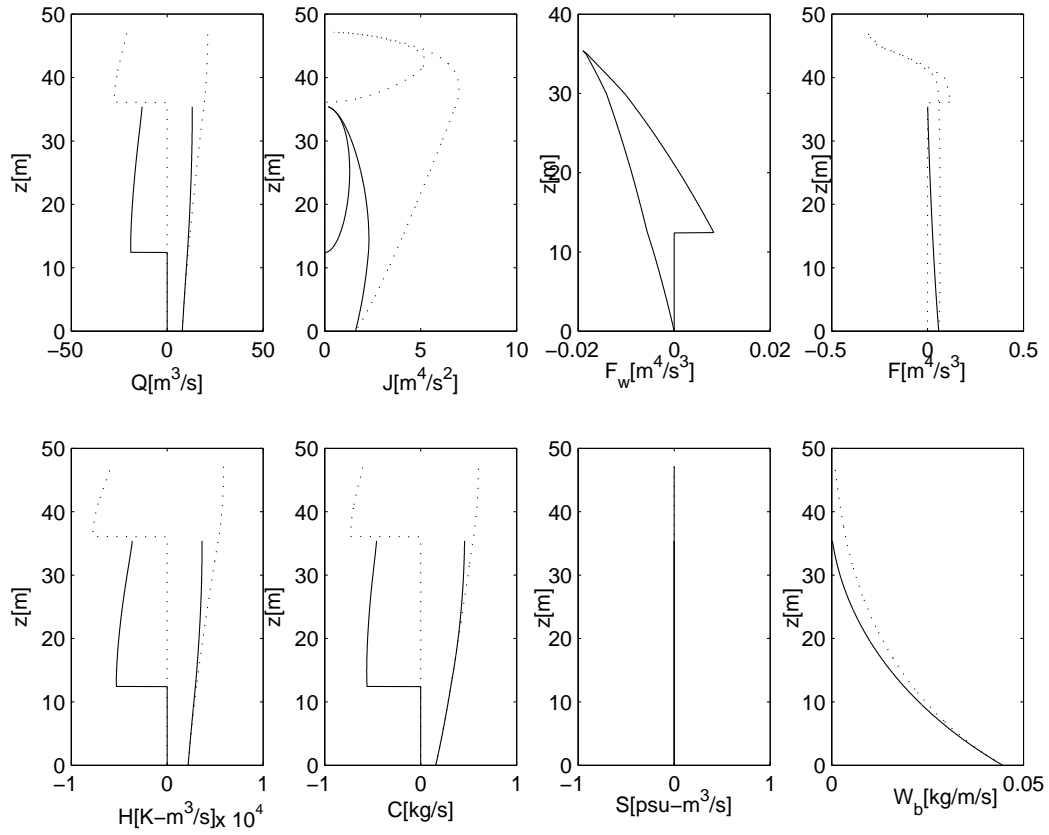


Fig. 47. Numerical simulation of air-bubble for the lake using the mixed-fluid and two-fluid modeling approaches. Bold lines denote results for the two-fluid model and dotted lines for the mixed fluid model.

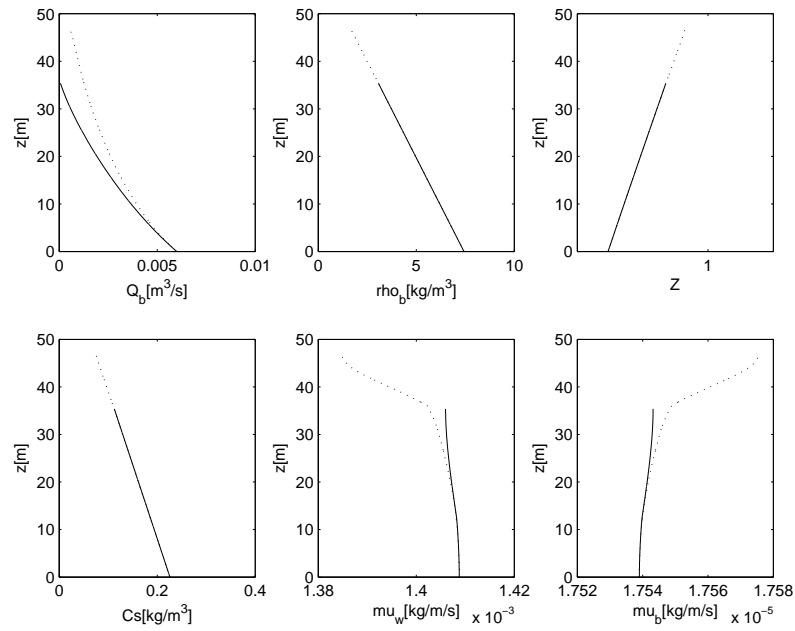


Fig. 48. Phase properties vs. depth as tracked by the two-fluid and the mixed-fluid models. Bold lines denote results for the two-fluid model and dotted lines for the mixed fluid model.

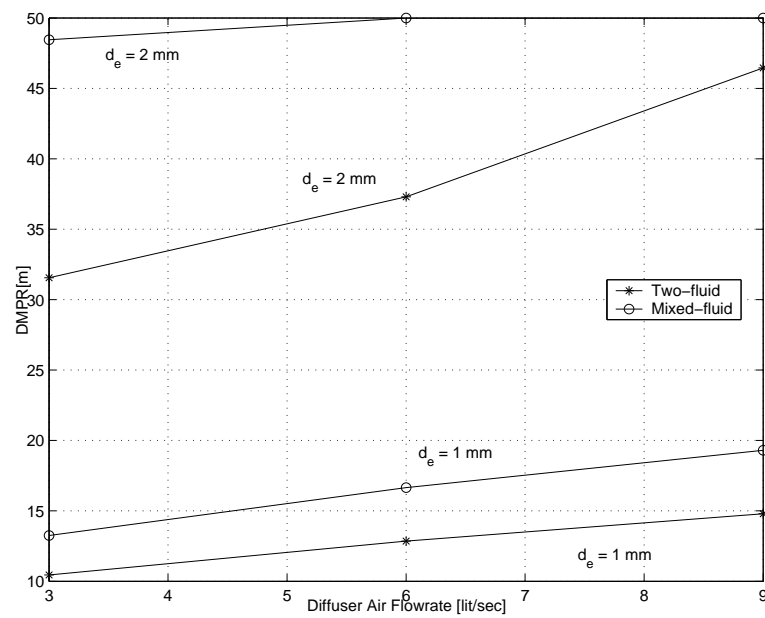


Fig. 49. DMPR of air-bubble plumes for different values of diffuser air flowrate and bubble diameter.

height of about 37 m, the mixed-fluid model computes this height to be nearly 48 m, that is, the mixed-fluid model predicts a higher DMPR and the difference is about 30%. The variation of the phase properties over depth as tracked by the two models are shown in Figure 48.

The two models were then run for values of Q_0 equal to 3, 6 and 9 l/s for bubble diameters of 2 mm and 1 mm respectively. The DMPR was noted in each case and the results are plotted graphically in Figure 49. It is seen that, for a given air-flowrate, the DMPR is reduced to about one-third of the value when the bubble diameter is halved, as expected. On the other hand, for the same bubble diameter, when the air flowrate is reduced by one-half, the DMPR reduces by only about one-sixth of its value. Also another significant result that can be deciphered from Figure 47 is that as the bubble diameter decreases, the difference in the results predicted by the two models also diminishes. This is because from Clift et al. (1978), the slip velocity decreases with the bubble diameter for bubble diameters below 2 mm, and as has been derived in Chapter II, the two model results eventually converge when the slip velocity goes to zero.

3. Ocean Sequestration of CO₂

Global warming is predicted to occur by many global climate models due to the atmospheric build-up of greenhouse gases, two-thirds of which is CO₂(Carbon dioxide). This is a consequence of progressive industrialization, deforestation and chiefly, continuous burning of fossil fuels. Even though the former two activities can be stopped by implementing legal reforms, consumption of fuel cannot be significantly reduced unless novel ways are devised to effectively harness other unconventional sources of energy, which at present looks unfeasible. Therefore, sequestration of atmospheric

CO₂ into the deeper layers of the ocean is among the proposed mitigation schemes to counter this threat of ever-increasing CO₂ accumulation and thereby to at least keep the peak concentration of CO₂ in the atmosphere below an allowable maximum (Chow 2004).

Figure 50 shows the schematic of different ways by which CO₂ can be disposed into the ocean. The principal aspect of consideration in this regard is to ensure that the released CO₂ is sufficiently negatively buoyant so that it sinks or is weakly positively buoyant so that it dissolves completely before being able to escape into the atmosphere. A number of negatively buoyant forms of CO₂ have been proposed in the literature. These include dry ice (solid) (Nakanishi, Ohsumi & Shitashima 1994, Caulfield, Adams, Auerbach & Herzog 1997), very cold CO₂ (COSMOS) (Aya, Yamane & Shiozaki 1999), CO₂/CaCO₃ emulsions (Caldeira & Rau 2000, Rau & Caldeira 1999), dense CO₂ brine solutions (Haugen & Drange 1992, Adams, Golomb, Zhang & Herzog 1995) and liquid CO₂ droplets and clathrate mixtures (Warzinski, Lynn & Holder 2000). It is much costlier to use a more negatively buoyant form of CO₂, hence liquid CO₂ droplets, even though slightly positively buoyant, is usually the most cost-effective choice of phase. This form of CO₂ release would be acceptable if the droplets are released at a deep enough depth (Crounse 2000) so that all of them dissolves before escaping into the atmosphere.

In the present work, liquid CO₂ droplets of 5 mm diameter are released by the help of a buoyant source of 1 m diameter placed at a depth of 800 m in the ocean. The droplets are positively buoyant, so that they rise up owing to their buoyancy until they dissolve at a particular depth. The ocean temperature and salinity data are taken from Teng & Yamasaki (1998) as shown in Table 4. It is important to note from the table that the phase of CO₂ changes from liquid to gas at a depth of 450 m. This means that the scheme is successful only if all of the released CO₂ dissolves before reaching

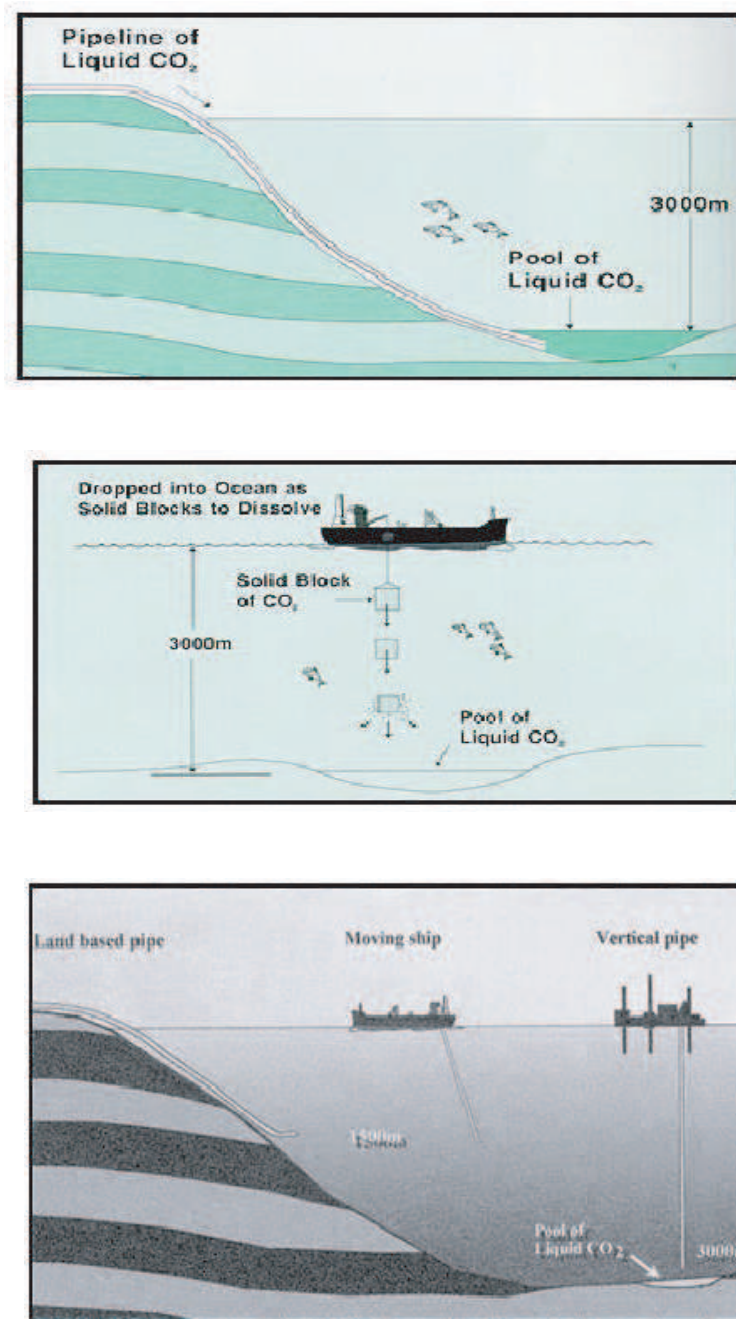


Fig. 50. Schematic of various CO₂ sequestration schemes in the deep ocean (<http://archive.greenpeace.org/politics/co2/co2dump.pdf>)

Table 4. Ocean temperature data taken from Teng(1996)

Depth m	Temperature °C	Salinity psu	State of Discharged CO ₂
0.0	20.0	35	gas bubbles
100.0	20.0	35	gas bubbles
200.0	19.5	35	gas bubbles
300.0	18.5	35	gas bubbles
400.0	13.5	35	gas bubbles
450.0	11.5	35	phase change depth
500.0	9.0	35	liquid droplets
600.0	7.6	35	liquid droplets
700.0	6.6	35	liquid droplets
800.0	6.0	35	liquid droplets

this depth as they move upwards. With this objective in mind, the two-fluid and the mixed-fluid integral plume models are run for the base case parameters listed in Table 2 for Case 3 to estimate the DMPR, and the results are compared. The fluxes of mass, momentum, buoyancy, temperature, salinity and concentration are also tracked. By tracking the concentration flux of CO₂, the seawater pH can be calculated which is important because lowering of pH below a certain level has been found to have a detrimental effect on marine organisms (Knutzen 1981, Tamburri, Peltzer, Friederich, Aya, Yamane & Brewer 2000). The upper limit of depth considered is 350 m because beyond this depth, phase change will occur (as seen from Table 4) which must be prevented for the design scheme to be successful. Because of the uncertainty involved in the extent of formation of clathrate hydrate as the plume of liquid CO₂ moves up through the ocean waters, a mid-value of the CO₂ mass transfer coefficient is chosen for making realistic dissolution estimates. Figure 51 shows the density stratification along the depth of the ocean corresponding to the temperature data presented in

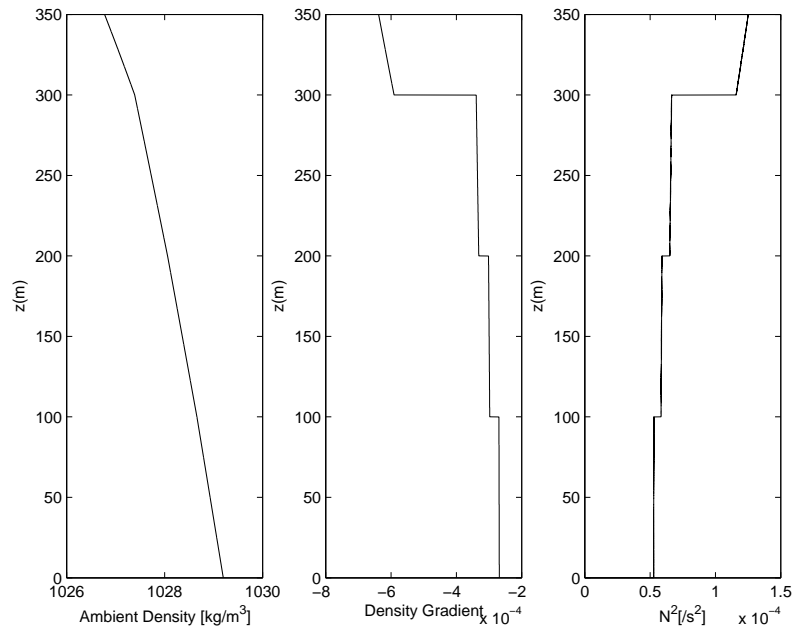


Fig. 51. Variation of ocean water density with depth

Table 4.

The two-fluid and the mixed-fluid model results for the base case is shown in Figure 52. It is seen that while the two-fluid model predicts that all of the release dispersed phase dissolves at a height of about 72 m, the mixed-fluid model calculates this height to be about 117 m. This is because as has been physically explained and mathematically derived in Chapter II, the mixed-fluid model underpredicts the rate of change of momentum flux J , so the momentum flux goes to zero at a higher depth and hence peeling is delayed in case of the mixed-fluid model.

Finally, the two models were run separately for different release rates to estimate the DMPR which is effectively the height at which all of the released CO_2 dissolves, for three different values of the mass transfer coefficient, namely 0.1, 0.5 and 1.0 times the actual value. The value of 0.1 corresponds to a high extent of formation of hydrates and the value of 1.0 corresponds to zero hydrate formation. Figure 53 is the

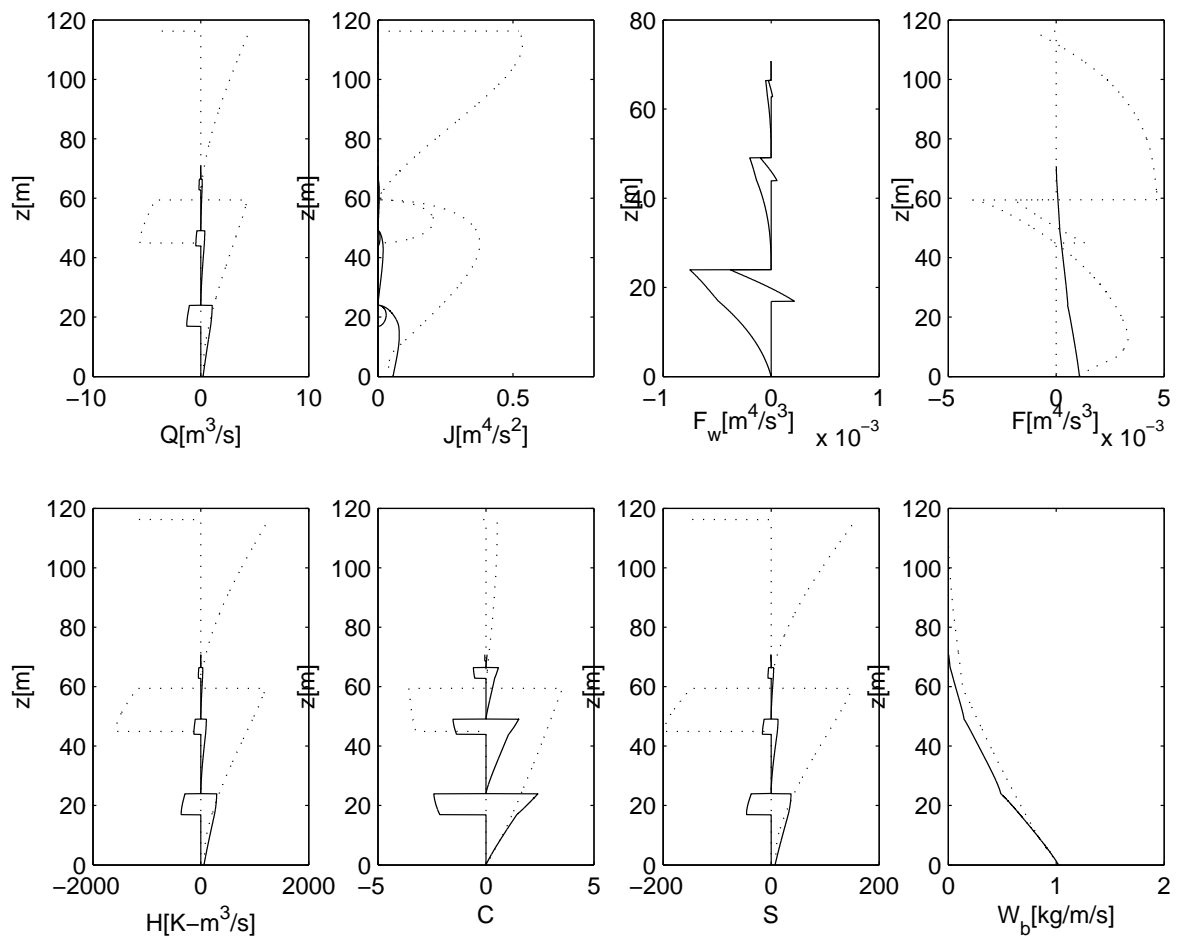


Fig. 52. Comparison of results for the two-fluid and mixed-fluid models. Bold lines denote results for the two-fluid model and dotted lines for the mixed fluid model.

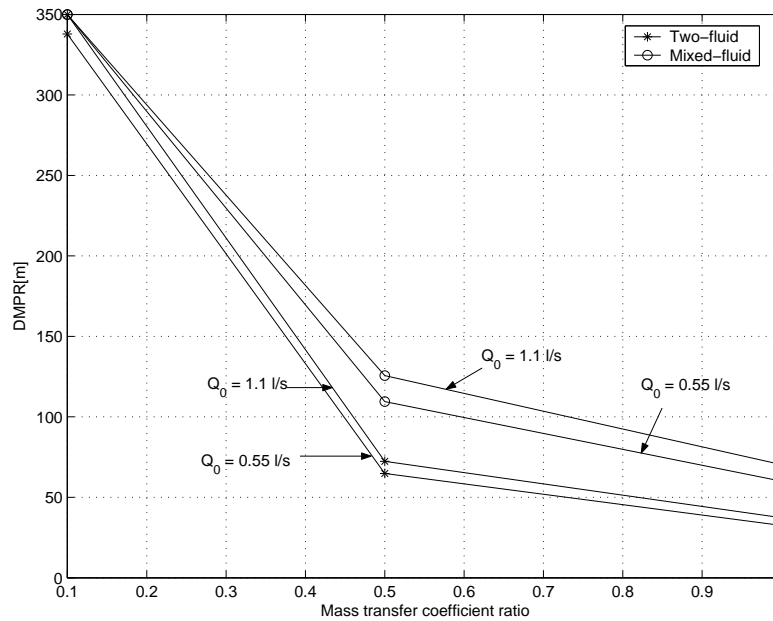


Fig. 53. Comparison of results for the two-fluid and mixed-fluid models for estimated DMPR for liquid CO_2 droplet plumes

result of this plot. It is seen from the plot that with increasing hydrate formation, the mass transfer coefficient of CO_2 going to dissolution is lowered so that the two-fluid model predicts a height of nearly 340 m where complete dissolution occurs, as opposed to a height of only 30 m with no hydrate formation. The mixed fluid model again overpredicts this height and the CO_2 phase goes beyond the design margin of 350 m. This shows once again that the improper choice of the correct modeling approach has far-reaching consequences on the realisation of the design objectives.

CHAPTER VIII

SUMMARY AND CONCLUSIONS

The mixed-fluid and the two-fluid modeling approaches are among the most recent and advanced scientific numerical methods that are used to simulate multiphase plumes in nature. The goal of the present work was to make a detailed comparative study of the two modeling approaches for integral plume models for the most general case of double plumes by comparing model results to experimental data, and to better understand what the implications of the differences in the outputs of the two models have in realizing field scale design objectives. The most striking difference between the two models was found to lie in the equation for the conservation of momentum flux, specifically in the calculation of the buoyant forces responsible for the momentum generation for the plume. Since the mixed-fluid model treats the dispersed and continuous phases inside the plume as a mixture, the net buoyant force is calculated as a whole on the mixture phase, which is found to differ significantly when compared to the two-fluid model where the buoyant forces acting on the two phases are calculated separately. This difference was derived mathematically and was found to be a function of the slip velocity of the dispersed phase, the spreading ratios and the densities of the phases. The treatment of the two different phases separately in the formulation of the conservation equations is more reasonable to represent multiphase plume physics, so the two-fluid model is more justified than the mixed-fluid model and this conclusion was also confirmed by matching the model results to experimental measurements.

Integral plume model computations rely on appropriate initial conditions for the flux variables, to be provided both for inner as well as outer plumes. In this work, a detailed study was performed to analyze and develop the existing methods of obtaining

these initial conditions. Among all methods of determining initial conditions, those of Wüest et al. (1992) was found to match the experimental data for the momentum flux, the dispersed phase Froude number and the dispersed phase void fraction most closely. The outer plume initial conditions were derived based on the proposition of Asaeda & Imberger (1993) with the addition of two new parameters, the fractional peeling coefficient μ_p and the extra entrainment factor μ_e , although, the effects of these two parameters were not studied in detail in this work. Model convergence was found to be adequate for both models starting with the inner and outer plume initial conditions for the first plume. For the subsequent plumes, some oscillations were noted in a few cases which suggests that further improvements are necessary in the determination of the initial conditions for subsequent inner plumes.

A detailed sensitivity analysis of the model parameters showed that both models were quite insensitive to the values of the momentum amplification factor γ and the spreading ratio λ_1 . However the sensitivity to the entrainment coefficient α and the entrainment ratio κ were found to be important.

A graphical user interface was designed to condense all of the computational work necessary for both models with in-built algorithms for computing the initial conditions and reading in input data conveniently from the user. The two models were finally run for three case studies identified as lake destratification, lake aeration and CO₂ sequestration in deep ocean, and the results were compared against each other. In all of the three cases, the mixed-fluid model was found to predict on an average of about 30% higher values for the peel heights and for the DMPR than the two-fluid model. This conclusion has important consequences as far as the realization of actual design standards and objectives are concerned. For the design of a lake destratification system, using the mixed-fluid model would therefore mean predicting lower values of the optimal air-flowrate necessary to achieve destratification, thereby

leading to an under-design. For achieving aeration below the hypolimnion in a lake, for a given air flow rate this would mean the requirement of smaller bubble sizes if dissolution predictions are made using the mixed-fluid model, thereby calling for a more expensive design than is actually necessary. Lastly, if the mixed-fluid model is used to conduct a feasibility study of a CO₂ sequestration experiment, it would require the release source to be placed at a deeper depth in the ocean to ensure complete dissolution to occur below the phase change depth, for a given release rate and droplet size. So it would lead to a more expensive scheme if simulations are based on the mixed-fluid model. Therefore, the use of the two-fluid model which is physically more justified than the mixed-fluid model would lead to more reliable and economic, and hence better designs.

REFERENCES

- Adams, E., Golomb, D., Zhang, X. & Herzog, H. (1995). "Confined release of CO₂ into shallow sea water." *Direct Ocean Disposal of Carbon Dioxide*, TERRAPUB, Tokyo, Japan, 153–164.
- Angus, S., Armstrong, B. & Reuck, K. D. (1976). *International Thermodynamic Tables of the Fluid State*, Pergamon Press, Oxford, England.
- Asaeda, T. & Imberger, J. (1993). "Structure of bubble plumes in linearly stratified environments." *Journal of Fluid Mechanics*, 249, 35–57.
- Aya, I., Yamane, K. & Shiozaki, K. (1999). "Proposal of self sinking CO₂ sending system: Cosmos." *Greenhouse Gas Control Technologies*, 269–274.
- Baines, W. & Leitch, A. (1992). "Destruction of stratification by bubble plume." *Journal of Hydraulic Engineering*, 118, 559–577.
- Bergmann, C. (2004). "Physical and numerical studies on multiphase plumes." MS Thesis, Texas A&M University, College Station, Texas.
- Bergmann, C., Seol, D.-G., Bhaumik, T. & Socolofsky, S. (2004). "Entrainment and mixing properties of a simple bubble plume." presented at the 4th International Symposium on Environmental Hydraulics, IAHR, Hong Kong, China.
- Caldeira, K. & Rau, G. (2000). "Accelerating carbonate dissolution to sequester carbon dioxide in the ocean: Geochemical implications." *Geophysical Research Letters*, 27(2), 225–228.
- Caulfield, J., Adams, E., Auerbach, D. & Herzog, H. (1997). "Impacts of ocean CO₂ disposal on marine life: Ii. probabilistic plume exposure model used with a

- time-varying dose-response analysis.” *Environmental Modeling and Assessment*, 2, 345–353.
- Chow, A. C. (2004). “Effects of buoyancy source composition on multiphase plume behavior in stratification.” MS thesis, Massachusetts Institute of Technology, Cambridge, Massachusetts.
- Clift, R., Grace, J. & Weber, M. (1978). *Bubbles, Drops, and Particles*, Academic Press, New York.
- Crouse, B. C. (2000). “Modeling buoyant droplet plumes in a stratified environment.” MS thesis, Massachusetts Institute of Technology, Cambridge, Massachusetts.
- Deen, N., Solberg, T. & Hjertager, B. (2001). “Large eddy simulation of the gas-liquid flow in a square cross-sectioned bubble column.” *Chemical Engineering Sciences*, 56, 6341–6349.
- Ditmars, J. D. & Cederwall, K. (1974). “Analysis of air-bubble plumes.” *Proceedings of the Fourteenth Conference on Coastal Engineering*, ASCE, Copenhagen, Denmark, 128, 2209–2226.
- Fischer, H., List, E., Koh, R., Imberger, J. & Brooks, N. (1979). *Mixing in Inland and Coastal Waters*, Academic Press, San Diego, California.
- Gill, A. (1982). *Ocean-Atmosphere Dynamics*, Academic Press, New York.
- Goossens, L. (1979). *Reservoir Destratification with Bubble Columns*, Delft University Press, Delft, The Netherlands.
- Haugen, P. & Drange, H. (1992). “Sequestration of CO₂ in the deep ocean by shallow injection.” *Nature*, 357(28), 1065–1072.

- Hirai, S., Okazaki, K., Araki, N., Yazawa, H., Ito, H. & Hijikata, K. (1996). "Transport phenomena of liquid CO₂ in pressurized water flow with clathrate-hydrate at the interface." *Energy Conversion and Management.*, 37(6–8), 1073–1078.
- Jirka, G., Doneker, R. & Hinton, S. (n.d.). *User's manual for CORMIX: A hydrodynamic mixing zone model and decision support system for pollutant discharges into surface waters*, University of Karlsruhe, Karlsruhe, Germany.
- Johansen, O. (2000). "Deepblow - a lagrangian plume model for deep water blowouts." *Spill Science and Technology Bulletin*, 6(2), 103–111.
- Johnson, A. & White, D. (1993). "Experimental-determination of gas migration velocities with non-newtonian fluids." *International Journal of Multiphase Flow*, 19(6), 921–941.
- Knutzen, J. (1981). "Effects of decreased pH on marine organisms." *Marine Pollution Bulletin*, 12(1), 25–29.
- Kobus, H. (1968). "Analysis of the flow induced by air-bubble systems." *Proceedings of the 11th International Conference on Coastal Engineering*, London, ASCE, Reston, Virginia, 1016-1031.
- Koh, R. & Chang, Y. (1973). "Mathematical model for barged ocean disposal of waste." *Technical Report 660*, U.S. EPA, Washington, D.C.
- Lee, J. & Cheung, V. (1990). "Generalized lagrangian model for buoyant jets in current." *Journal of Environmental Engineering*, 116(6), 1085–1106.
- Lemckert, C. & Imberger, J. (1993). "Energetic bubble plumes in arbitrary stratification." *Journal of Hydraulic Engineering*, 119(6), 680–703.

- Lemmon, E., Jacobsen, R., Penoncello, S. & Friend, D. (2000). "Thermodynamic properties of air and mixtures of nitrogen, argon and oxygen from 60 to 2000 K at pressures to 2000 MPa." *Journal of Physical Chemistry Reference Data*, 29(3), 331–349.
- Liro, C., Adams, E. & Herzog, H. (1992). "Modeling the release of CO₂ in the deep ocean." *Energy Conversion and Management*, 33(5–8), 667–674.
- Lund, P. C. (1995). "Impact of CO₂ hydrates on ocean carbon dioxide deposition options." *Technical Report*, Institut für Energietechnik u. Wasser-wirtschaft, ETH, Zürich, Switzerland.
- Marshall, T. (1976). *Gas Encyclopaedia*, Elsevier, New York.
- McDougall, T. (1978). "Bubble plumes in stratified environments." *Journal of Fluid Mechanics*, 85, 655–672.
- McGinnis, D., Lorke, A., Wüest, A., Stöckli, A. & Little, J. (2004). "Interaction between a bubble plume and the near field in a stratified lake." *Water Resources Research*, 40.
- Milgram, J. (1983). "Mean flow in round bubble plumes." *Journal of Fluid Mechanics*, 133, 345–376.
- Morton, B., Taylor, G. & Turner, J. (1956). "Turbulent gravitational convection from maintained and instantaneous sources." *Proceedings of the Royal Society in London*, A234, 1–23.
- Motarjemi, M. & Jameson, G. (1978). "Mass transfer from very small bubbles - the optimum bubble size for aeration." *Chemical Engineering Sciences*, 33, 1415–1423.

- Nakanishi, N., Ohsumi, T. & Shitashima, K. (1994). "Sequestering of CO₂ in a deep ocean." *Technical Report, Central Research Institute of Electric Power Industry, Abiko-City, Chiba 270-11, Japan.*
- Nepf, H. (1995). *Course Notes and problem sets: MIT Course 1.77: Water Quality Control*, MIT, Cambridge, Massachusetts.
- Ohsumi, T., Nakashiki, N., Shitashima, K. & Hiramata, K. (1992). "Density change of water due to dissolution of carbon dioxide and near-field behavior of CO₂ from a source on deep-sea floor." *Energy Conversion and Management*, 33(5-8), 685–690.
- Patterson, J. & Imberger, J. (1989). "Simulation of bubble plume destratification systems in reservoirs." *Aquatic Sciences Journal*, 51(1), 1–18.
- Rau, G. & Caldeira, K. (1999). "Enhanced carbonate dissolution: A means of sequestering waste CO₂ as ocean bicarbonate." *Energy Conversion and Management*, 40, 1803–1813.
- Rye, H. (1994). "Model for calculation of underwater blow-out plume." *Proceedings of the Seventeenth Arctic Marine Oil Spill Program (AMOP) Technical Seminar*, 2, 849–865.
- Schladow, S. (1993). "Lake destratification by bubble plume systems: Design methodology." *Journal of Hydraulic Engineering*, 119, 350–368.
- Socolofsky, S. (2001). "Laboratory experiments of multi-phase plumes in stratification and crossflow." PhD Dissertation, MIT, Cambridge, Massachusetts.
- Socolofsky, S. & Adams, E. (2005). "Role of slip velocity in the behavior of stratified multiphase plumes." *Journal of Hydraulic Engineering*, 131(4), 273–282.

- Socolofsky, S., Crounse, B. & Adams, E. (2002). "Multiphase plumes in uniform, stratified and flowing environments." H. Shen, A. Cheng, K.-H. Wang, M. H. Teng & C. Liu, eds, *Environmental Fluid Mechanics - Theories and Applications*, ASCE/Fluids Committee, New York.
- Taitel, Y., Barnea, D. & Brill, J. (1995). "Stratified 3-phase flow in pipes." *International Journal of Multiphase Flow*, 21, 53–60.
- Tamburri, M., Peltzer, E., Friederich, G., Aya, I., Yamane, K. & Brewer, P. (2000). "A field study of the effects of CO₂ disposal on mobile deep-sea animals." *Marine Chemistry*, 72, 95–101.
- Teng, H., Masutani, S., Kinoshita, C. & Nihous, G. (1996). "Solubility of CO₂ in the ocean and its effect on CO₂ dissolution." *Energy Conversion and Management*, 37(6–8), 1029–1038.
- Teng, H. & Yamasaki, A. (1998). "Solubility of liquid CO₂ in synthetic sea water at temperatures from 278 K to 293 K and pressures from 6.44 MPa to 29.49 MPa, and densities of the corresponding aqueous solutions." *Journal of Chemical Engineering Data* 43, 2–5.
- Topham, D. (1975). "Hydrodynamics of an oil well blowout." *Technical Report 33*, Institute of Ocean Sciences, Sidney, B.C, Canada.
- Turner, J. (1986). "Turbulent entrainment: The development of the entrainment assumption, and its application to geophysical flows." *Journal of Fluid Mechanics*, 173, 431–471.
- Warzinski, R. P. & Holder, G. D. (1999). "Ocean storage of CO₂: Experimental observations of clathrate hydrates in seawater." *Greenhouse Gas Control Tech-*

nologies, B. Eliasson, P. Reimer & A. Wokaun, eds., Elsevier Science Ltd., New York, 1061–1063.

Warzinski, R., Lynn, R. & Holder, G. (2000). “The impact of CO₂ clathrate hydrate on deep ocean sequestration of CO₂: Experimental observations and modeling results.” *Annals of the New York Academy of Sciences*, 912, 226–234.

Wüest, A., Brooks, N. & Imboden, D. (1992). “Bubble plume modeling for lake restoration.” *Water Resources Research*, 28, 3235–3250.

Yapa, P. & Zheng, L. (1999). “Modeling underwater oil/gas jets and plumes.” *Journal of Hydraulic Engineering*, 125, 481–491.

APPENDIX

EQUATION OF STATE FOR SEAWATER, CO₂ AND AIR

1. Seawater Equation of State

The density of seawater $\rho_{sw}(T, S, P)$ can be calculated from the seawater equation of state (Gill 1982) where ρ_{sw} is in kg/m³, temperature T is in °C, salinity S is in practical salinity units (psu), and the hydrostatic pressure P is in bars.

The density at one standard atmosphere ($P = 0$) is given by

$$\begin{aligned}
\rho_{sw}(T, S, 0) = & 999.845294 \\
& + 6.793952 \times 10^{-2} \times T - 9.095290 \times 10^{-3} \times T^2 \\
& + 1.001685 \times 10^{-4} \times T^3 - 1.120083 \times 10^{-6} \times T^4 \\
& + 6.536332 \times 10^{-9} \times T^5 + 8.24493 \times 10^1 \times S \\
& - 5.72466 \times 10^{-3} \times S^{\frac{3}{2}} + 4.8314 \times 10^{-4} \times S^2 \\
& - 4.0899 \times 10^{-3} \times TS + 7.6483 \times 10^{-5} \times T^2S \\
& - 8.2467 \times 10^{-7} \times T^3S + 5.3875 \times 10^{-9} \times T^4S \\
& + 1.0227 \times 10^{-4} \times TS^{\frac{3}{2}} - 1.6546 \times 10^{-6} \times T^2S^{\frac{3}{2}} \quad (A.1)
\end{aligned}$$

The density of seawater at a water depth with non-zero hydrostatic pressure P is given by

$$\rho_{sw}(T, S, P) = \frac{\rho_{sw}(T, S, 0)}{1 - \frac{1}{K(T, S, P)}} \quad (A.2)$$

where

$$\begin{aligned}
K(T, S, P) = & 19652.21 + 148.4206 \times T - 2.327105 \times T^2 \\
& + 1.360477 \times 10^{-2} \times T^3 - 5.155288 \times 10^{-5} \times T^4 + 3.239908 \times P \\
& + 1.43713 \times 10^{-3} \times TP + 1.16092 \times 10^{-4} \times T^2P - 5.77905 \times 10^{-7} \times T^3P \\
& + 8.50935 \times 10^{-5} \times P^2 - 6.12293 \times 10^{-6} \times TP^2 + 5.2787 \times 10^{-8} \times T^2P^2 \\
& + 54.6746 \times S - 0.603459 \times TS + 1.09987 \times 10^{-2} \times T^2S \\
& - 6.1670 \times 10^{-5} \times T^3S + 7.944 \times 10^{-2} \times S^{\frac{3}{2}} + 1.6483 \times 10^{-2} \times TS^{\frac{3}{2}} \\
& - 5.3009 \times 10^{-4} \times T^2S^{\frac{3}{2}} + 2.2838 \times 10^{-3} \times PS - 1.0981 \times 10^{-5} \times TPS \\
& - 1.6078 \times 10^{-6} \times T^2PS + 1.91075 \times 10^{-4} \times PS^{\frac{3}{2}} - 9.9348 \times 10^{-7} \times P^2S \\
& + 2.0816 \times 10^{-8} \times TP^2S + 9.1697 \times 10^{-10} \times T^2P^2S \quad (\text{A.3})
\end{aligned}$$

2. CO₂ Equation of State

The IUPAC equation of state for CO₂ (Angus et al. 1976) is used to calculate the compressibility Z of CO₂ to account for its non-ideal behavior. This is given by the analytic equation of state, expressed in terms of the reduced density ω and reciprocal reduced temperature τ as follows:

$$Z = 1 + \omega \sum_{i=0}^9 \sum_{j=0}^6 b_{ij} (\tau - 1)^j (\omega - 1)^i \quad (\text{A.4})$$

where $\omega = \frac{\rho}{\rho_1}$, $\tau = \frac{T_1}{T}$, $\rho_1 = 0.468 \text{ gm/cm}^3$, and $T_1 = 304.2K$. The values of the coefficients b_{ij} are obtained from Table 5.

Eq. (A.4) is not accurate near the critical point of CO₂, which is located at $T = 304.2K$ and $P = 73.86 \text{ bar}$. However, since the ambient ocean conditions are never met in the vicinity of the critical point, so this equation is applicable to the present work.

The fugacity f may also be calculated by using Eq. (A.4) which is given by

$$\ln\left(\frac{f}{P}\right) = -\ln Z + \left[2 \sum_{i=0}^9 \sum_{j=0}^6 \frac{b_{ij}}{i+1} (\tau-1)^j (\omega-1)^{i+1} + \sum_{i=1}^9 \sum_{j=0}^6 b_{ij}(i) (\tau-1)^j \left(\frac{(\omega-1)^{i+1}}{(i+1)} + \frac{(\omega-1)^i}{i} \right) \right]_0^\rho \quad (\text{A.5})$$

where the P is the partial pressure of CO_2 which can be calculated by the expression

$$P = RT \frac{\rho}{M_{\text{CO}_2}} Z \quad (\text{A.6})$$

where $R = 8.314 \text{ kJ/mol/K}$ and $M_{\text{CO}_2} = 44.01 \text{ g/mol}$

3. Air Equation of State

The equation of state for air in terms of the compressibility Z is given by the expression (Lemmon et al. 2000)

$$Z = \frac{P}{\rho RT} = 1 + \delta \left(\frac{\partial \alpha_r}{\partial \delta} \right)_\tau \quad (\text{A.7})$$

where $\delta = \frac{\rho}{\rho_j}$ is the reduced density, $\tau = \frac{T_j}{T}$ is the reciprocal reduced temperature and α_r is the residual of the Helmholtz energy. $\rho_j = 10.4477 \text{ mol/dm}^3$ and $T_j = 132.6035 \text{ K}$. The derivative of the Helmholtz energy is given by

$$\left(\frac{\partial \alpha_r}{\partial \delta} \right)_\tau = \sum_{k=1}^{10} i_k N_k \delta^{i_k-1} \tau^{j_k} \times \exp(-\delta^{l_k}) (i_k - l_k \delta^{l_k}) \quad (\text{A.8})$$

The coefficients N_k and the exponents i_k , j_k and l_k are obtained from Table 6.

Table 5. Coefficients b_{ij} for the CO₂ equation of state

	j=0	j=1	j=2	j=3
i=0	-0.725854437×10^0	-0.168332974×10^1	0.259587221×10^0	0.376945574×10^0
i=1	0.447869183×10^0	0.126050691×10^1	0.596957049×10^1	0.154645885×10^2
i=2	-0.172011999×10^0	-0.183458178×10^1	-0.461487677×10^1	-0.382121926×10^1
i=3	$0.446304911 \times 10^{-2}$	-0.176300541×10^1	-0.111436705×10^2	-0.278215446×10^2
i=4	0.255491571×10^0	0.237414246×10^1	0.750925141×10^1	0.661133318×10^1
i=5	$0.594667298 \times 10^{-1}$	0.116974683×10^1	0.743706410×10^1	0.150646731×10^2
i=6	-0.147960010×10^0	-0.169233071×10^1	-0.468219937×10^1	-0.313517448×10^1
i=7	$0.136710441 \times 10^{-1}$	-0.100492330×10^0	-0.163653806×10^1	-0.187082988×10^1
i=8	$0.392284575 \times 10^{-1}$	0.441503812×10^0	0.886741970×10^0	0
i=9	$-0.119872097 \times 10^{-1}$	$-0.846051949 \times 10^{-1}$	$0.464564370 \times 10^{-1}$	0

	j=4	j=5	j=6
i=0	-0.670755370×10^0	-0.871456126×10^0	-0.149156928×10^0
i=1	0.194449475×10^2	0.864880497×10^1	0
i=2	0.360171349×10^1	0.492265552×10^1	0
i=3	-0.271685720×10^2	-0.642177872×10^1	0
i=4	-0.242663210×10^1	-0.257944032×10^1	0
i=5	0.957496845×10^1	0	0
i=6	0	0	0
i=7	0	0	0
i=8	0	0	0
i=9	0	0	0

Table 6. Coefficients and exponents for the air equation of state

k	N_k	i_k	j_k	l_k
1	0.118160747229	1	0	0
2	0.713116392079	1	0.33	0
3	$-0.161824192067 \times 10^1$	1	1.01	0
4	$0.714140178971 \times 10^{-1}$	2	0	0
5	$-0.865421396646 \times 10^{-1}$	3	0	0
6	0.134211176704	3	0.15	0
7	$0.112626704218 \times 10^{-1}$	4	0	0
8	$-0.420533228842 \times 10^{-1}$	4	0.2	0
9	$0.349008431982 \times 10^{-1}$	4	0.35	0
10	$0.164957183186 \times 10^{-3}$	6	1.35	0
11	-0.101365037912	1	1.6	1
12	-0.173813690970	3	0.8	1
13	$-0.472103183731 \times 10^{-1}$	5	0.95	1
14	$-0.122523554253 \times 10^{-1}$	6	1.25	1
15	-0.146629609713	1	3.6	2
16	$-0.316055879821 \times 10^{-1}$	3	6	2
17	$0.233594806142 \times 10^{-3}$	11	3.25	3
18	$0.148287891978 \times 10^{-1}$	1	3.5	3
19	$-0.938782884667 \times 10^{-2}$	3	15	3

VITA

Tirtharaj Bhaumik was born on July 19, 1978 in Durgapur, India. He got his B.Tech. degree in Ocean Engineering in 2002 from Indian Institute of Technology (IIT), Kharagpur. He served one year of service in the Defense Research and Development Organisation (DRDO) from August 2002 to July 2003 in India. He came to Texas A&M University, College Station in the Fall of 2003 to pursue his Master of Science in Ocean Engineering. His research interests include Computational Fluid Dynamics, Multiphase Flow and Direct Ocean Carbon Sequestration, Fluid Mechanics, Large Eddy Simulation, Particle Image Velocimetry and Numerical Modeling. His permanent address is

Tirtharaj Bhaumik,
C/O Dr. Nirmalendu Bhaumik,
PO: Khanjanchak, Haldia - 721602,
Dt: East Midnapore,
West Bengal, INDIA.